UNIVERSITÀ DEGLI STUDI DI PADOVA

Dipartimento di Fisica e Astronomia "Galileo Galilei"

Corso di Laurea Magistrale in Fisica

Tesi di Laurea

Unidimensional hyperbolic metamaterials: synthesis and characterization

Relatore

Prof. Giovanni Mattei

Correlatore

Dr. Tiziana Cesca

Laureando

Alessandro Cotrufo

Anno Accademico 2017/2018

Contents

Introduzione

L'emergente area di ricerca dei metamateriali propone un nuovo paradigma per ingegnerizzare la risposta ottica di un sistema, col quale ottenere anche proprietà che non sono rintracciabili nei materiali convenzionali [1]. Un metamateriale consiste solitamente in una cella unitaria ripetuta periodicamente nello spazio, in modo tale che il sistema complessivo deriva le sue proprietà non solo dai suoi materiali costituenti, ma anche dalla loro disposizione geometrica. Nell'ipotesi in cui i dettagli del sistema siano più piccoli della lunghezza d'onda di lavoro, la risposta elettromagnetica del metamateriale risulta essere la media spaziale di tale pattern periodico. Questo principio di base permette di costruire sistemi con proprietà particolari, come metamateriali a indice di rifrazione negativo, e metamateriali ottici nonlineari.

Tra i vari tipi di metamateriali, la classe di metamateriali iperbolici ha ricevuto interesse negli ultimi anni grazie alle sue proprietà, che possono essere ottenute anche a frequenze ottiche [2]. I metamateriali iperbolici sono mezzi non magnetici caratterizzati da una permittività tensoriale con componenti principali di segno opposto. Questa caratteristica fa sì che le curve di dispersione del sistema valutate a frequenza costante abbiano forma iperbolica invece che ellittica. A sua volta, ciò significa che in un metamateriale iperbolico possono propagarsi modi elettromagnetici con vettore d'onda arbitrariamente elevato, il che fa divergere la densità di stati fotonici nel mezzo. A differenza di altri tipi di metamateriali, questi sistemi hanno una natura non risonante con un'elevata figura di merito, possono essere realizzati con tecniche standard di nanofabbricazione, e le loro proprietà possono essere regolate facilmente lungo lo spettro. I metamateriali iperbolici hanno trovato applicazioni interessanti nel campo del biosensing [3], dell'ottica nonlineare [4], e del confinamento della luce [5], per citarne alcuni.

L'obiettivo di questa tesi è stato lo studio e la realizzazione di un metamateriale iperbolico nel visibile e nel vicino infrarosso. Come mezzo che approssimi la dispersione iperbolica si è scelto un multilayer con layer di oro e allumina alternati aventi spessori *subwavelength*. Si sono sviluppate simulazioni nel dominio della frequenza per studiare la validità dell'approssimazione di mezzo efficace per campioni spessi e sottili, e per valutare la capacità di un *nanohole array* come mezzo di accoppiamento con i modi del sistema aventi vettore d'onda elevato. Alcuni multilayer progettati in questo modo sono stati realizzati e studiati sperimentalmente con tecniche di scansione e tecniche ottiche.

La tesi si sviluppa in quattro capitoli. Il primo capitolo riprende alcune nozioni di elet-

tromagnetismo, cominciando dalle equazioni di Maxwell, ed esamina il caso dei mezzi uniassiali. Segue quindi un'introduzione all'area di ricerca dei metamateriali, partendo dai primi studi teorici e sperimentali. Si introduce il concetto di metamateriale iperbolico, e si derivano le formule di approssimazione di mezzo efficace per un multilayer. Si considera quindi il problema di eccitare modi elettromagnetici con elevato vettore d'onda, considerando l'accoppiamento mediante prisma e quello mediante reticolo. Infine, si introducono la teoria su molecole fluorescenti in prossimità di una superficie e la teoria dell'ottica nonlineare. Il secondo capitolo sviluppa le diverse tecniche sperimentali che sono state utilizzate nel lavoro di tesi, descrivendo gli apparati sperimentali e i protocolli di misura. Tra i metodi di misura compaiono: il magnetron sputtering, che è stato impiegato per realizzare i multilayer; tecniche per investigare le strutture dei campioni, in particolare la microscopia a forza atomica, la microscopia a scansione di elettroni, e la riflettività da raggi X; tecniche per misurare le proprietà ottiche dei multilayer, come l'ellissometria spettroscopica, la tecnica z-scan, e le misure di fotoluminescenza. Il terzo capitolo contiene i risultati dello studio simulativo di un multilayer di oro e allumina come approssimazione di un metamateriale iperbolico. Dopo aver calcolato le permittività da mezzo efficace di questo sistema, la sua relazione di dispersione è presa in esame per mezzo di simulazioni nel dominio delle frequenze. L'accoppiamento con modi elettromagnetici a vettore d'onda elevato è preso in considerazione sia col metodo del prisma che col metodo del reticolo, confrontando il comportamento di un mezzo omogeneo iperbolico con quello di un multilayer. Nel quarto capitolo, vengono discusse le misure strutturali e ottiche di alcuni multilayer. Diverse tecniche sono state utilizzate per studiare la struttura dei multilayer, in modo da ottenere risultati indipendenti da ciascuna di esse e da studiare i vantaggi di ogni metodo. Per quanto riguarda invece le misure ottiche, l'ellissometria è stata utilizzata per attribuire delle permittività sperimentali ai multilayer, coerentemente con l'approssimazione di mezzo efficace. Misure di fotoluminescenza sono state realizzate per indagare la densità fotonica di stati del multilayer, studiando la variazione del tempo di vita di emettitori collocati in prossimità del sistema. La tecnica z-scan è stata usata per caratterizzare la risposta ottica nonlineare dei multilayer.

Introduction

The emerging field of metamaterials proposes a new paradigm to engineer the optical response of a system, even obtaining properties which are not found in conventional materials [1]. A metamaterial consists typically in a unit block repeated periodically through space, deriving its properties not only from its constituent materials, but also from their geometry. Under the hypothesis of features smaller than the operating wavelength, the electromagnetic response of the metamaterial is the result of the spatial average of this repeating pattern. This building principle allows to create systems with peculiar properties, such as negative-index metamaterials and nonlinear optical metamaterials.

Amongst different types of metamaterials, the class of hyperbolic metamaterials (HMMs) has gained interest in recent years for its properties which can be obtained even at optical frequencies [2]. HMMs are non-magnetic media characterized by a tensorial permittivity with principal components of different signs. This feature causes the isofrequency curve of a HMM to be hyperbolic instead of elliptical as in common materials. This means in turn that a HMM can sustain light modes with arbitrarily high wavevector, causing the photonic density of states in the medium to diverge. Unlike other types of metamaterials, HMMs have a non-resonant nature with a high figure of merit, can be realized with standard nanofabrication techniques, and their properties can be tuned easily across a broad spectrum. HMMs have been found interesting applications in biosensing [3], nonlinar optics [4], and light confinement [5], amongst other things.

The objective of this thesis is the study and realization of a hyperbolic metamaterial at visible and infrared frequencies. The design of a multilayer of alternating gold and alumina layers with subwavelength thicknesses was chosen to approximate a hyperbolic dispersion. Simulation in frequency domain were developed to study the validity of the effective medium approximation for thick and thin samples, and to evaluate the performance of a nanohole array as a coupling mechanism with the high-k modes of the system. Several multilayer samples were also fabricated and investigated experimentally with scanning and optical techniques.

The thesis is developed in four chapters. The first chapter resumes some notions of electromagnetism starting from Maxwell's equations, and examines the case of uniaxial media. The research field of metamaterials is then discussed starting from its first theoretical and experimental studies. The notion of hyperbolic metamaterials is introduced, and effective media approximation formula are derived for a multilayer. The problem of exciting high-k

modes is developed, considering both the coupling by prism and by grating. Eventually, the theory behind fluorescent emitters in proximity of interfaces and behind nonlinear optics is introduced. The second chapter describes the different experimental techniques which were employed in this thesis work, describing the experimental apparati and how each type of measure is carried on. Experimental methods included: the magnetron sputtering technique, which was used to fabricate the multilayer samples; several methodologies to investigate the samples' structure, such as atomic force microscopy, scanning electron microscopy, and X-ray reflectivity; several techniques to measure the optical properties of the multilayers, such as spectroscopic ellipsometry, z-scan technique, and photoluminescence measurements. The third chapter contains the results of the simulative study of a gold-alumina multilayer as an approximation of a hyperbolic metamaterial. After calculating the effective medium permittivities of this system, its dispersion relation is investigated by means of simulations in the frequency domain. The coupling with high-k modes is investigated both in the prism and in the grating mechanism, comparing the behavior of a true homogeneous hyperbolic medium with that of a multilayer. In the fourth chapter, structural and optical measurements made on a set of a different multilayers are discussed. Several techniques were implemented to study the structure of the multilayers, in order to get independent results and to investigate the advantages of each method. Ellipsometric measurements were used to assign experimental permittivities to the multilayers, in accordance with the effective medium approximation. Photoluminescence measurements were realized to probe the photonic density of states in a multilayer, which reduces the decay lifetimes of fluorescent emitters placed nearby. The z-scan technique was used to characterize the nonlinear optical response of the multilayers.

Chapter 1

Theory

1.1 Isotropic media

In the macroscopic formulation of the Maxwell's equations fields are averaged over many atomic distances, and the sources of these fields are continuous functions, namely the charge density ρ and the current density $\mathbf{j}$. The response of a medium to an electromagnetic field is described in terms of its macroscopic polarization density $\mathbf{P}$ and macroscopic magnetization density $\mathbf{M}$. The polarization density, or electric polarization, is the spatial density of electric dipole moments, whereas the magnetization density, or magnetic polarization, expresses the spatial density of magnetic dipole moments. From these quantities, one defines two auxiliary fields, the electric displacement $\mathbf{D}$ and the magnetic field $\mathbf{H}$:

$$\mathbf{D} = \varepsilon_0 \mathbf{E} + \mathbf{P}, \tag{1.1}$$

$$\mathbf{H} = \frac{1}{\mu_0}\mathbf{B} - \mathbf{M}. \tag{1.2}$$

The four fields $\mathbf{E}$, $\mathbf{B}$, $\mathbf{D}$, and $\mathbf{H}$ satisfy the Maxwell's macroscopic equations, which can be written as

$$\nabla \cdot \mathbf{D} = \rho_{ext}, \tag{1.3}$$

$$\nabla \cdot \mathbf{B} = 0, \tag{1.4}$$

$$\nabla \times \mathbf{E} = -\frac{\partial \mathbf{B}}{\partial t}, \tag{1.5}$$

$$\nabla \times \mathbf{H} = \mathbf{j}_{ext} + \frac{\partial \mathbf{D}}{\partial t}. \tag{1.6}$$

In this equations, the total charge and current densities are distinguished into external ($\rho_{ext}, \mathbf{j}_{ext}$) and internal ($\rho_{int}, \mathbf{j}_{int}$) contributes, with $\rho_{tot} = \rho_{int} + \rho_{ext}$ and $\mathbf{j}_{tot} = \mathbf{j}_{int} + \mathbf{j}_{ext}$ [6]. With this choice, one separates the external sources which drive the system from the internal sources which respond to the external stimuli. Taking in account all the components of the vector and scalar fields, these equations contain a total of 16 unknowns, each one a function of space and time.

Maxwell's equations only describe how the electromagnetic fields components are related, and how they originate from currents and charges in matter. Additional equations are

required to describe the response of a medium to the electromagnetic radiation. These equations, known as constitutive relations, connect the polarization density $\mathbf{P}$ and the magnetization density $\mathbf{M}$ to the electric field $\mathbf{E}$ and the magnetic induction $\mathbf{B}$, respectively. These relationships are established in terms of the electric susceptibility χ_e and the magnetic susceptibility χ_m. In the case of a non-dispersive, linear, and isotropic medium, the constitutive relations are

$$\mathbf{P} = \varepsilon_0 \chi_e \mathbf{E}, \tag{1.7}$$

$$\mathbf{M} = \chi_m \mathbf{H}. \tag{1.8}$$

Substituting Eq. (1.7) and (1.8) into (1.1) and (1.2), one obtains the following equations, directly relating the fundamental fields to the auxiliary ones:

$$\mathbf{D} = \varepsilon_0(1 + \chi_e)\mathbf{E} = \varepsilon_0 \varepsilon \mathbf{E}. \tag{1.9}$$

$$\mathbf{B} = \mu_0(1 + \chi_m)\mathbf{H} = \mu_0 \mu \mathbf{H}. \tag{1.10}$$

Two dimensionless quantities have been introduced: the dielectric constant (also known as relative permittivity, or dielectric function) $\varepsilon = 1 + \chi_e$, which is the permittivity of the material with respect to the permittivity of a vacuum; and the relative permeability $\mu = 1 + \chi_m$, which is the permeability of the medium relative to a vacuum. These parameters describe the coupling of the material to the electromagnetic field.

It's worth to notice that ε, μ, and σ are macroscopic parameters, which describe the response of the medium on a scale bigger than the atomic level. From these quantities, one can express other parameters, like the refractive index $\widetilde{n} = \sqrt{\mu\varepsilon}$ and the impedance $Z = \sqrt{\mu/\varepsilon}$ of the medium.

In this work only nonmagnetic media will be considered; therefore, from now on, μ is assumed to be a scalar quantity equal to 1.

In the general case, a medium is affected by spatial and temporal dispersion. Spatial dispersion causes the electric displacement field $\mathbf{D}$ in a point in space to be affected by values the electric field $\mathbf{E}$ assumes not only in that point, but in neighbouring points as well. Similarly, in a temporally dispersive medium, the values the electric field assumed in the past affect the values of the field $\mathbf{D}$ in the present. Spatial and temporal dispersion can be found in the optical response of metals, which depends on the wavevector $\mathbf{k}$ and the angular frequency ω of the electromagnetic radiation. For this reason, Eq, (1.9) can be generalized as follows:

$$\mathbf{D}(\mathbf{r}, t) = \varepsilon_0 \int\int \varepsilon(\mathbf{r} - \mathbf{r}', t - t')\mathbf{E}(\mathbf{r}', t')d\mathbf{r}'dt', \tag{1.11}$$

In order for this expression to be valid, all length scales must be larger than the lattice spacings of the material. The Fourier transform of this equation converts the convolutions over space and time into simple multiplications, giving the constitutive relation in the Fourier domain:

$$\mathbf{D}(\mathbf{k}, \omega) = \varepsilon_0 \varepsilon(\mathbf{k}, \omega)\mathbf{E}(\mathbf{k}, \omega), \tag{1.12}$$

For interactions of electromagnetic radiation with metals, spatial dispersion is usually neglected to simplify the description. Indeed, this assumption is strictly valid for small wavelengths up to the ultraviolet region ($\lambda \lesssim 100\ nm$), when the wavelength is larger than the relevant dimensions of the system, like the unit cell size and the mean free path of the electrons. In these cases the dielectric function $\varepsilon(\mathbf{k},\omega)$ is simplified to $\varepsilon(\mathbf{k}=\mathbf{0},\omega)=\varepsilon(\omega)$. From Eq. (1.12), temporal dispersion implies a dependency of the dielectric function on the angular frequency of light. It can be shown that temporal dispersion requires it to be also a complex-valued function $\widetilde{\varepsilon}(\omega)=\varepsilon_1(\omega)+i\varepsilon_2(\omega)$, and vice versa. This result follows by the principle of causality, as the medium's response to the electric field necessarily takes place after the electromagnetic radiation has interacted with it. From these considerations one can derive the Kramers-Kronig integral, which connects the real and imaginary parts of the complex dielectric function:

$$\varepsilon_1(\omega) = 1 + \frac{2}{\pi} P \int_0^{+\infty} \frac{\omega' \varepsilon_2(\omega')}{\omega'^2 - \omega^2} d\omega. \tag{1.13}$$

The symbol P indicates that the Cauchy principal value of the integral must be taken. The Kramers-Kronig relation implies that if the dielectric function is dispersive, it is also complex-valued, and vice versa. Furthermore, since the real and imaginary parts are strictly related, one could derive the values of the real part if the absorption spectrum is known. Examininng the denominator of the integrand, one further observes that absorption processes which take place at ω' far from ω do not contribute strongly to the dielectric function dispersion at ω. A relation similar to (1.13) can be written for the complex refractive index of the material $\widetilde{n}=\sqrt{\widetilde{\varepsilon}}$. In fact, $\widetilde{n}$ is a complex function of the angular frequency as well, namely $\widetilde{n}(\omega)=n(\omega)+i\kappa(\omega)$, with $n(\omega)$ being the (real) refractive index, and $\kappa(\omega)$ being the extinction coefficient of the material. In explicit form, the real and imaginary components of the dielectric function and the refractive index are related by the following expressions:

$$\varepsilon_1 = n^2 - \kappa^2, \tag{1.14}$$

$$\varepsilon_2 = 2n\kappa, \tag{1.15}$$

$$n^2 = \frac{\varepsilon_1}{2} + \frac{1}{2}\sqrt{\varepsilon_1^2 + \varepsilon_2^2}, \tag{1.16}$$

$$\kappa = \frac{\varepsilon_2}{2n}. \tag{1.17}$$

While the real refractive index n relates to the phase change of a wave propagating through the medium, the extinction coefficient κ is related to the attenuation of the field amplitude as it propagates. The attenuation of a light beam is usually expressed in terms of its intensity with the Beer's law,

$$I(x) = I_0 e^{-\alpha x}, \tag{1.18}$$

which describes the decrease in intensity of a light beam as it travels a distance x through the medium. The coefficient α is the absorption coefficient of the medium and in general depends on the light frequency. In a propagating monochromatic wave the electric

field is expressed in term of a phase term given by $exp[i\tilde{n}k_0x] = exp[i(n+i\kappa)k_0x] = exp(ink_0x)exp(-\kappa k_0x)$. Recalling that the light intensity is proportional to the square of the electric field, one finds the following expression relating the absorption coefficient to the extinction coefficient:

$$\alpha(\omega) = \frac{2\kappa(\omega)\omega}{c}. \tag{1.19}$$

The absorption coefficient has the dimension of the reciprocal of a length.
Since the optical response of a material is strictly related to its dielectric function, a classification of different materials can be made in terms of ε. For linear, isotropic, non-magnetic media, one usually distinguish between positive and negative values of $Re(\varepsilon)$. If $Re(\varepsilon) > 0$, which is the case for common dielectrics, the material is transparent to light. On the other hand, for negative values of $Re(\varepsilon)$, which are found for example in noble metals at optical wavelenghts, the waves in the medium are evanescent. It is worth studying the optical properties of these different types of materials and finding an analytical expression for their dielectric functions.

1.1.1 Metals

The optical response of metals is intimately related to the behaviour of the free electrons in the medium. A starting point for their description is given by the plasma model, in which one considers a gas of free electrons with density n, superimposed on a fixed lattice of positive ion nuclei. In this model, instead of describing explicitly the potentials due to the lattice and to the mutual electron interaction, one assigns to the electrons an effective mass m which reproduces the main characteristics of the band structure. The motion of electrons induced by electromagnetic radiation can be modeled in terms of a Lorentz harmonic oscillator, in which the electrons are free to move in the lattice and there is no restoring force or spring costant. Hence, the resonant frequency $\omega_0 = \sqrt{k/m}$ is actually zero, and no linear term compares into the differential equation. Electrons are put in motion by the external electric field $\mathbf{E}$, and collide with the lattice with a characteristic frequency $\gamma = 1/\tau$, where τ is the relaxation time of the free electron gas (typical values are $\gamma \sim 100THz$ and $\tau \sim 10^{-14}\ s$). Therefore, one can describe the motion of an electron subjected to an harmonic incident field with the differential equation

$$m\frac{d^2\mathbf{x}}{dt^2} + m\gamma\frac{d\mathbf{x}}{dt} = -e\mathbf{E}. \tag{1.20}$$

This plasma model is also referred to as the Drude free electron model. Considering an electric field $\mathbf{E} = \mathbf{E}_0 e^{-i\omega t}$ with harmonic time dependence, the differential equation admits the particular solution

$$\mathbf{x}(t) = \frac{e}{m(\omega^2 + i\gamma\omega)}e^{-i\omega t}. \tag{1.21}$$

The whole gas of free electrons, each one oscillating according to (1.21), gives rise to a macroscopic polarization $\mathbf{P} = -en\mathbf{x}$. Hence, substituting (1.21), one obtains an explicit expression for the polarization caused by the electric field,

$$\mathbf{P} = -\frac{ne^2}{m(\omega + i\gamma\omega^2)}\mathbf{E}. \tag{1.22}$$

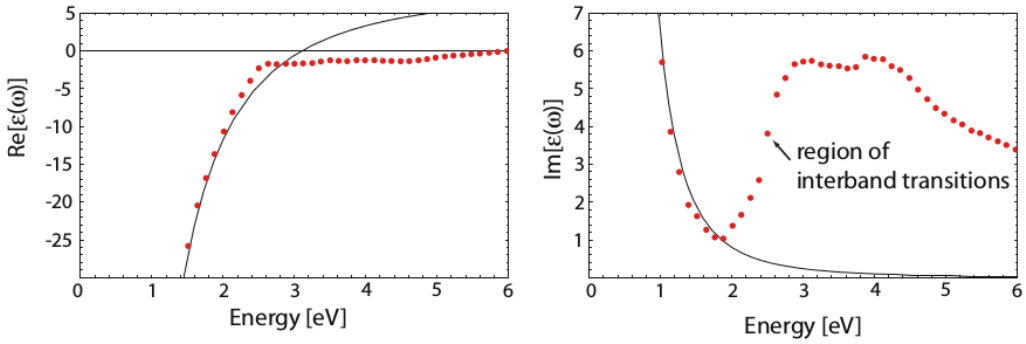

Figure 1.1: Comparison between experimental values for the the dielectric function $\varepsilon(\omega)$ of gold (red dots) and the values from the Drude model (solid black line) (image taken from [6]). The Drude model reproduce poorly the data at energies greater than the interband transition of gold.

Substituting this expression into (1.9), one finds

$$\mathbf{D} = \varepsilon_0 \left(1 - \frac{\omega_p^2}{\omega^2 + i\gamma\omega}\right) \mathbf{E}, \tag{1.23}$$

where the quantity $\omega_p = \sqrt{\frac{ne^2}{\varepsilon_0 m}}$ is called the plasma frequency of the particular free electron gas. Eventually, the description in terms of a plasma allows to determine an analytical expression for the complex dielectric function of a metal,

$$\varepsilon(\omega) = 1 - \frac{\omega_p^2}{\omega^2 + i\gamma\omega} = \left[1 - \frac{\omega_p^2\tau^2}{1 + \omega^2\tau^2}\right] + i\left[\frac{\omega_p^2\tau}{\omega(1 + \omega^2\tau^2)}\right]. \tag{1.24}$$

In the previous expression the real and imaginary part of the dielectric function have been explicitly separated for clarity. It is worth noting that one has to take in account the damping costant γ in order to have a non null imaginary term for the dielectric function. Since plasma frequencies reside deep in the ultraviolet region for noble metals (for Au it's $\omega_p \sim 2\ PHz$, corresponding to a wavelength of 138 nm), the analysis can be limited to the case $\omega < \omega_p$ for optical studies. Furthermore, if the frequency is large enough, such that $\omega\tau \gg 1$, the dielectric function can be approximated by the real expression

$$\varepsilon(\omega) = 1 - \frac{\omega_p^2}{\omega^2}. \tag{1.25}$$

On the contrary, for low frequencies in the limit $\omega\tau \ll 1$, one finds that $\varepsilon_2 \gg \varepsilon_1$, and the real and the imaginary part of the refractive index are approximately equal:

$$n \approx \kappa = \sqrt{\frac{\varepsilon_2}{2}} = \sqrt{\frac{\tau\omega_p^2}{2\omega}}. \tag{1.26}$$

It follows that in this regime metals are mainly absorbing, with an absorption coefficient given by the expression

$$\alpha = \sqrt{\frac{2\omega_p^2\tau\omega}{c^2}}. \tag{1.27}$$

The previous model was obtained under the assumption that all electrons in the metal are free and move inside the same outer conduction band. Therefore, it doesn't reproduce the optical response of a metal at frequencies which induce electron transitions between two energy levels belonging to different bands. These interband transitions become relevant at energies greater than 2 eV ($\lambda < 600\ nm$) for copper and gold, and for energies greater than 4 eV ($\lambda < 300\ nm$) for silver. Above these energies the imaginary part of the dielectric function increases in comparison with the free electron model. Corrections to the model are then required to describe the optical effect of these transitions. Each transition can be modeled classically, as a bound electron oscillating with a resonance frequency ω_i, corresponding to a particular interband transition with energy $\hbar\omega_i$.

$$m_i \frac{d^2\mathbf{x}}{dt^2} + m_i\gamma_i \frac{d\mathbf{x}}{dt} + m_i\omega_i^2\mathbf{x} = -e\mathbf{E}. \tag{1.28}$$

Several equations of this type can be considered to take in account different interband transitions, each one with a different resonance frequency. Solving theese equations, one finds that each bound oscillator contributes to the total dielectric function with a Lorentzian term

$$\varepsilon_i^{(b)}(\omega) = \frac{A_i^2}{\omega_i^2 - \omega^2 - i\gamma_i\omega}, \tag{1.29}$$

where the amplitude A_i is related to the density of bound electrons, ω_i is the resonance frequency of the interband transition, and ω is radiation frequency. Therefore, in the Drude-Lorentz model, the dielectric function of a metal is computed as the sum of several Lorentz terms, with the resonance frequence of one term (the Drude term) equal to zero:

$$\varepsilon(\omega) = \varepsilon^{(f)}(\omega) + \sum_i \varepsilon^{(b)}(\omega) = 1 - \frac{\omega_p^2}{\omega^2 + i\gamma\omega} + \sum_i \frac{A_i^2}{\omega_0^2 - \omega^2 - i\gamma_i\omega}. \tag{1.30}$$

Since most of the interband transitions reside in the UV spectrum, the dielectric function in the visible part can be approximated by evaluating the sum of the limits of the interband transition terms at $\omega \to 0$ ($\lambda \to \infty$). Hence these effects can be condensed into a constant term ε_∞:

$$\varepsilon(\omega) = \varepsilon_\infty - \frac{\omega_p^2}{\omega^2 + i\gamma\omega}. \tag{1.31}$$

The empirical values of ε_∞ for silver and gold are about 5 and 9, respectively. An interesting feature of this model is that the optical properties of a metal can be described with a good approximation using just three parameters: the long wavelengths contribute ε_∞, the plasma frequency ω_p, and the damping constant γ.

1.1.2 Dielectrics

In common optical systems, light is controlled by making it pass through transparent devices, whose interface surfaces are properly shaped. These devices are usually made of crystalline and glassy materials, which are dielectric. At optical frequencies, dielectric materials are usually much less dispersive than metals. Even so, one has to take in account

that strong resonances can be found both in the infrared region, because of the absoroption of phonons due to lattice vibrations, and in the ultraviolet regime, because of interband electron-hole transitions. These phenomena increase the dispersion of the material and therefore cause it to be absorptive around these frequencies. Similarly to the case of metals, these resonances can be modeled as

$$\varepsilon(\omega) = 1 + \sum_j \frac{S_j \omega_j^2}{\omega_j^2 - \omega^2 - i\omega\gamma_j}, \tag{1.32}$$

where ω_j is the resonance frequency of the jth mode, S_j represents its strength, and γ_j its damping constant. If the spectral range is limited to a region of low dispersion for the chosen dielectrics (which is usually the case of the visible region), a simpler expression can be used in which absorption is neglected. For dielectrics one usually expresss the optical response in terms of the refractive index. Hence, for dielectric materials with negligible attenuation coefficient (usually $\kappa < 10^{-5}$), the real refractive index calculated from (1.32) reduces to the Sellmeier dispersion formula:

$$n^2(\lambda) = 1 + \sum_j \frac{S_j \lambda^2}{\lambda^2 - \lambda_j^2}. \tag{1.33}$$

This equation is an empirical relationship, which was actually obtained by Sellmeier as an improvement on the Cauchy's equation $n(\lambda) = A + B\lambda^{-2} + C\lambda^{-4} + ...$, in which the refractive index is expressed as a power series approximation, with only negative even powers.

1.2 Anisotropic media

An optically anisotropic medium is a material whose optical properties depend on the direction along which they are measured. This anisotropy can be described in terms of a tensorial dielectric susceptibility $\widehat{\chi}$, from which it follows that the medium is characterized by a tensorial dielectric permittivity, $\widehat{\varepsilon} = 1 + \widehat{\chi}$. In an arbitrary reference frame, $\widehat{\varepsilon}$ can then be expressed as

$$\widehat{\varepsilon} = \begin{pmatrix} \varepsilon_{xx} & \varepsilon_{xy} & \varepsilon_{xz} \\ \varepsilon_{yx} & \varepsilon_{yy} & \varepsilon_{yz} \\ \varepsilon_{zx} & \varepsilon_{zy} & \varepsilon_{zz} \end{pmatrix}. \tag{1.34}$$

The constitutive relation (1.9) can be written as $\mathbf{D} = \widehat{\varepsilon}\mathbf{E}$ for an anisotropic medium. It follows that, in the general case, the fields $\mathbf{D}$ and $\mathbf{E}$ are not parallel. Instead, a component of $\mathbf{D}$ along a given direction will depend on all the components of $\mathbf{E}$:

$$\begin{cases} D_x = \varepsilon_0(\varepsilon_{xx}E_x + \varepsilon_{xy}E_y + \varepsilon_{xz}E_z) \\ D_y = \varepsilon_0(\varepsilon_{yx}E_x + \varepsilon_{yy}E_y + \varepsilon_{yz}E_z) \\ D_z = \varepsilon_0(\varepsilon_{zx}E_x + \varepsilon_{zy}E_y + \varepsilon_{zz}E_z) \end{cases} \tag{1.35}$$

Nonetheless, for every anisotropic medium one can always find three orthogonal directions, called the principal axes or optical axes of the medium, with the property that, given an

electric field polarized along one of these directions, the displacement field will be parallel to it. Consequentially, if one chooses a reference frame whose axes are parallel to the principal axes of the medium, the dielectric tensor can be diagonalized as

$$\widehat{\varepsilon} = \begin{pmatrix} \varepsilon_x & 0 & 0 \\ 0 & \varepsilon_y & 0 \\ 0 & 0 & \varepsilon_z \end{pmatrix}, \tag{1.36}$$

and the components of $\mathbf{D}$ and $\mathbf{E}$ are related by

$$\begin{cases} D_x = \varepsilon_0 \varepsilon_x E_x \\ D_y = \varepsilon_0 \varepsilon_y E_y \\ D_z = \varepsilon_0 \varepsilon_z E_z \end{cases} \tag{1.37}$$

The three principal components, ε_x, ε_y, and ε_z, depend on the light frequency. For anisotropic materials with a tensorial dielectric function, the magnetic permeability can still be a scalar, and it will be considered equal to one in the following analysis. Depending on the values of the principal components, the medium is said to be isotropic if the three components coincide, uniaxial if two components coincide but differ from the third, and biaxial if the three components have three distinct values. The following analysis is limited to the case of a uniaxial material, in which $\varepsilon_x = \varepsilon_y = \varepsilon_\parallel$, while $\varepsilon_z = \varepsilon_\perp \neq \varepsilon_\parallel$.
The notation adopted throughout this thesis for the subscripts of the principal components refers to the x-y plane perpendicular to the optical axis, rather than the optical axis itself. Therefore, $\varepsilon_\parallel$ is the permittivity of waves whose direction of polarization is contained in the x-y plane, whereas $\varepsilon_\perp$ is the permittivity of waves polarized perpendicularly to it. The reason for this choice will be cleared afterwards.
To describe the propagation of electromagnetic waves into the material, Eq. (1.5) and (1.6) can be rewritten for an anisotropic material, namely

$$\nabla \times \mathbf{E} = -\frac{\partial \mathbf{B}}{\partial t}, \tag{1.38}$$

$$\nabla \times \mathbf{H} = \frac{\partial \mathbf{D}}{\partial t}. \tag{1.39}$$

Considering a plane wave of the form $e^{i(\omega t - \mathbf{k}\cdot\mathbf{r})}$ propagating into the optically anisotropic medium, the two equations can be written as

$$-\mathbf{k} \times \mathbf{H} = \omega \varepsilon_0 \widehat{\varepsilon} \cdot \mathbf{E}, \tag{1.40}$$

$$\mathbf{k} \times \mathbf{E} = \mu_0 \omega \mathbf{H}. \tag{1.41}$$

Combining the two equations, one obtains the following wave equation,

$$\frac{1}{\varepsilon_0 \mu_0 \omega^2} [\mathbf{k} \times (\mathbf{k} \times \mathbf{E})] = -\widehat{\varepsilon} \cdot \mathbf{E}. \tag{1.42}$$

This equation can be further developed by using the vector calculus identity $\mathbf{k} \times \mathbf{k} \times \mathbf{E} = \mathbf{k}(\mathbf{k} \cdot \mathbf{E}) - k^2\mathbf{E}$, and substituting $c^2 = (\varepsilon_0\mu_0)^{-1}$. It follows that

$$\mathbf{k}(\mathbf{k} \cdot \mathbf{E}) = k^2\mathbf{E} - \frac{\omega^2}{c^2}\widehat{\varepsilon} \cdot \mathbf{E}. \tag{1.43}$$

This vector equation correspond to a homogeneous system for the components E_x, E_y, E_z of the electric field. Explicitly:

$$\begin{cases} k_x(k_xE_x + k_yE_y + k_zE_z) = \left(k^2 - \frac{\omega^2}{c^2}\varepsilon_\parallel\right) E_x \\ k_y(k_xE_x + k_yE_y + k_zE_z) = \left(k^2 - \frac{\omega^2}{c^2}\varepsilon_\parallel\right) E_y \\ k_z(k_xE_x + k_yE_y + k_zE_z) = \left(k^2 - \frac{\omega^2}{c^2}\varepsilon_\perp\right) E_z \end{cases} \tag{1.44}$$

which can be rewritten as

$$\begin{cases} \left[k_x^2 - \left(k^2 - \frac{\omega^2}{c^2}\varepsilon_\parallel\right)\right] E_x + k_xk_yE_y + k_xk_zE_z = 0 \\ k_yk_xE_x + \left[k_y^2 - \left(k^2 - \frac{\omega^2}{c^2}\varepsilon_\parallel\right)\right] E_y + k_yk_zE_z = 0 \\ k_zk_xE_x + k_zk_yE_y + \left[k_z^2 - \left(k^2 - \frac{\omega^2}{c^2}\varepsilon_\perp\right)\right] E_z = 0 \end{cases} \tag{1.45}$$

Nontrivial solutions for the electric field in the medium can be found by setting the determinant of the system equal to 0. Thus, the characteristic equation of the system of equations (1.45) can be factored as

$$\left[\frac{\omega^2}{c^2}\varepsilon_\parallel - k^2\right] \left[\frac{\omega^4}{c^4}\varepsilon_\parallel\varepsilon_\perp - \frac{\omega^2}{c^2}\varepsilon_\parallel(k_x^2 + k_y^2) - \frac{\omega^2}{c^2}\varepsilon_\perp k_z^2\right] = 0. \tag{1.46}$$

Consequentially, equation 1.46 corresponds to two separate equations, which describe two distinct sets of waves propagating through the medium. The first equation is given by

$$\frac{\omega^2}{c^2}\varepsilon_\parallel = k^2 \tag{1.47}$$

It represents the dispersion relation for ordinary waves, or Transverse Electric (TE) waves, which are electromagnetic waves whose electric field is polarized in the perpendicular direction with respect to the optical axis. For TE waves the wavelength and the medium permittivity do not depend on the direction of the wave vector, as the permittivity for TE waves is equal to $\varepsilon_\parallel$. The other equation can be written as

$$\frac{\omega^2}{c^2} = \frac{k_x^2 + k_y^2}{\varepsilon_\perp} + \frac{k_z^2}{\varepsilon_\parallel}. \tag{1.48}$$

This equation is the dispersion relation for extraordinary waves, or Transverse Magnetic (TM) waves, which are waves whose magnetic field is perpendicular to the optical axis. Therefore, the electric field of TM waves has a non null component orientated along the optical axis. For these waves the wavelength and permittivity depend on the direction of propagation. If θ is angle between the optical axis and the direction of propagation of the TM wave, the permittivity for the TM wave is given by

$$\varepsilon_{TM}(\theta) = \frac{\varepsilon_\parallel\varepsilon_\perp}{\varepsilon_\parallel sin^2\theta + \varepsilon_\perp cos^2\theta}. \tag{1.49}$$

1.3 Metamaterials

In order to control and manipulate light, optical devices are designed with an accurate choice of their constituent materials and the shapes they are given, especially at the interfaces. A certain material is adopted mainly because of its optical constants, which are expressed in terms of its dielectric function. It would then be desirable to have a large space of parameters, in which one could choose a material with an arbitrary value of its dielectric function. This space of parameters is in fact limited by the finite number of materials which are found in nature, and which was only partially enlarged by the development of artificial materials.

A new approach to the research of new electromagnetic properties is given by the emerging field of metamaterials [1, 7]. A metamaterial is an artificial engineered device, composed of well-arranged functional elements with subwavelength dimensions and mutual distances, usually arranged in a periodic pattern. Each of these "meta-atoms" consists of a carefully designed structure, composed of common materials, whose dimensions are many orders of magnitude bigger than the molecular scale. Even so, if the inhomogeneity of the artificial structure is subwavelength, the system can be considered homogeneous with respect to its interaction with light. The properties of a metamaterial depend not only on the choice of the materials from which it's built, but mostly from the structure of its unit cell. Metamaterials are usually made combining metal and dielectric materials, whereas analogous structures composed only of dielectrics are called photonic crystals.

The fact that the system results to be macroscopically homogeneous leads to considering it as a new material in itself, instead of a device. The fundamental condition for the homogeneity of the structure is that the characteristic length a of the system (i.e., the length of the meta-atoms, or their mutual distance) must be smaller than the wavelength of interest: $a \ll \lambda$. When this condition holds, the interaction of light with the system can be averaged over many meta-atoms, similarly to how the macroscopic electric field is the average of the microscopic electric field over many atoms in a common material. Thus, it is possible to associate macroscopic parameters to the metamaterial, like an effective dielectric permittivity and an effective refractive index. The fundamental and interesting concept is that the meta-atoms of a metamaterial can be engineered in a precise way to obtain desired electromagnetic properties with regards to the whole system. Hence, the development of new metamaterials enables to explore the space of parameters $\{\varepsilon, \mu, ...\}$, achieving properties which are not offered by any existing material.

It is worth noticing that, since meta-atoms are built from dispersive materials, the resulting metamaterial will be dispersive as well. Furthermore, depending on the particular structure, a metamaterial can exhibit strong anisotropy.

The first paper adopting the term "metamaterial" was published in 2000 by Smith et al. [8]. In this seminal paper, they reported the experimental realization of a metamaterial exhibiting simultaneous negative values of the effective dielectric permeability and magnetic permeability in the microwave spectrum. The metamaterial was composed of a periodic

array of conducting nonmagnetic split ring resonators and wires, in which resonance effects were employed to achieve the wanted optical response.
The structure realized by Smith et al. was actually the experimental validation of Veselago's theoretical study [9] on left-handed materials, which dates back to 1968. In this paper, Veselago studied the properties of an hypothetical material having both a negative permittivity ε and a negative permeability μ. Most materials in nature show both a positive permeability and a positive permittivity across all the spectrum (with non-magnetic materials having $\mu \simeq 1$). Lossless materials exist in which either ε or μ is negative (but not both), and they are opaque to electromagnetic radiation, as $n = \sqrt{\varepsilon\mu}$ is purely imaginary. This is the case of noble metals, which have $\varepsilon < 0$ at optical wavelengths, and in which light can penetrate only up to a finite length. On the other hand, if simultaneously $\varepsilon < 0$ and $\mu < 0$, the refractive index results to be purely real, and propagation through the medium is allowed. Additionally, it can be shown that the refractive index has to be taken with a negative sign in order for causality to hold. For this reason, these materials are usually called Negative Index Materials (NIMs).
To explain why the refractive index would be negative, one can consider a monochromatic electromagnetic wave described by a phase term $exp[i(\mathbf{k}\cdot\mathbf{x} - \omega t)]$, with wavevector $\mathbf{k}$ and frequency ω. By definition the wavevector is normal to the wavefronts, which are the surfaces of constant phase, and indicates the direction of phase velocity. On the other hand, the Poynting vector $\mathbf{S} = \mathbf{E} \times \mathbf{H}$ is oriented along the direction of energy flow, which coincides with the direction of the group velocity. This direction is what is usually referred to as the direction of wave propagation. A relationship between the fields $\mathbf{E}$, $\mathbf{H}$, and $\mathbf{k}$ can be obtained by considering the curl Maxwell's equations (1.5) and (1.6):

$$\begin{cases} \mathbf{k} \times \mathbf{E} = \frac{\omega}{c}\mu_0\mu\mathbf{H} \\ \mathbf{k} \times \mathbf{H} = \frac{\omega}{c}\varepsilon_0\varepsilon\mathbf{E} \end{cases} \tag{1.50}$$

In materials for which both ε and μ are positive, or only one of them is negative, these equations cause the triad $(\mathbf{E}, \mathbf{H}, \mathbf{k})$ to be right-handed. This is the common situation, in which the Poynting vector is parallel to the wavevector $\mathbf{k}$. If instead a material with $\varepsilon < 0$ and $\mu < 0$ is considered, one obtains that the triad $(\mathbf{E}, \mathbf{H}, \mathbf{k})$ is left-handed, and $\mathbf{S}$ is anti-parallel to $\mathbf{k}$. This property has important consequences when the refraction at the interface between a positive index material (PIM) and a NIM is considered, with light coming from the PIM. As in the incidence medium the wavevector and the Poynting vector are parallel, they are both oriented towards the interface. As the beam is transmitted through the interface, the Poynting vector in the NIM points away from the interface, while the wavevector, oriented in the opposite direction, points towards it. Since the tangential component of the wavevector must be preserved at the interface (as a consequence of the continuity of the tangent component of the electric field), one concludes that the transmitted beam must propagate at a negative angle of refraction. Nonetheless, assuming the refractive index of the NIM to be negative, the refraction is still expected to adhere to Snell's law, $n_1 sin\theta_i = n_2 sin\theta_t$.

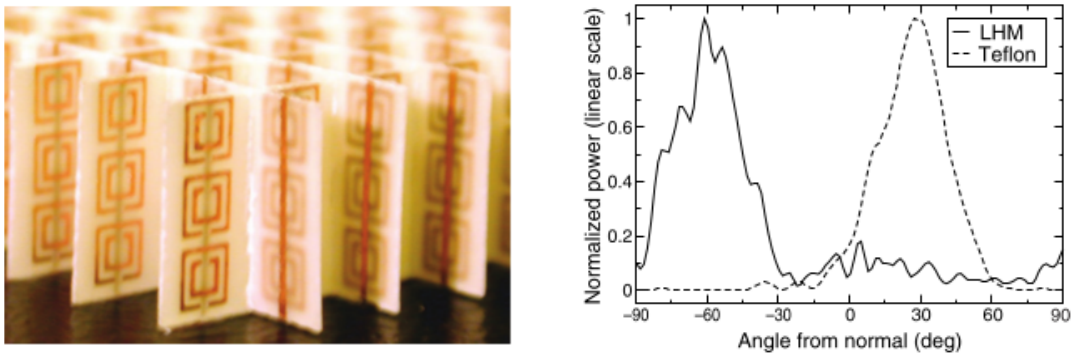

Figure 1.2: On the left, a detail of the metamaterial studied by Shelby et al. [10] to have a left handed material (LHM) at microwave frequencies. On the right, transmittance spectra measured for the LHM and for a comparison Teflon sample show that the LHM refracts microwaves at negative angles

This effect was experimentally demonstrated in 2001 by Shelby et al. [10]. Their metamaterial (Fig. 1.2) consisted in a two-dimensionally periodic array of copper split ring resonators and wires, fabricated on a 0.25 mm fiber glass circuit board material by means of an etching technique. The lattice had a spacing of 5 mm, and the metamaterial was built to work in the microwave regime at $\lambda \simeq 3$ cm. The metamaterial was cut into a prism-like shape, to have microwaves entering perpendicularly on one interface and have incidence at non-normal angle at the other. The trasmitted power measured as a function of transmission angle showed unambiguously that microwaves were refracted at a negative angle, corresponding to a negative refractive index $n = -2.7$.

The experimental proof of the reality of NIMs led to the study of unforeseen applications. For example, Pendry [11] observed that a slab of negative refractive index material would act as a "superlens", which would focus evanescent waves together with propagating waves, thus surpassing the diffraction limit which holds for common lenses.

Although the first experimental studies focused on the realization of metamaterials exhibiting negative refraction, the field of metamaterials today has a broader scope. Among the active areas of research, metamaterials are studied with regards to optical sensing, nonlinear optics, photonic circuits, super effects, and electromagnetic cloaks of invisibility.

1.4 Hyperbolic metamaterials

An hyperbolic metamaterial (HMM) is an anisotropic uniaxial medium, characterized by a tensorial dielectric permittivity whose principal components have opposite signs [12] [2]. A few natural materials showing this property actually exist [13], but they are rather rare and work only at Terahertz and far-infrared frequencies. To obtain an hyperbolic system with precise characteristics and working at the wanted spectral range, one usually recurs to a carefully designed metamaterial. If a reference frame is chosen with the z-axis parallel to the optical axis, one has $\varepsilon_x = \varepsilon_y$, and the dielectric permittivity can be

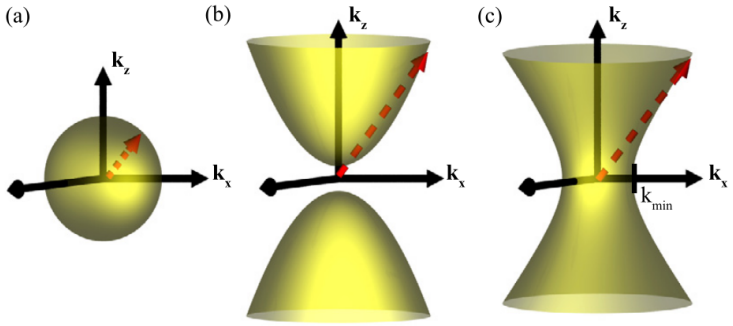

Figure 1.3: Isofrequency surfaces in k-space for different types of materials (images taken from [2]). Waves propagating in an isotropic medium (or ordinary waves in a uniaxial medium) are characterized by a spherical isofrequency contour (a). In the case of extraordinary waves propagating in hyperbolic mediums, the isofrequency surfaces open up into hyperboloids: a type I HMM ($\varepsilon_{\parallel} > 0$ and $\varepsilon_{\perp} < 0$) is the dispersion relation describes a two-sheeted hyperboloid (b), whereas a type II HMM ($\varepsilon_{\parallel} < 0$ and $\varepsilon_{\perp} > 0$) is characterized by a one-sheeted hyperbolid (c). Dotted red arrows are possible wavevectors which correspond to propagating waves in the medium. In the case of type II HMMs, a minimum value for the parallel component of the wavevector is required to have a propagating wave.

diagonalized as

$$\widehat{\varepsilon} = \begin{pmatrix} \varepsilon_{\parallel} & 0 & 0 \\ 0 & \varepsilon_{\parallel} & 0 \\ 0 & 0 & \varepsilon_{\perp} \end{pmatrix}, \tag{1.51}$$

with $\varepsilon_{\parallel}\varepsilon_{\perp} < 0$.

The defining property of an HMM can be interpreted as saying that an HMM has dielectric properties in one direction and metallic properties in the orthogonal one, so that free electrons are constrained only in one or two spatial directions. The adjective "hyperbolic" stems from a geometrical consideration of the dispersion equation for TM waves in a uniaxial medium (1.48), evaluated at a fixed frequency. For an isotropic medium ($\varepsilon_{\parallel} = \varepsilon_{\perp}$), the isofrequency surfaces in the k-space for ordinary waves are spherical surfaces. For a classic uniaxial crystal, with positive principal components $\varepsilon_{\parallel} \neq \varepsilon_{\perp}$, isofrequency surfaces for TM waves are ellipsoids of revolution. Instead, if the two principal components have different signs, the isofrequency surfaces open up into hyperboloids. A fundamental distinction between different types of HMMs can be made, depending on how many principal components are negative. If $\varepsilon_{\parallel} > 0$ and $\varepsilon_{\perp} < 0$, the isofrequency surface is a two-sheeted hyperboloid, and the HMM is said to be of Type I. Instead, if $\varepsilon_{\parallel} < 0$ and $\varepsilon_{\perp} > 0$, the isofrequency surface is a one-sheeted hyperboloid, and the medium is a Type II HMM. It is worth examining the dispersion relations for TE and TM waves for both Type I and Type II HMMs. For semplicity, the x-z plane is chosen as the plane of incidence, so that $k_y = 0$ and $k_{\parallel} = k_y$.

HMMs of Type I ($\varepsilon_{\parallel} > 0$ and $\varepsilon_{\perp} < 0$) can sustain both ordinary and extraordinary waves in their propagating form. Ordinary TE waves are affected by a positive permittivity $\varepsilon_{\parallel}$, which does not depend on the angle of propagation. As regards extraordinary TM waves,

their dispersion relation allows a real k_z for every value of k_x, with a minimum absolute value of $k_z = \sqrt{\varepsilon_\parallel} k_0$ for $k_x = 0$. Henceforth, waves with $k > k_0 = \omega/c$, which would be evanescent in air, are able to propagate in a Type I HMM.
HMMs of Type II ($\varepsilon_\parallel < 0$ and $\varepsilon_\perp > 0$) behave like a metal with negative $\varepsilon_\parallel$ for ordinary TE waves. The isofrequency hyperbola for TM waves at a given ω crosses the x-axis at $k_x = \pm\sqrt{\varepsilon_\perp} k_0$, determining the smallest wavevector which can propagate within the structure. Therefore, a Type II HMM allows only the propagation of TM high-k modes, whereas propagating modes in air are evanescent in the metamaterial, as typically $\sqrt{\varepsilon_\perp} > 1$.
Both types of HMMs have the capacity to sustain high-k modes. This property is of great interest, as high-k modes, which are evanescent in common dielectrics, carry information about details smaller than the diffraction limit. This property, combined with a suitable geometry, has led to the theoretization of hyperlenses [14], which would be able to convert high-k waves inside the metamaterial into low-k waves at its outer interface.

1.5 Effective Medium Approximation of a Multilayer

Hyperbolic dispersion is not found in nature at optical frequencies. Nonetheless, it can be reproduced with nanostructured engineered metamaterials. A possible implementation of a metamaterial, which can give rise to hyperbolic dispersion, consists of a periodically layered composite (multilayer) built alternating thin layers of different materials. In the limit in which the thin film thicknesses are small with respect to the wavelength, this structure can be described in terms of an effective medium approximation (EMA), with a spatially averaged anisotropic effective permittivity assigned to it. Additionally, since the structure is azimuthally isotropic, in the effective medium approximation it will behave as a uniaxial crystal, with two principal components having the same value and with its optical axis oriented perpendicularly to the thin films. If two isotropic constituent materials with dielectric permittivities ϵ_1 and ϵ_2 of opposite signs are used, namely a metal and a dielectric, the hyperbolic dispersion can be obtained.
An ideal multilayer is considered as extending indefinitely in the plane of the interfaces between each layers, and having layers periodically repeating in the perpendicular direction. The ratio between the two constituent materials can be expressed in terms of the filling fraction of the first material, $\rho_1 = h_1/(h_1 + h_2)$, where h_1 and h_2 are the heights of the layers of the first and the second material, respectively. It follows immediately that the second material's filling fraction is $\rho_2 = 1 - \rho_1 = h_2/(h_1 + h_2)$. One assumes that the layer thicknesses are much smaller than the wavelength of light propagating into the multilayer, $h_1 + h_2 \ll \lambda$, so that the metamaterial effective medium approximation holds.
In each layer the constitutive relation between the electric displacement field and the electric field, see Eq. (1.9), must hold:

$$\begin{cases} \mathbf{D}_1 = \varepsilon_0 \varepsilon_1 \mathbf{E}_1, \\ \mathbf{D}_2 = \varepsilon_0 \varepsilon_2 \mathbf{E}_2. \end{cases} \tag{1.52}$$

A similar equation applies to the system when it is described as an homogeneous effective medium. Using the subscript 'e' to indicate a spatially averaged effective parameter or effective field, and considering a tensorial dielectric function, one can write

$$\mathbf{D}_e = \varepsilon_0 \widehat{\varepsilon}_e \mathbf{E}_e. \tag{1.53}$$

In order to find an expression for the dielectric permittivity of the metamaterial, one can consider two independent cases in which only one principal component is taken into account: when the electric field is polarized along the planar interfaces (and perpendicularly to the optical axis), and when the electric field is perpendicular to the thin films (parallel to the optical axis).
When the polarization of the electric field is parallel to the thin films, the continuity condition for the tangential component of the electric field at an interface must be taken into account. The electric field thus remains constant between two layers across the whole multilayer, so that it will be equal to the effective electric field:

$$E_1 = E_2 = E_e. \tag{1.54}$$

The electric displacement field, which is oriented along the interfaces as well, changes from layer to layer. Nonetheless, in the hypothesis of thin films one can consider the electric displacement field in the effective medium as the spatial average on two constituent layers, which results to be

$$D_e = \rho_1 D_1 + (1-\rho_1) D_2. \tag{1.55}$$

Substituting D_1 and D_2 using the constitutive relations of each layer, one finds that

$$\begin{aligned} D_e &= \varepsilon_0 \rho_1 \varepsilon_1 E_e + \varepsilon_0 (1-\rho_1) \epsilon_2 E_e \\ &= \varepsilon_0 \left[\rho_1 \varepsilon_1 + (1-\rho_1)\varepsilon_2\right] E_e \\ &= \varepsilon_0 \varepsilon_{\parallel} E_e. \end{aligned} \tag{1.56}$$

Therefore, the effective permittivity for waves polarized along the thin film interfaces results to be the weighted average of the dielectric permittivities of the layers, where the weights are the filling factors of the two materials (weighted arithmetic mean):

$$\varepsilon_{\parallel} = \rho_1 \varepsilon_1 + (1-\rho_1)\varepsilon_2. \tag{1.57}$$

With a similar reasoning, a different expression can be obtained for the effective permittivity of waves polarized perpendicularly to the layers. In this case the electric field is not preserved from one layer to the other. Therefore, the effective electric field can be expressed as the spatial average

$$E_e = \rho_1 E_1 + (1-\rho_1) E_2. \tag{1.58}$$

On the other hand, since the electric displacement field is perpendicular to the layers, in absence of surface charges it must be continuous at the boundaries. It is therefore constant across the whole multilayer, so that

$$D_1 = D_2 = D_e. \tag{1.59}$$

Considering the constitutive relation between the effective fields, one finds that

$$\begin{aligned} E_e &= \rho_1 \frac{D_e}{\varepsilon_1} + (1-\rho_1)\frac{D_e}{\varepsilon_2} \\ &= \left(\frac{\rho_1}{\varepsilon_1} + \frac{1-\rho_1}{\varepsilon_2}\right) D_e \\ &= \frac{D_e}{\varepsilon_\perp}. \end{aligned} \tag{1.60}$$

Therefore, one finds that the reciprocal of the effective permittivity for waves polarized perpendicularly to the layers is equal to the weighted average of the reciprocals of the permittivities of the two materials, where the weights are the filling factors of the two materials (weighted harmonic mean). Explicitly, one has

$$\varepsilon_\perp = \frac{\varepsilon_1 \varepsilon_2}{(1-\rho_1)\varepsilon_1 + \rho_1 \varepsilon_2}. \tag{1.61}$$

Because of the azimuthal simmetry of the multilayer, one can choose a set of orthogonal axes with x- and y- axes parallel to the layers and the z-axis perpendicular to them. In this reference frame, the permittivity tensor can be diagonalized as in eq. (1.51).
The formulas obtained for the components of the permittivity tensor can be immediately generalized to the case of a multilayer with more than two materials periodically repeating themselves. Using the subscript i to indicate the i-th material, one can write the effective permittivities as

$$\varepsilon_\parallel = \sum_i \rho_i \varepsilon_i, \tag{1.62}$$

$$\varepsilon_\perp^{-1} = \sum_i \rho_i \varepsilon_i^{-1}, \tag{1.63}$$

given that the condition $\sum_i \rho_i = 1$ is fulfilled.
An alternate approach to obtain the formulas (1.57) and (1.61) is based on describing the multilayer as an homogeneous medium using Bruggeman's effective medium theory [15] with a screening parameter κ. The implicit expression for the effective permittivity ε of a medium composed of two constituents would then be

$$\rho_1 \frac{\varepsilon_1 - \varepsilon}{\varepsilon_1 + \kappa\varepsilon} + \rho_2 \frac{\varepsilon_2 - \varepsilon}{\varepsilon_2 + \kappa\varepsilon} = 0. \tag{1.64}$$

The parameter κ accounts for non-spherical inclusions, which cause a different screening of the external field depending on the direction of polarization. In the extreme case where the inclusions are actually parallel thin films, the screening parameter diverges to infinity when all the boundaries of the composites are parallel to the electric field and there is zero screening, whereas it equals zero if the boundaries are perpendicular to the electric field and there is full screening. Therefore, setting $\kappa \to \infty$ in (1.64) one re-obtains the expression (1.57) for the effective permittivity in the parallel direction, while setting $\kappa = 0$ gives the same expression as in (1.61).
The derivation of the effective permittivities through Brugemann's effective medium theory shows that the expressions for the permittivity in the parallel and in the perpendicular

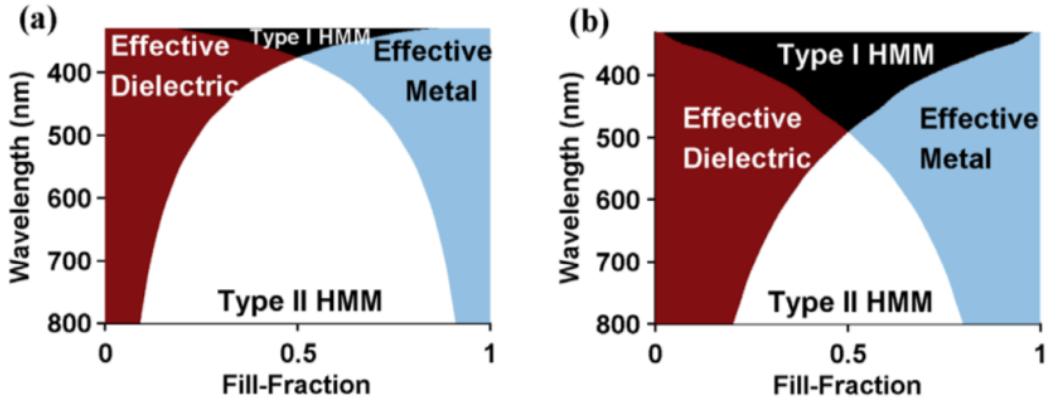

Figure 1.4: Optical phase diagrams as functions of metallic fill-fraction and wavelength for metal-dielectric multilayers described by EMA. The two graphs (images taken from [2]) show the behavior for (a) a Ag/Al_2O_3 multilayer system and (b) a Ag/TiO_2 multilayer system.

direction represent the upper and lower bounds for the effective permittivity of the composite, as they correspond to the case of zero screening ($\kappa \to \infty$) and full screening ($\kappa = 0$). As these properties were first studied in 1912 by Otto Wiener, the expressions formulas (1.57) and (1.61) are also referred to as Wiener bounds.

The expressions for the effective parameters (1.57) and (1.61) show that one can reproduce particular values of the permittivity by appropriately choosing the constituent materials and their filling fraction. Being interested in realizing an HMM, one would be interested in having $\varepsilon_{\parallel}$ and $\varepsilon_{\perp}$ of different signs. This is usually obtained choosing a metal and a dielectric constituent. Nonetheless, one could also obtain an effective dielectric medium, with both positive $\varepsilon_{\parallel}$ and $\varepsilon_{\perp}$, or an effective metallic medium, with both negative $\varepsilon_{\parallel}$ and $\varepsilon_{\perp}$. Furthermore, one has to remember that, as the constituent materials are dispersive, $\varepsilon_1 = \varepsilon_1(\omega)$, $\varepsilon_2 = \varepsilon_2(\omega)$, the effective parameters will be dispersive as well, $\varepsilon_{\parallel} = \varepsilon_{\parallel}(\omega)$, $\varepsilon_{\perp} = \varepsilon_{\perp}(\omega)$. This implies that an homogenous effective medium can have transitions between different optical phases across the spectrum when either of the principal components change sign, see Fig. 1.5. The choice of materials is thus related also to the portion of the electromagnetic spectrum in which one wants to observe an hyperbolic dispersion. To operate at optical frequencies one usually combines a noble metal (e.g., Au or Ag) with an high-index dielectric (e.g., TiO_2, or Al_2O_3).

Some interesting properties can be expected by looking at the formulas for the effective permittivity. If the constituent materials have low losses ($Im(\varepsilon_{1,2}) \simeq 0$), the in-plane permittivity is expected to approach zero when the relationship $\rho_1/\rho_2 = -\varepsilon_2/\varepsilon_1$ is fulfilled at a given wavelength. Because of the negative value on the right side of the equation, this relationship can hold only when a dielectric and a metal constituent are used together. On the other hand, when the relationship $\rho_1/\rho_2 = -\varepsilon_1/\varepsilon_2$ is realized instead, the out-of-plane is expected to diverge. The development of metamaterials with permittivities such as $\varepsilon = 0$ and $\varepsilon = \infty$ is of great interest in the field of photonic nanocircuits, where they can be used as insulating or conducting elements, respectively.

1.5.1 EMA as approximation of Transfer Matrix Method

Expression (1.57) and (1.61) have been obtained under the general metamaterial condition of having characteristic lengths smaller than the light wavelength: $h_1+h_2 \ll \lambda$. On a closer look, a stronger condition must hold for this description to be valid in the case of an HMM. In fact, one of the most interesting properties of an ideal HMM is the capacity to sustain high-k modes as propagating modes. If at a given frequency ω the wavevector in the HMM is bigger than the corresponding wavevector in air, the resulting wavelength will be smaller in the HMM. This implies that an effective medium realization of a HMM is not capable of sustaining arbitrarily high-k modes. Instead, the effective medium approximation becomes less and less efficient as the considered wavevector increases.
In order to study the limits of this approximation, one can resort to finding an exact solution for the propagation of waves in a multilayer structure, by means of a transfer matrix method [16]. Assuming lossless materials, an infinitely periodic multilayer can sustain certain modes called Bloch waves. The dispersion relation for these modes is found to be

$$cos[k_z(h_1+h_2)] = cos(k_{1,z}h_1)cos(k_{2,z}h_2) - \gamma_j sin(k_{1,z}h_1)sin(k_{2,z}h_2), \tag{1.65}$$

where $k_{i,z} = \varepsilon_i\omega^2/c^2 - k_y^2$ is the wavevector component along the z-axis for the layer $i = 1, 2$, and γ_j depends on the wave polarization ($j = TE, TM$), namely

$$\gamma_{TE} = \frac{1}{2}\left(\frac{\varepsilon_1}{\varepsilon_2} + \frac{\varepsilon_2}{\varepsilon_1}\right), \tag{1.66}$$

$$\gamma_{TM} = \frac{1}{2}\left(\frac{\varepsilon_1 k_{1,z}}{\varepsilon_2 k_{2,z}} + \frac{\varepsilon_2 k_{2,z}}{\varepsilon_1 k_{1,z}}\right). \tag{1.67}$$

The Taylor expansion of the trigonometric functions up to the second order in

$$\begin{cases} |k_{1,z}h_1| \ll 1 \\ |k_{2,z}h_2| \ll 1 \\ |k_z(h_1+h_2)| \ll 1 \end{cases} \tag{1.68}$$

leads to two dispersion relations of the form (1.47) and (1.48), in which the principal components of the dielectric function coincide with the EMA formulas (1.57) and (1.61). The conditions in (1.68) constitute a stronger constraint than the metamaterial condition $h_1 + h_2 \ll \lambda$, and represent a fundamental limit to the efficiency of an HMM.
The description of the multilayer system by means of the transfer matrix method allows to study different degrees of approximation, by expanding (1.65) up to higher orders. For example, by expanding it to the next nonvanishing Taylor term, one can account for the spatial dispersion in the HMM [17]. Using the superscript (0) to refer to previous lower order effective parameters, and the superscript (1) for higher order ones, one finds

$$\varepsilon_\perp^{(1)}(\mathbf{k},\omega) = \frac{\varepsilon_\perp^{(0)}(\omega)}{1-\delta_\perp(\mathbf{k},\omega)}, \tag{1.69}$$

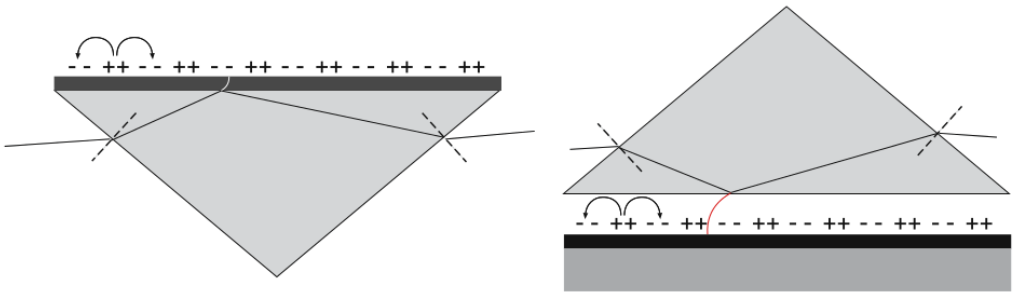

Figure 1.5: Scheme for prism coupling to SPPs via attenuated total internal reflection in Kretschmann (left) and Otto (right) configurations (image taken from [6]).

$$\varepsilon_{\parallel}^{(1)}(\mathbf{k},\omega) = \frac{\varepsilon_{\parallel}^{(0)}(\omega)}{1-\delta_{\parallel}(\mathbf{k},\omega)}, \tag{1.70}$$

with the correction terms given by

$$\delta_{\perp}(\mathbf{k},\omega) = \frac{h_1^2 h_2^2(\varepsilon_1-\varepsilon_2)^2\varepsilon_{\perp}^{(0)2}}{12(h_1+h_2)^2\varepsilon_1^2\varepsilon_2^2}\left(\varepsilon_{\parallel}^{(0)}\frac{\omega^2}{c^2} - \frac{k_z^2(\varepsilon_1+\varepsilon_2)^2}{\varepsilon_{\parallel}^{(0)2}}\right), \tag{1.71}$$

$$\delta_{\parallel}(\mathbf{k},\omega) = \frac{h_1^2 h_2^2(\varepsilon_1-\varepsilon_2)^2}{12(h_1+h_2)^2\varepsilon_{\parallel}^{(0)}}\frac{\omega^2}{c^2}. \tag{1.72}$$

1.6 Excitation of high-k modes

The study of dispersion relations of HMMs showed that they can sustain high-k modes. In order to excite these modes into an HMM, one needs either a near field source, or the implementation of a phase-matching technique to couple light in far field. The phase-matching is required to increase the wavevector component along the interface, as light coming from air at an angle θ has at most a parallel component $k_x = k_0 sin\theta$, with $k_0 = \omega/c$. One can then take in account the same phase-matching techniques which are implemented for the excitation of surface plasmon polaritons.

1.6.1 Prism coupling

A possible phase-matching technique consists in using a prism made of an optically dense material with permittivity ε_2 as the medium from which light impinges on the sample under study, see Fig. 1.5. The HMM would be either deposited directly on one side of the prism (Kretschmann geometry), or separated from it by only a thin air gap (Otto configuration). The light beam enters into the prism on one of the other sides, either perpendicularly or at an angle small enough to be transmitted, and propagates toward the face with the sample. Here, if the radiation impinging with an angle θ is totally reflected, it will enter into the sample with an in-plane wavevector $k_x = k_0\sqrt{\varepsilon_2}sin\theta$. The excitation of a high-k mode is detected with the observation of a minimum in the reflectance spectrum, corresponding to a particular wave mode which coupled to the system.

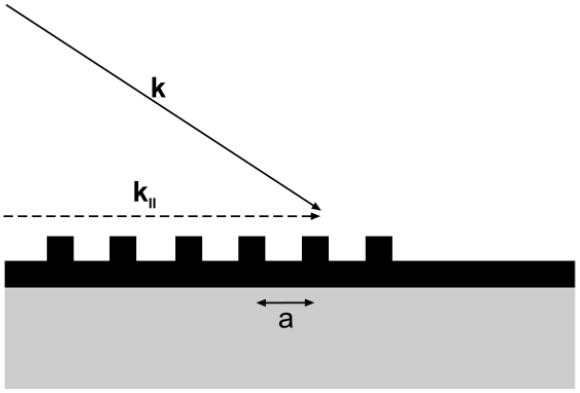

Figure 1.6: Depiction of a one-dimensional grating for phase-matching of light (image taken from [6]).

1.6.2 Grating coupling

Another way to cover the mismatch in the in-plane wavevector consists in patterning the external surface of the sample with a shallow grating of periodic grooves or holes. The ordered periodic structure can be described in terms of an associated lattice and base vectors, to which a reciprocal lattice can be associated. The reciprocal lattice vectors correspond to the contribution of the grating to the in-plane wavevector. The simplest type of grating consists of a one-dimensional array of grooves with constant spacing a, for light polarized along the grooves. This periodical direct lattice corresponds to an analogous one-dimensional lattice in the reciprocal space with spacing $2\pi/a$. Therefore, if one considers light propagating in air with wavevector $k_0 = \omega/c$, and a mode supported by the sample with in-plane wavevector k', the grating matches the two modes if the following condition is satisfied:

$$k' = k_0 sin\theta + \frac{2\pi}{a}m. \tag{1.73}$$

In this equation θ is the angle of incidence of light on the grating, $m \in \mathbb{Z}$ is an integer, and $(2\pi/a)m$ is a wavevector of the grating's reciprocal lattice. As in prism coupling, a succesful phase-matching results into a minimum in the reflectance spectrum. A grating can also cause the reverse process, with an internal mode of the system coupling to light emitted at the grating. If the thickness of the grating is on the order of 10 nm, it doesn't alter significantly the dispersion relation of the sample. Instead, when the thickness is equal to several times the absorption length $L = \alpha^{-1}$ of the chosen material, traditional transmission of light through the grating is interdected.

1.6.3 Nanohole arrays

A nanohole array (NHA) is a metallic thick layer with a periodic arrangement of nanoholes. Due to the periodic array, at given wavelengths the light transmittance through the holes is found to be bigger than what would be classically expected. This phenomeon

is therefore known as extraordinary optical transmission, ot EOT [18].
For an aperture with radius $r \gg \lambda_0$, all light impinging on the hole is able to pass through it in the form of a propagating mode. If a subwavelength hole is considered instead, one observes that propagation of light through the hole is not allowed due to the diffraction limit. In this case, the only way for light to pass through it is by tunneling. In the particular case of electromagnetic radiation impinging perpendicularly on an opaque and infinitely thin screen with a subwavelength circular hole, the trasmission through the hole is given by the analytical expression [19]

$$T_{SH} = \frac{64}{27\pi^2}(kr)^4 \propto \left(\frac{r}{\lambda_0}\right)^4. \tag{1.74}$$

In addition to the dependence on the hole radius, simulations show that, in the case of a realistic metallic layer with finite thickness, the transmittance decreases exponentially with the thickness. Nonetheless, the transmission can be enhanced if many subwavelength holes are fabricated in a periodic pattern on the metallic film.
Solving Maxwell's equations at the interface between a metal and a dielectric, one finds that particular solutions exist in the form of surface waves propagating along the metal-dielectric interface. These oscillations of both charges in the metal and electromagnetic fields in the dielectric are called surface plasmon polaritons, or SPPs. The dispersion relation for SPPs traveling with momentum k' and frequency ω at a flat infinite metal-dielectric interface is found to be [6]

$$k' = k_0\sqrt{\frac{\varepsilon_m\varepsilon_d}{\varepsilon_m + \varepsilon_d}}. \tag{1.75}$$

where ε_m and ε_d are the permittivities of the metal and the dielectric at the interface. In the case of a NHA, the periodic arrangement of nanoholes acts as a grating which helps coupling external light to SPPs traveling along the NHA surface. Furthermore, SPPs are able to tunnel through the holes more efficiently than radiating light, passing from one interface to the other. Here, the same nanohole lattice causes the decoupling of SPPs in radiating light, causing an increment of the layer trasmittance.
At a fixed angle of incidence, and depending on the characteristics of the chosen grating, SPPs resonance are excited at resonance wavelengths at which the phase-matching condition is satisfied. In the case of a two-dimensional grating, the phase matching condition (1.73) must be modified to

$$\mathbf{k}' = \mathbf{k}_{\parallel} + n\mathbf{G}_1 + m\mathbf{G}_2, \tag{1.76}$$

where G_1, G_2 are the basis wavevectors of the two-dimensional reciprocal lattice, and n, m are the Miller integer indexes defining the scattering order. When Eq. (1.76) holds, SPPs are excited, causing a maximum peak in the trasmittance spectrum. In the case of an hexagonal array of nanoholes and for normally incident radiation, the phase-matching holds at wavelengths given by [20]

$$\lambda_{SPP}(n,m) = \frac{a}{\sqrt{\frac{4}{3}(n^2 + nm + m^2)}}\sqrt{\frac{\varepsilon_m\varepsilon_d}{\varepsilon_m + \varepsilon_d}}. \tag{1.77}$$

Equations (1.75) and (1.77) were obtained considering an infinite flat metal-dielectric interface. The presence of nanoholes on the surface modifies these relations, shifting the resonance wavelengths at which transmittance maxima are found.
To give a definition of EOT, one defines a normalized transmission coefficient T_{norm} as the ratio of the transmittance T_{NHA} through the nanohole array to the sum of the ordinary transmission T_{SH} of each nanohole:

$$T_{norm} = \frac{T_{NHA}}{\sum_j T_{SH}} \tag{1.78}$$

At wavelengths of surface plasmon resonance, values of T_{norm} bigger than unity are observed. In other words, one observes a transmitted intensity through the periodic arrangement of nanoholes whose magnitude is bigger than the sum of the intensitis which would be transmitted by each nanohole singularly. This happens because, in addition to light tunneling through the holes, even light impinging on opaque regions can be channeled and transmitted by means of SPPs. Therefore, a NHA behaves as a frequency-selective grating. Additionally, localized surface plasmons are observed on the border of each hole, as a consequence of light penetrating inside the metal. The enhancement of the electric field at the borders also affects the transmittance spectrum, although to a lesser effect than EOT. These properties make the NHA an interesting tool in the field of biosensing, as the dependence of the resonance wavelength on the permittivity of the external dielectric allows to measure small variations of its refractive index.

1.7 Fluorescence near interfaces

In photoluminescence (PL) a molecule, atom, or ion, reaches an excited state, having absorded energy from an impinging electromagnetic radiation. The excited system will thus decay to a lower-energy state with a simultaneous emission of energy, either in the form of photons or by means of non-radiative mechanisms. The emission of excitation energy in the form of a photon is a process called fluorescence, which is a typical spontaneous emission process. The spontaneous transition decay rate between an excited state (i) and a lower energy state (j) is given by the Fermi's golden rule [21]

$$\Gamma_{i,j} = \frac{2\pi}{\hbar}|M_{i,j}|^2\rho_{i,j}, \tag{1.79}$$

where $M_{i,j}$ is the transition matrix element connecting the final and the initial energy levels, and $\rho_{i,j}$ is the photonic density of states (PDOS), or optical field density of states. The reciprocal of the decay rate, $\tau_{i,j} = \Gamma_{i,j}^{-1}$, is the characteristic lifetime of the spontaneous emission process. From (1.79), it follows that the probability of spontaneous emission can be modified by altering the PDOS. The dependance of the spontaneous emission rate of a fluorescent molecule on the environment was first pointed out by Purcell [22], for emitters in a resonant cavity (Purcell effect). The PDOS of given emitters can also be modified by placing them in close proximity to an interface with another medium. In fact, the field reflected at the interface can interfere with the emitter. Depending on

whether the reflected field and the emitter are in phase or out of phase, the PDOS at the emitter is correspondingly enhanced or reduced. In addition, the interface and the medium underneath can be able to sustain new electromagnetic modes, increasing the total PDOS for the excited emitters. This process can be described equivalently with a classical or a quantum-mechanical model, as established by Yeung and Gustafson [23].
A comprehensive analytical solution to this problem, formulated in the classical viewpoint, was first given by Chance, Prock and Silbey in 1975 [24]. In this model, the fluorescent molecule is modeled as a forced damped dipole oscillator, placed at a given distance from the interface. The total electromagnetic field at the dipole must be evaluated, considering both the emitted field and the back-reflected field from the surface. Additionally, the emitter can lose energy via energy transfer to the interface (e.g. coupling with SPPs and lossy surface waves). The equation of motion for the emitter is then

$$\frac{d^2\mu}{dt^2} + \omega^2\mu = \frac{e}{m}E_R - \Gamma_0\frac{d\mu}{dt}, \tag{1.80}$$

where μ is the dipole momentum, ω is the oscillation frequency in absence of damping, m is the effective mass of the dipole, e is the electric charge, E_R is the reflected field evaluated at the dipole position (i.e. the driving term), and Γ_0 is the decay rate (i.e. the damping costant) of the emitter in absence of the interface. The dipole moment and the reflected field change in time with the same dependancy,

$$\mu = \mu_0 e^{-i(\omega+\Delta\omega)}e^{-\Gamma t/2}, \tag{1.81}$$

$$E_R = E_0 e^{-i(\omega+\Delta\omega)}e^{-\Gamma t/2}, \tag{1.82}$$

where $\Delta\omega$ and Γ are the frequency shift and the decay rate in the presence of the interface, respectively. Substituting (1.81) and (1.82) in (1.80), one obtains the following expressions for these quantities,

$$\Delta\omega = \frac{\Gamma^2}{8\omega} + \left[\frac{e^2}{2\mu_0 m\omega}\right] Re(E_0), \tag{1.83}$$

$$\Gamma = \Gamma_0 + \left[\frac{e^2}{2\mu_0 m\omega}\right] Im(E_0). \tag{1.84}$$

Evaluating (1.83) and (1.84), it follows that the decay rate depends strongly on the out-of-phase component of the reflected field. To evaluate the reflected field at the dipole position, either the Hertz vector potential of the Green's dyadic function method can be employed. The emitter is modeled as a randomly oriented dipole, whose decay rate can be computed as a combination of the decay rates of perpendicular and parallel dipoles with respect to the interface,

$$\Gamma_t = \Gamma_0\left[1 - \frac{3}{2}Im\left(\int_0^\infty R_p\frac{u^3}{a_1}exp(-4\pi n_1 a_1 z/\lambda)du\right)\right], \tag{1.85}$$

$$\Gamma_p = \Gamma_0\left[1 + \frac{3}{4}Im\left(\int_0^\infty [(1-u^2)R_p + R_t]\frac{u}{a_1}exp(-4\pi n_1 a_1 z/\lambda)du\right)\right], \tag{1.86}$$

where the integration variable $u = k_x/k_1$ is the wave-vector component of the dipole field in the interface plane, normalized with respect to the far-field wavevector k_1 of the dipole radiation in the medium embedding the emitter, n_1 is its refractive index, z is the distance between the emitter and the interface, and λ is the emission wavelength. The parameter $a_1 = -i\sqrt{1-u^2}$ is related to the perpendicular component of the wave-vector at the interface, while R_p and R_t are the Fresnel coefficients for p- and s- polarized light at the interface, which are functions of the integration variable u. They can be expressed as

$$R_t = \frac{a_1 - a_2}{a_1 + a_2}, \quad R_p = \frac{\varepsilon_1 a_2 - \varepsilon_2 a_1}{\varepsilon_1 a_2 + \varepsilon_2 a_1}, \tag{1.87}$$

where ε_1 is the dielectric function of the medium embedding the emitter, ε_2 is the dielectric function of the medium beyond the interface, and $a_2 = -i\sqrt{\varepsilon_2/\varepsilon_1 - u^2}$.
Since the integration variable ranges from 0 to ∞, the reflection coefficients have to be calculated for both real and complex angles of incidence. These evaluations correspond to incident waves which are propagating and evanescent in the other medium, respectively.
For an ensemble of dipoles with isotropic or random orientation with respect to the interface, the total decay rate is obtained as the spatial average

$$\Gamma_{iso} = \frac{1}{\tau} = \frac{2}{3}\Gamma_p + \frac{1}{3}\Gamma_t. \tag{1.88}$$

1.8 Nonlinear optics

Properly engineered HMMs can exhibit interesting nonlinear optical properties [2, 4]. Nonlinear optics (NLO) is a branch of optics which studies the nonlinear response of materials to high intensity electromagnetic radiation. As it was pointed out in Eq. (1.7), low intensity electric fields induce into a medium a polarization $\mathbf{P} = \varepsilon_0 \chi \mathbf{E}$ which grows linearly with the electric field. This relationship can be regarded as the low-intensity approximation of a more general power series of the electric field, namely [25]

$$\mathbf{P}(t) = \varepsilon_0 \left(\chi^{(1)}\mathbf{E}(t) + \chi^{(2)}\mathbf{E}^2(t) + \chi^{(3)}\mathbf{E}^3(t) + ... \right). \tag{1.89}$$

In Eq. (1.89) the term $\chi^{(n)}$ is the n-order nonlinear susceptibility, and in the general case it is a (n+1)-rank tensor with $3^{(n+1)}$ components. In explicit form, the i-th component of the polarization density $\mathbf{P}$ is

$$P_i(t) = \varepsilon_0 \left(\sum_{j=1}^{3} \chi_{ij}^{(1)} E_j(t) + \sum_{j=1}^{3}\sum_{k=1}^{3} \chi_{ijk}^{(2)} E_j(t)E_k(t) + \sum_{j=1}^{3}\sum_{k=1}^{3}\sum_{l=1}^{3} \chi_{ijkl}^{(3)} E_j(t)E_k(t)E_l(t) + ... \right) \tag{1.90}$$

Usually nonlinear terms are significant only for values of the electric field high enough to be comparable with the interatomic electric fields, that is, $E \sim 10^7 \div 10^8\ V/m$. In the case of media with inversion symmetry, called centrosymmetric media, one can prove that susceptibilities of even order must be equal to zero . Therefore in centrosymmetric media

(e.g., glass) the first non-null nonlinear polarization term is the one which depends on the third power of the electric field:

$$\mathbf{P}^{(3)}(t) = \varepsilon_0 \chi^{(3)} \mathbf{E}^3(t). \tag{1.91}$$

Because of its power dependence on the electric field, the nonlinear polarization will have frequency components separate from those of the electric field. This property leads to the emission of sum-frequency-generated radiation. Considering the frequencies ω_m, ω_n, and ω_o, one can examine the i-th component of the nonlinear polarization characterized by a frequency equal to the sum of these frequencies:

$$P_i^{(3)}(t;\omega_m+\omega_n+\omega_o) = \varepsilon_0 \sum_{jkl} \sum_{(mno)} \chi_{ijkl}^{(3)}(t;\omega_m+\omega_n+\omega_o,\omega_m,\omega_n,\omega_o) E_j(t;\omega_m) E_k(t;\omega_n) E_l(t;\omega_o). \tag{1.92}$$

In this expression, the electric fields are assumed to be linearly polarized. The sum over (mno) indicates that the sum over the three frequencies is fixed. One can greatly simplify Eq. (1.92) by limiting the analysis to a monochromatic electric field, linearly polarized along the x-direction, oscillating with angular frequency ω. In this case the incident field can be written as

$$E_x(t) = E_x(\omega) e^{i\omega t} + (E_x(\omega))^* e^{-i\omega t} = E_x(\omega) e^{i\omega t} + E_x(-\omega) e^{-i\omega t}, \tag{1.93}$$

and the polarization $\mathbf{P}^{(3)}$ will be orientated along the x-direction as well,

$$P_x^{(3)}(t;\omega_m+\omega_n+\omega_o) = \sum_{(mno)} \chi_{xxxx}^{(3)}(t;\omega_m+\omega_n+\omega_o,\omega_m,\omega_n,\omega_o) E_x(t;\omega_m) E_x(t;\omega_n) E_x(t;\omega_o). \tag{1.94}$$

The x subscript will now be omitted. The choice of a monochromatic electric field forces the three frequencies to be equal to either ω or $-\omega$. Therefore, one can obtain two different terms for the third order nonlinear density polarization:

$$P^{(3)}(t;3\omega) = \varepsilon_0 \chi^{(3)}(t;3\omega) E^3(t;\omega) + c.c. \tag{1.95}$$

$$P^{(3)}(t;\omega) = 3\varepsilon_0 \chi^{(3)}(t;\omega) |E(t;\omega)|^2 E(t;\omega) + c.c. \tag{1.96}$$

Hence, the result is that an incident electric field at frequency ω induces the medium to irradiate a field at 3ω and a field at ω. The first term relates to the phenomenon of Third Harmonic Generation (THG), while the second term gives rise to the optical Kerr effect. One can show that the second term causes the optical constants of the nonlinear medium to depend on the intensity of the external field, according to the equations

$$n(I) = n_0 + n_2 I, \tag{1.97}$$

$$\alpha(I) = \alpha_0 + \beta I. \tag{1.98}$$

In these expressions the quantities n_0 and α_0 are the linear refractive index and the linear absorption coefficient, respectively; on the other hand, n_2 and β are respectively the

nonlinear refractive index and the nonlinear absorption coeficient of the material. The coefficients n_2 and β give rise to a linear dependance of the optical constants on the intensity of the external electric field, caused by the third order nonlinear susceptibility. In order to prove it, the third order nonlinear term with frequency ω can be grouped with the first order linear term, which has the same frequency (the frequencies will now be omitted to lighten the notation):

$$\begin{aligned} P &= \varepsilon_0\chi^{(1)}E + 3\varepsilon_0\chi^{(3)}|E|^2E + c.c. \\ &= \varepsilon_0(\chi^{(1)} + 3\chi^{(3)}|E|^2)E + c.c. \\ &= \varepsilon_0\chi_e E + c.c. \end{aligned} \tag{1.99}$$

where the following definition was given ('e' stands for effective):

$$\chi_e = \chi^{(1)} + 3\chi^{(3)}|E|^2. \tag{1.100}$$

Recalling that the complex refractive index $\widetilde{n} = \varepsilon_e = n + i\kappa$ is related to the electric susceptibility by $\widetilde{n}^2 = 1 + \chi_e$, and substituting the attenuation coefficient κ with the absorption coefficient $\alpha = 4\pi\kappa/\lambda$, one can write ($k = 2\pi/\lambda$)):

$$(n_0 + n_2 I)^2 - \frac{(\alpha_0 + \beta I)^2}{4k^2} + i\frac{(n_0 + n_2 I)(\alpha_0 + \beta I)}{k} = 1 + Re\,(\chi_e) + iIm\,(\chi_e)\,. \tag{1.101}$$

If one neglects terms with powers of two or more in n_2 or β, the following expressions can be calculated for the components of the effective susceptibility ($I = (n_0\varepsilon_0 c/2)|E|^2$):

$$Re\left(\chi^{(3)}\right) = \frac{2n_0\varepsilon c}{3}\left(2n_0 n_2 - \frac{\alpha_0\beta}{2k^2}\right), \tag{1.102}$$

$$Im\left(\chi^{(3)}\right) = \frac{2n_0\varepsilon c}{3}\left(\frac{n_0\beta}{k} - \frac{\alpha_0 n_2}{k}\right). \tag{1.103}$$

These equations show that the nonlinear terms n_2 and β affect both the real and imaginary components of the third order nonlinear susceptibility. If the analysis is limited to media where the linear attenuation coefficient is small with respect to the linear refractive index ($\kappa_0 \ll n_0$), one finds that the nonlinear refractive index is proportional only to the real component of $\chi^{(3)}$, while the nonlinear absorption coefficient is proportional only to the imaginary component:

$$Re\left(\chi^{(3)}\right) = \frac{4}{3}n_0^2\varepsilon_0 c n_2, \tag{1.104}$$

$$Im\left(\chi^{(3)}\right) = \frac{2n_0^2\varepsilon}{3k}\beta. \tag{1.105}$$

There can be several mechanisms which cause nonlinear effects in media. Nonlinearity can arise from thermal effects at high temperatures, or because of the realignment of anisotropic molecules in the medium, affected by the external electric field. Another nonlinear contribution comes from the nonlinear response of bound electrons to an applied optical field [25]. These different phenomena are characterized by different time scales and different magnitudes in their contribution to nonlinear optical constants. For example,

thermal effects happen on a time scale of the order of a few ns, and give rise to a term $\chi^{(3)} \sim 10^{-12}\ m^2/V^2$. On the other hand, electronic contributions happen on a much faster scale, but with a lower effect. The response time of bound electrons can be estimated semi-classically, computing the time required by an electron to orbit around a nucleus. In the framework of Bohr's model, one finds

$$\tau = 2\pi \frac{a_0}{v}, \tag{1.106}$$

where $a_0 \approx 0.5 \cdot 10^{-10}\ m$ is the Bohr radius, and $v \approx c/137$ is a typical value for electron velocity. Hence, a time response of $\tau \approx 10^{-16}\ s$ is obtained, whereas contributions to the nonlinear susceptibility are on the order of $\chi^{(3)} \sim 10^{-22}\ m^2/V^2$. Even if fundamentally smaller, this effect is of great importance because in principle it can be observed in all dielectric materials. To observe the nonlinearity caused by the polarization of bound electrons, one can take advantage of the different time scales. A laser emitting pulses lasting only a few picoseconds or less allows to excite the nonlinear response of bound electrons, without inducing thermal effects.

Chapter 2

Experimental techniques

In this chapter the experimental techniques for the fabrication and characterization of one-dimensional hyperbolic metamaterials are presented. Firstly, the magnetron sputtering technique is described, which was used to realize periodic multilayers based on thin films of gold and alumina with nanometer controlled thicknesses. Then the tools for nano-characterization are presented, namely the Atomic Force Microscopy, the Scanning Electron Microscopy, and the X-Ray Reflectivity. These techniques were used to study the structural features of the multilayers, such as the thin film thicknesses, and the quality of the interfaces. Eventually, a description is given of the Variable Angle Spectroscopic Ellipsometry and the z-scan technique, which are optical characterization methods. With these techniques it was possible to measure the optical constants of the samples and their nonlinear optical properties.

2.1 Magnetron Sputtering

Sputtering is a physical vapor deposition technique, which enables to create thin films of a certain material with low roughness and nanometric controlled thickness. In a sputtering process a solid target is bombarded with energetic particles, typically a plasma, in order to cause the ejection of atoms or molecules. As these molecules are continuously emitted into an isolate chamber, they tend to condense onto a sample positioned nearby. A thin film of the target material is thus gradually formed on the sample.

The sputtering process happens inside a vacuum chamber, in which the solid target and the sample are mounted onto a target holder and a sample holder, respectively, as depicted in Fig. 2.1. A series of pumps (typically a rotary vane pump and a turbomolecular pump) are used to achieve a high vacuum of $P \sim 10^{-6}\ mbar$ inside the chamber. Such a high vacuum is important to clean the chamber from other substances, which would worsen the quality of the sputtering process, creating inclusions and defects in the sputtered films. After the initial high vacuum is reached, Argon gas is pumped into the chamber reaching a pressure of $P \sim 10^{-3}\ mbar$. The Argon gas is the medium from which the plasma of ions and electrons is obtained. The target is held still with a conductive clamping ring,

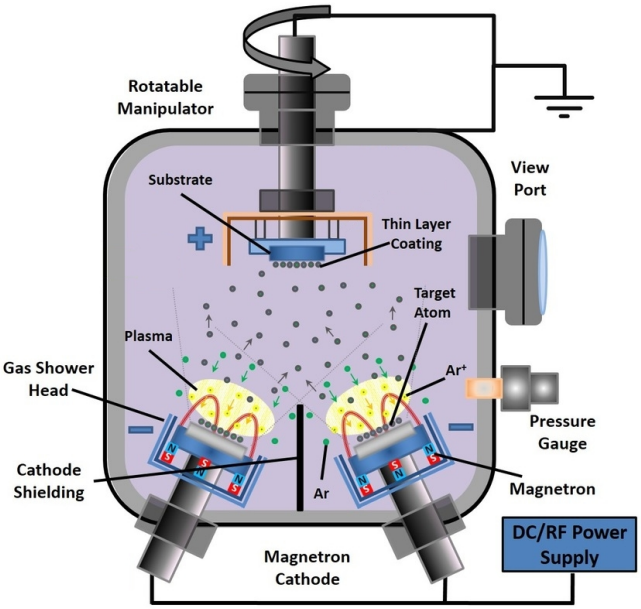

Figure 2.1: Schematic setup of a magnetron sputtering apparatus with two independent targets.

and a ground shield is put around it at close distance. The clamping ring is biased at a negative high voltage with respect to the ground shield, which is shortcircuited to the walls of the chamber. The high voltage between the two elements causes the plasma ignition, producing Ar^+ ions and electrons. As Ar^+ ions are produced, they are accelerated by the DC voltage towards the target and collide with it, causing the ejection of molecules of the target material. These molecules are mostly neutral, so they can travel across the chamber unaffected by the electric voltage. Some of these molecules condense onto the sample, forming a bound layer. In this process Argon is chosen because it is inert, so it doesn't react neither with the target nor the sample. Depending on the particular application, one can conduct a sputtering process with a different gas.

In a magnetron sputtering system, permanent magnets are used to create a strong magnetic field near the target area. The magnets are placed with their south pole at the center of the target sample, and their north pole at its border. The magnetic field confines the plasma close to the target area, while at the same time increasing its density. Since the plasma is kept ignited only close to the target and far from the sample, it won't affect the thin film which is gradually being formed onto the sample. Additionally, the magnetic field causes the electron to spiralize, thus following longer trajectories. This effect increments the collision rate with Argon atoms, leading to a stable plasma with higher density of ions, and to a higher ejection rate. The sputtering process can then be completed in a shorter time, minimizing the number of impurities.

Depending on the material being sputtered, different power supplies are employed. In insulating and semiconducting targets, Ar^+ ions colliding on the target cause the build up of a localized charge. It is therefore necessary to use a radio frequency (RF) source to

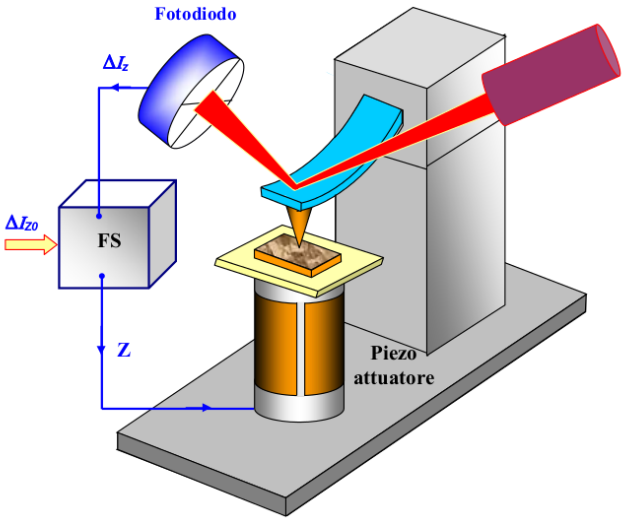

Figure 2.2: Schematic setup of an atomic force microscope. The differential values of intensities between the photo-diodes are used as input in a feedback circuit to control the piezoelectric actuator in the z-direction.

alternatively hit the target with positive ions and electrons and disperse the accumulated charge. For conductive targets instead, a simple DC power supply can be used.
The magnetron sputtering apparatus used during this thesis work has three target holders, each one having an independent power supply and a shutter. With this setup, it's possible to alternate the sputtered materials in the same deposition and create multilayers of different materials. The sample holder is put at the same distance from all the three target holders, at the summit of a pyramidal shape. The target holders are tilted towards the sample holder, which is kept in rotation for the whole deposition process. This helps the synthesis of homogeneous layers on the sample.
The properties of the thin films (thickness, density, impurities) obtained by magnetron sputtering depend on several system parameters. Among the most important factors there are the distance between target and sample, the voltage between target holder and ground, the pressure at which the Argon gas is kept, the choice of the target material, and the temperature of the targets and the sample. In particular, since the process happens in a vacuum chamber, a water cooling system is required to cool the targets and the sample.

2.2 Atomic Force Microscopy

Atomic Force Microscopy (AFM) is a characterization technique which follows the principle of Scanning Probe Microscopy, as it collects information on the sample by scanning it with a physical probe. In an atomic force microscope the probe consists of an elastic cantilever - a lever with a fixed end - with a sharp tip at its free end. When the tip is brought close to the surface of the sample, several types of interaction between the tip and the sample arise and cause the cantilever to bend. A measurement of the degree of bending and torsion of the probe enables to reconstruct the morphology of the sample in that point.

A scan of the sample on different points enables to construct a three-dimensional image of the surface with high resolution. The first atomic force microscope was invented in 1986 by Gerd Binnig, Calvin Quate, and Christoph Gerber, at IBM [26]. Today AFMs are widely used not only for imaging activities, but also for manipulating matter at the atomic scale.

Several modes of operation of an AFM exist, depending on how the probe interacts with the sample. In this thesis work an AFM in non-contact mode was employed. In this configuration the tip of the cantilever doesn't touch directly the sample. Instead, it is kept at distances on the order of $\lesssim 10\ nm$, at which the sample and the probe interact by means of van der Waals forces. The AFM used in the present work is a NT-MDT Solver Pro.

The cantilever and its tip are made mainly of silicon, with an Au surface layer to increase its reflectivity. The tip, which protrudes transversally from the cantilever, has a total height of $\sim 10\ \mu m$ and a radius of curvature of only $10\ nm$. A piezoelectric actuator causes the cantilever to vibrate at its own resonance frequency $\omega_0 \sim 100\ kHz$, with an oscillation amplitude $A_0 \sim 10 \div 100\ nm$. The sample is mounted on a sample holder, which can be translated by three independent piezoelectric actuators. One actuator causes the sample to move closer or further away from the probe along the z direction. The other two actuators move the sample in the x-y plane, enabling the scan of an area on the order of $100\ \mu m \times 100\ \mu m$. Starting with the probe and the sample far from each other, the sample is gradually brought closer to the probe until van Der Waals forces arise between them. This interaction modifies both the shape of the resonance curve and its resonant frequency. As the cantilever is still forced to oscillate at the frequency ω_0, which differs from its new resonance frequency, the amplitude of its oscillations will decrease to a value $A(x, y, z) < A_0$. In order to maximize the measurement sensibility, at every scanning point the distance between probe and sample is regulated by a feedback mechanism to keep the amplitude oscillation at $A' = A_0/2$. At each scanning point, the position of the piezoelectric actuator in the z-direction is stored in memory, so that during the scan a map of z-values is created. It is worth specifying that the obtained values are not absolute measurements. Instead, they are relative to the z-position reached by the the piezoelectric actuator when the probe first approaches the sample.

The interaction with the sample causes the cantilever to bend inwards and twist laterally, according to the local morphology of the sample. To measure the degree of bending of the cantilever, the "beam-bounce" method is used. The laser beam emitted by a diode laser is focused onto the cantilever and is reflected into a detector composed of a matrix of 4 photo-diodes, see Fig. 2.2. Before the measure starts, the system is aligned in such a way that the reflected beam impinges at the center of the detector, and the 4 photo-diodes measure equal light intensities. When the cantilever is bent by the interaction with the sample, the beam is reflected on a different region of the detector, so that the photo-diodes will detect different intensities. The differential values of intensities between the photo-diodes allow to measure the bending of the probe, and are used as input values in the feedback circuit which controls the main actuator. With these data, a 3-D image of the surface on the sample can be reconstructed, with resolution of $\lesssim 1\ nm$ in the z direction. Due to

the convolution of the tip with the features of the sample, lateral resolution is lower, on the order of 10 nm. Collected data can contain spurious features due to the sloping of the sample, or to the cantilever skipping lines during the scan. These defects were corrected and the data were analyzed with the software Gwyddion [27].
In this work, the use of an AFM enabled to measure the thicknesses of single layers deposited on a substrate and the rougnesses of their surfaces. The thickness measurements were necessary to calibrate the sputtering rate of the sputtering system, and create layers with controlled thickness. To obtain a thin film height, the distance between the exposed substrate and the external surface of the thin film has to be measured. The substrate was exposed either by scratching the surface with a metallic blade, or by applying a marker line on the substrate before the sputtering process and removing it afterwards with a solvent. In this way a step-like structure is obtained between the layer and the substrate. In the case of multilayer samples, the total thickness of the samples were measured. These values were compared with the nominal total thicknesses, obtaining coherent values within experimental error.
In addition, an AFM enables to measure the roughness of planar interfaces, which has to be as small as possible to create ordered structures. The roughness of a surface can be described in terms of the average roughness R_a. To define this parameter, a scanning line is considered along the surface under exam. Along this line, the z-height is measured on n ordered, equally spaced points, and from these measurements a mean height is calculated. Indicating with y_i the vertical distance from the mean height at the i-th point, the average roughness is defined as the arithmetical mean deviation

$$R_a = \frac{1}{n}\sum_{i=1}^{n}|y_i|. \tag{2.1}$$

2.3 Scanning Electron Microscopy

In Scanning Electron Microscopy, a focused beam of high energy ($E \sim 1 \div 30\ keV$) electrons is employed as a probe to scan the sample. As the beam hits the sample, it causes the emissions of different particles, namely electrons and X-rays, depending on the morphology and the composition of the sample.
A scanning electron microscope (SEM) consists of several components positioned sequentially in the so-called electronic column, see Fig. 2.3. The beam of electrons is emitted by a tungsten filament either by thermoionic effect or field emission. In the latter case, the tungsten filament has a sharp point and a high negative voltage is applied to it. The electric field close to the point is high enough ($E > 10^7\ V/cm$) that electrons can pass through the potential barrier by tunnel effect. In this way, current densities up to $10^6\ A/cm^2$ are obtained, with a narrower energy distribution than with simple thermoionic effect. The electrons are accelerated at energies of $0.5 \div 30\ keV$ before they leave the electron gun. The electron beam is then focused by the first electromagnetic lens, which is coupled to an aperture. Changing the acceleration voltage and the parameters of the electromagnetic

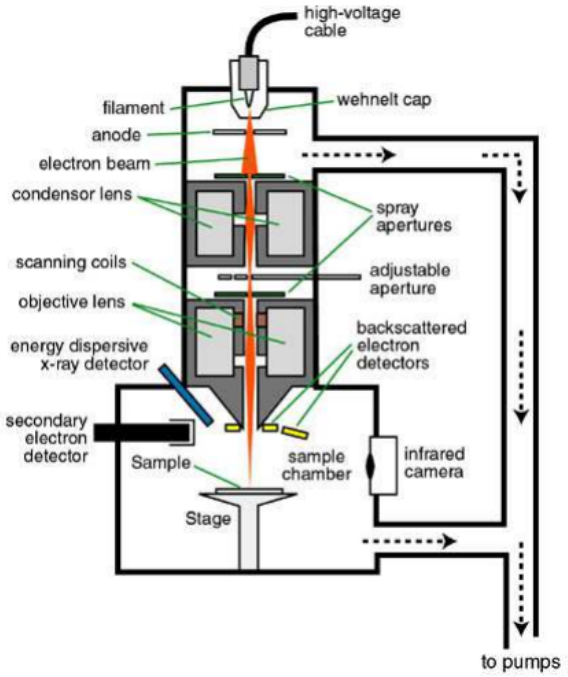

Figure 2.3: Sketch of a Scanning Electron Microscopy.

lens, one can modify the intensity of the electron beam which will pass through the aperture. Other EM lenses enable to focus the beam up to a diameter of only $4 \div 5\ nm$. It's worth noting that a beam with a smaller diameter will improve the resolution and the depth of field, but it will also decrease the brightness of the final image. Eventually, a system of scan coils allows to deviate the beam along the x- and y-direction, to scan a wide area of the sample.

High vacuum is necessary to obtain a focused electron beam, and to analyze the particles emitted by the sample. Traces of gas would scatter the electrons, reducing the intensity of the initial beam and lowering the signal-to-noise ratio. A series of pumps are used to reduce the pressure down to $P \sim 10^{-6}\ mbar$. Even at this pressure, the beam current drops from $I \sim 10\mu A$ when is emitted from the filament, down to $\sim 100\ pA$ before it hits the sample.

As the electron beam interacts with the sample, it causes the emission of secondary electrons (SEs), backscattered electrons (BSEs), and X-rays, through distinct processes. These particles can be collected to obtain different informations about the sample under exam.

SEs are low energy electrons, emitted because of anelastic scattering between the beam electrons and the external electrons of the atoms in the sample. The SEs which are observed outside the sample are actually emitted from atoms which reside a few nanometers below the surface. For this reason, they carry information about the surface morphology of the sample. The SEs which are emitted at an angle with respect to the impinging beam are gathered by a high voltage grid, which accelerates them to a scintillator-coupled photomultiplier. Instead, the SEs which are emitted in a direction parallel to the impinging

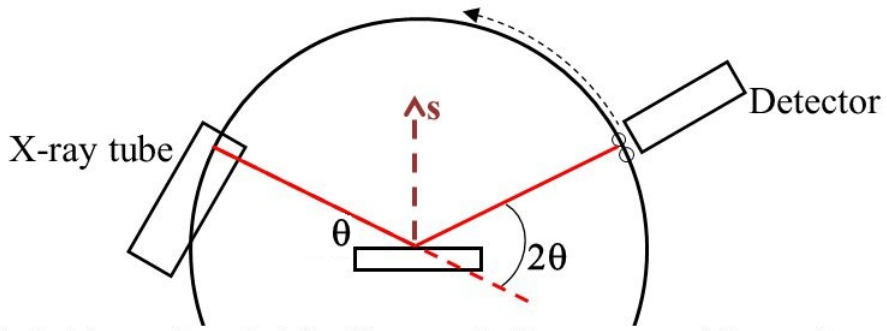

Figure 2.4: Scheme of X-Ray Reflectivity measurements in the θ-2θ configuration. X-ray are emitted by the X-ray tube and incide at a grazing angle θ on the sample. The specularly reflected beam is observed on the detector at an angle 2θ with respect to the incident beam propagation direction.

beam are observed with an In-lens detector.
BSEs are high energy electrons from the impinging beam which are back-scattered outside the sample. This happens because of elastic collisions with inner shell electrons or nuclei in the sample. The cross section for the elastic scattering grows like the square of the atomic number of the material, hence the number of emitted BSEs will depend on the local composition of the sample.
The interaction of the beam with the sample causes also the emission of X-rays. In this case, not only the intensity but also the characteristic discrete spectrum gives information on the sample composition. X-rays are measured with a solid-state detector.
The SEM used in the present work is a Zeiss Sigma HD field-emission microscope (FESEM).

2.4 X-Ray Reflectivity

X-Ray Reflectivity (XRR) consists in directing an X-ray beam on the flat surface of a thin film or multilayer sample at small angles of incidence with respect to the surface($< 10°$), and in measuring the intensity of the beam reflected at a specular angle. The study of the distribution of intensity at different incidence angles allows to obtain the density profile of the sample. This in turn permits to determine the quality of the interfaces, the densities of the constituents, and the thicknesses of thin films [28]. In the present work a PANalytical X'Pert-Pro HR diffractometer was used.
Measurements of XRR can be operated with an X-ray diffractometer (XRD). Typically, while in X-ray diffraction at grazing incidence (GI-XRD) X-rays are scattered at large angles, in XRR experiments the X-rays impinging at small incident angles are reflected specularly. In an XRD, the X-ray beam is produced in an X-ray tube, where a high energy electron beam hits a copper filament. This causes the emission of the characteristic $Cu\ K\alpha$ peak at $\lambda = 1.54\ \mathring{A}$, which corresponds to photons with energy $E \sim 8\ keV$. The emitted beam passes through a series of collimators, monochromators, and attenuators, depending on the type of beam required for the particular experiment. The sample is mounted on a

goniometric sample holder, which can be both translated and rotated with respect to three orthogonal directions, with angular resolution of $\sim 10^{-5}$ degrees. The detector is typically a scintillation counter. For reflectivity measurements the diffractometer is operated in the $\theta - 2\theta$ configuration, in which the source is held still, while the sample holder and the detector rotates in the plane of incidence. The beam emitted by the X-ray tube impinges at a grazing angle θ on the sample, whereas the specularly reflected beam is collected by the detector at an angle 2θ with respect to the incident beam propagation direction.
The electromagnetic response of a material to X-rays of a given frequency is described in terms of a complex refractive index. The physical interpretation of this refractive index is the same as at optical wavelenghts, but its values are significantly different. It is usually expressed as

$$n = 1 - \delta + i\beta, \tag{2.2}$$

where the quantities δ and β are both very small, being on the order of 10^{-6}. This is related to the weak interactions of X-rays with matter. The two real and imaginary components of the refractive index depend on the atomic composition of the sample, through the equations

$$\delta = \frac{2\pi\rho r_0}{k^2}, \tag{2.3}$$

$$\beta = \frac{\mu}{2k}, \tag{2.4}$$

where ρ is the electronic density in the medium, $r_0 = 2.82 \cdot 10^{-5}\mathring{A}$ is the electron radius, $k = 2\pi/\lambda$ is the X-ray photon wavenumber, and μ is the absorption coefficient of the material. Since the refractive index for X-rays has a real part which is extremely close to 1, but smaller than it, the critical angle α_c for total internal reflection of X-rays coming from air is equal to a few *mrad*. In terms of grazing angles, the Snell's law for refraction of light impinging at an interface from air is $cos(\alpha_i) = ncos(\alpha_t)$. Truncating the Taylor series expansion of the cosine functions for small angles, one finds that the critical angle is given by

$$\alpha_c = \sqrt{2\delta} = \frac{\sqrt{4\pi\rho r_0}}{k}. \tag{2.5}$$

Therefore, a measurement of the critical angle represents an indirect measurement of the electronic density of the surface layer. At angles greater than α_c, for thin film or multilayer samples, the reflectivity varies with the incident angle due to interference between X-rays being reflected and transmitted at the interface. If the sample consists of a single layer of thickness t, deposited on a ideally semi-infinite substrate, the reflectivity for X-rays results to be

$$R = \left| \frac{r_1 + r_2 e^{-2ik_{0z}t}}{1 + r_1 r_2 e^{-2ik_{0z}t}} \right|^2, \tag{2.6}$$

where $r_{1,2}$ are the Fresnel reflectivity coefficients of the air-sample surface and of the sample-substrate surface, respectively, and k_{0z} is the wavevector component in the vertical direction of the beam transmitted through the layer. Peaks of maximum intensity are

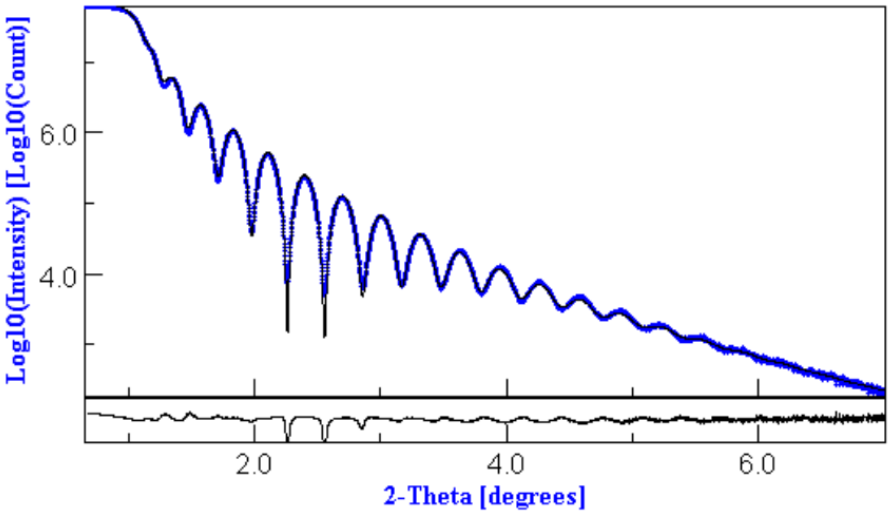

Figure 2.5: Reflectivity spectrum measured on a gold thin film deposited on crown glass. Data are plotted as a function of 2θ, which is twice the grazing incidence angle. The critical angle results to be equal to $\theta = 0.545°$. A slow-frequency variation of intensity can be observed due to the finite thickness of the substrate.

observed whenever the condition $exp(-2ik_{0z}t) = 1$ holds, which happens at angles α_{im} satisfying

$$2t\sqrt{sin^2\alpha_{im} - sin^2\alpha_c} = m\lambda. \tag{2.7}$$

The previous expression can be approximated as $\alpha_{im}^2 - \alpha_c^2 = m^2(\lambda/2t)^2$ for small angles. Therefore, the measurement of the angular positions of different orders of intensity maxima (called Kiessig fringes) allows to evaluate the layer thickness t. Only a finite number of Kiessig fringes can be experimentally observed, as the reflectivity for bigger angles. Defining the momentum transfer as $Q = \frac{4\pi}{\lambda} sin\alpha$, one finds that the reflectivity decreases as $R \propto Q^{-4}$. The intensities measured in reflection span several orders of magnitude, and long times of integration are required to gain information at larger angles.
XRR measurements also depend on the roughness at the interfaces. Calling $R_F(Q)$ the reflectivity of an ideally sharp interface, the reflectivity of a real interface with a gradually varying electron density $\rho(z)$ normalized to the value deep into the medium is given by

$$R(Q) = R_F(Q)\left|\int_{-\infty}^{+\infty}\left(\frac{d\rho}{dz}\right)e^{iQz}dz\right|^2 \approx R_F(Q)e^{-Q^2\sigma^2} \tag{2.8}$$

where the approximation holds if the density profile can be modeled as an error-function with width σ. As an example, in Fig. 2.5 the reflectivity spectrum obtained from a gold thin film sample on crown glass is shown, together with a fitted curve for the data analysis. For multilayer samples, more complex oscillation patterns are obtained, which can be reproduced by means of a transfer-matrix method study. Analysis of experimental data collected in this thesis work was conducted with the program Maud [29], which can be used also for the analysis of diffraction spectra.

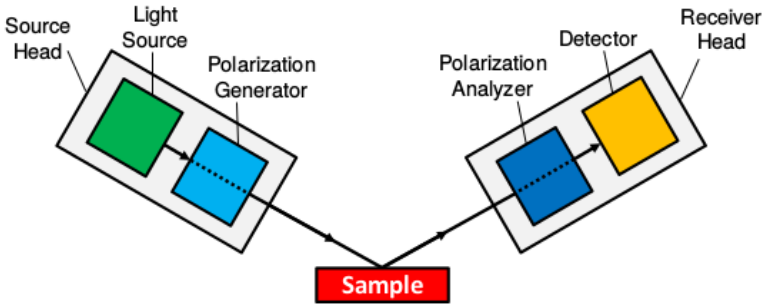

Figure 2.6: Schematic setup of an ellipsometry experiment

2.5 Variable Angle Spectroscopic Ellipsometry

Ellipsometry is an optical technique used to characterize both thin films and bulk materials, allowing the determination of their optical constants and thickness.
Ellipsometry is a model dependent technique, as the physical values directly measured do not coincide with the properties of interest. Instead, a model must be built in which the optical constants and thicknesses are used as parameters. The values obtained from the model are then compared with the experimental ones, and the characteristic properties are obtained with a best fitting procedure. The ellipsometer used in the present work is a Woollam Vase spectroscopic ellipsometer equipped with the WVASE analysis software.
The general schematic setup for an ellipsometer is showed in Fig. 2.6. Light of a given wavelength is generated from a combination of light sources together with a monochromator. The light beam is then filtered by a polarizing filter to obtain a linearly polarized light beam. As the beam impinges on the sample, its polarization state changes because of the sample characteristics, usually causing the beam to become elliptically polarized. The polarization state of the reflected beam is measured by filtering it with a second polarizing filter, called analyzer, and measuring the intensity of the transmitted beam with a solid state detector. The analyzer is set to rotate at constant frequency, causing the intensity signal to vary sinusoidally in time. By converting this intensity signal, it is possible to calculate the complex parameter [30]

$$\tilde{\rho} = \frac{\tilde{r}_p}{\tilde{r}_s} = tan\Psi \; e^{i\Delta}, \tag{2.9}$$

which is defined as the ratio of the complex Fresnel reflection coefficients for p-polarized and s-polarized light. The parameter $\tilde{\rho}$ is commonly expressed in terms of the angles Ψ and Δ, such that $tan\Psi$ equals the magnitude of the ratio of the Fresnel reflection coefficients, and Δ is their phase difference. These are the physical quantities which are directly measured and that must be compared with the predictions of a suitable model. It is worth noting that in ellipsometry the measurements are either a ratio or a difference between two values, instead of absolute measurements. Therefore, they are intrinsically more accurate than an absolute measurement of the sample reflectance, for example. In order to find the best-fit values for the chosen parameters, one has to choose a proper maximum likelihood

estimator, such that it's always positive and it reaches an absolute minimum when the calculated data matches the experimental data as close as possible. In the VASE analysis, one usually uses the mean-squared error (MSE), defined as

$$MSE = \sqrt{\frac{1}{2N-M}\sum_{i=1}^{N}\left[\left(\frac{\Psi_i^{(mod)}-\Psi_i^{(exp)}}{\sigma_{\Psi,i}^{(exp)}}\right)^2+\left(\frac{\Delta_i^{(mod)}-\Delta_i^{(exp)}}{\sigma_{\Delta,i}^{(exp)}}\right)^2\right]}, \tag{2.10}$$

where N is the number of (Ψ, Δ) pairs, M is the number of fitted parameters in the model, and the labels (mod) and (exp) refer to values obtained from the model and from experimental measurements, respectively. The minimum value for the MSE is found by means of Levenberg-Marquardt algorithm.
The implementation of ellipsometric measurements at different wavelengths and angles of incidence on the sample (Variable Angle Spectroscopic Ellipsometry, or VASE) allows to determine the optical constants across the spectrum. The experimental setup for VASE used in this thesis work allows also to conduct reflectance and transmittance measurements. In reflection it's not possible to explore angles smaller than 15° due to the finite dimensions of the light source and the detector. It is possible to explore angles up to 85° with respect to the sample normal, but at this value the beam footprint on the sample is already ten times bigger than its cross section,which is on the order of a few mm. Transmittance measurements can be performed for angles ranging from 0° to 75°.

2.6 Z-scan technique

The z-scan technique [31] was used to study the nonlinearity of the multilayer samples. In this technique, a single laser beam with constant power is focused by a converging lens, obtaining a high divergence beam. As the sample is translated along the optical axis of the lens, it is illuminated by a laser beam whose intensity changes with the position along the axis, being at its maximum at the lens focus and decreasing away from it. Therefore, it is possible to study the nonlinear properties of a sample as they get more significant at increasing intensity.
The technique aims at measuring the nonlinear components of the refractive index and absorption coefficient of the sample, described in Eq. (1.97) and (1.98). A change in the absorption coefficient alters the transmittance of the sample. For negative values of the nonlinear absorption coefficient (saturable absorption), an increase of the transmittance is obtained at higher intensities. A positive value of β (reverse saturable absorption), on the other hand, causes a minimum in the transmittance for positions of the sample close to the focus of the lens. These effects can then be studied simply by measuring the transmittance of the sample during the z-scan, with a power detector collecting all the transmitted light. This experimental configuration is called open aperture, or OA.
A nonlinear refractive index produces a different phase change of the electromagnetic wave as it propagates through the medium. When the sample is illuminated with a Gaussian beam (a beam with a Gaussian radial distribution of intensity, see Appendix A), different

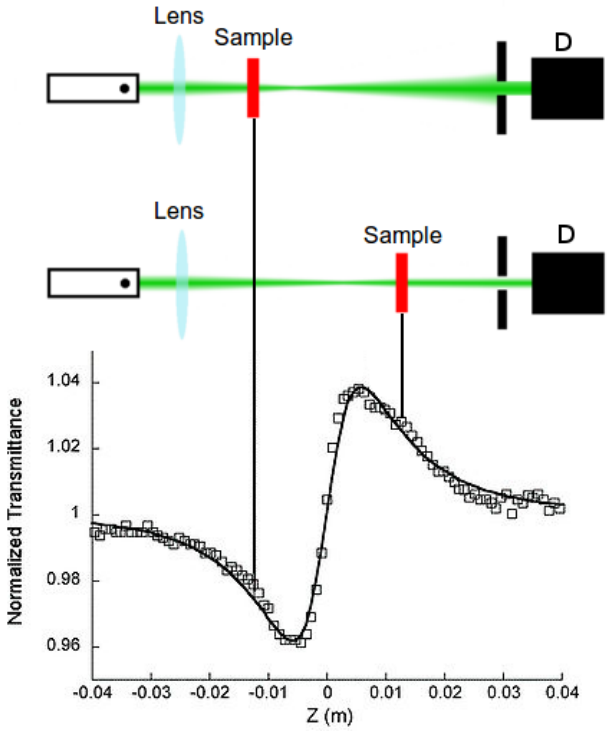

Figure 2.7: Schematic setup of a closed aperture z-scan acquisition for a nonlinear sample with $n_2 > 0$ and $\beta = 0$.

points of the wavefront "see" different values of the refractive index. If a collimated laser beam with a planar wavefront impinges on the sample, the wavefront for the output beam will be modified. When the nonlinear refractive index term n_2 is positive, the portion of the wavefront close to the optical axis propagates through a medium with a bigger refractive index than the outer portion, hence it accumulates a bigger phase delay. This effect changes the wavefront in the same way as a converging lens does. With the same reasoning, a negative n_2 causes a diverging effect on the laser beam. One important aspect is that the "focal length" of the nonlinear medium depends on the power of the laser beam. The effect of a nonlinear refractive index can be measured in a z-scan, using a power detector with a closed aperture (CA) put in front of it. For example, in Fig. 2.7 a nonlinear sample having positive n_2, $\beta = 0$, and small thickness with respect to the laser beam Rayleigh range is considered. Away from the focus, the intensity is usually too small for the nonlinear term to be significant, and the sample is in the linear regime. As the sample is brought closer to the lens focal point, while remaining on the left of it, the sample will act as converging lens focusing the laser beam before the lens focus. The light distribution on the aperture will then be widened, and less light power will pass it causing the transmittance to decrease. When the sample is exactly at the focus it won't actually modify the laser beam, and the transmittance value of the linear regime is obtained again. On the right of the lens focus and close to it, the sample will focus more light through the aperture, leading to an increase in the measured transmittance. Eventually, close to the aperture, the intensity decreases and the sample returns to the linear regime. Summarizing, the CA transmittance graph

for a nonlinear sample with a positive n_2 (and $\beta = 0$) shows a minimum on the left of the lens focus, and a maximum on its right. This trend is inverted for a sample with $n_2 < 0$. Furthermore, this simple description applies to a sample with a nonlinear refractive index and with negligible nonlinear absorption. This is not the case for most nonlinear samples, in which both effects are simultaneously observed. When this happens, the nonlinear absorption significantly modifies the transmittance measurements in the CA configuration. For example, a positive β causes the transmittance values to decrease around the lens focus with respect to Fig. 2.7, making the maximum more difficult to be detected. This effect can be taken in account by measuring the transmittance both in the OA and in the CA configuration, and correcting the absorbance effects in the CA acquisition with the data obtained from the OA one. The two measurements can be performed simultaneously by interposing a beamsplitter on the path of the output laser beam, and using the two beams for OA and CA measurements, separately.
Once data from a z-scan have been collected, signals obtained in the OA and the CA detectors are analyzed with the same fit function. The fit function for the transmittance measurements is given by [32]

$$T = 1 + \frac{(1-S)^{\mu} sin\xi}{S(1+x^2)}\Delta\Phi_0 - \frac{1-(1-S)^{\mu} cos\xi}{S(1+x^2)}\Delta\Psi_0, \tag{2.11}$$

in which several definitions have been introduced. First of all, S is the linear transmittance of the aperture, which is equal to 1 in the OA configuration. For CA configuration measurements, S must be directly measured, or it can be estimated as $S = 1 - exp(-2r_a^2/W_a^2)$, with r_a being the aperture radius and W_a being the beam radius at the aperture. Furthermore, being $x = z/z_R$ the normalized position of the sample with respect to the lens focus ($z_R = \pi W_0^2/\lambda$ is the Rayleigh range, with W_0 being the beam waist), the following adimensional quantities are defined:

$$\mu = \frac{2(x^2+3)}{x^2+9}, \tag{2.12}$$

$$\xi = -\frac{4\ x\ ln(1-S)}{x^2+9}. \tag{2.13}$$

Additionally, in terms of the linear absorption coefficient α_0 and the real length L of the sample, one defines the sample effective length as

$$L_e = \frac{1-e^{-\alpha_0 L}}{\alpha_0}. \tag{2.14}$$

Eventually, the quantities $\Delta\Phi_0$ (which represents the phase shift of the light beam) and $\Delta\Psi_0$ are related to the nonlinear refractive index and absorption coefficients, as well as the effective length and the intensity I_0 at the focus:

$$\Delta\Phi_0 = \frac{2\pi}{\lambda} n_2 I_0 L_e, \tag{2.15}$$

$$\Delta\Psi_0 = \frac{1}{2\sqrt{2}}\beta I_0 L_e. \tag{2.16}$$

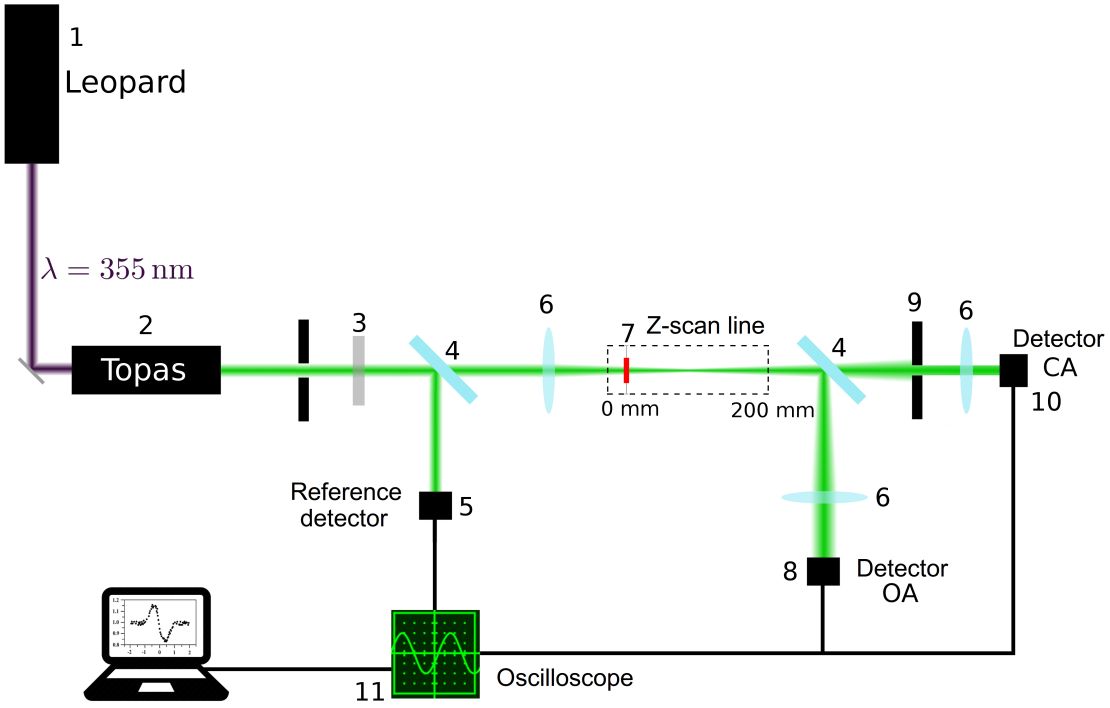

Figure 2.8: Schematic setup for the implementation of the z-scan technique.

For OA measurements $S = 1$, and Eq. (2.11) reduces to

$$T_{OA} = 1 - \frac{1}{1+x^2}\Delta\Psi_0 = 1 - \frac{\beta I_0 L_e}{2\sqrt{2}(1+x^2)}. \tag{2.17}$$

Data acquired in the OA configuration are analyzed first, obtaining a best fit value for the quantity $\beta I_0 L_e$. The results from this analysis are then used to study the data from the CA detector.

The z-scan measurements were implemented with the apparatus shown schematically in Fig. 2.8. Numbers are used to indicate different elements of the system. The laser beam used in the z-scan originates from an Optical Parametric Amplifier (2), which in turn is pumped by a *ps* pulsed laser (1) (Leopard).

The Leopard laser emits single pulses of duration $\Delta t \lesssim 20\ ps$, and at a repetition rate of 10 Hz. It consists of a solid-state laser whose active medium is an yttrium aluminum garnet doped with neodimium (Nd:YAG). It emits light at a fundamental wavelength of 1064 nm, and it is equipped with modules for Second Harmonic Generation (SHG) at 532 nm and Third Harmonic Generation (THG) at 355 nm. For the implementation of the z-scan technique, the third harmonic was used to pump the Optical Parametric Amplifier (OPA). At $\lambda = 355\ nm$ an average pulse energy of $\sim 11\ mJ$ was measured, with a standard deviation less than the 3%. The short pulses are obtained by implementation of passive mode-locking, using a saturable absorber in the optical cavity of the laser.

The OPA (2) can be used to change the wavelength of the laser beam, obtaining values from 420 nm up to 2400 nm (with the third harmonic of the Leopard laser in input). The conversion efficiency varies across the spectrum. In this thesis work, wavelengths in the

visible range were explored. The wavelength conversion happens by means of a nonlinear birifrangent crystal, in which the Difference Frequency Generation (DFG) is employed. In this process, two beams with different frequencies ω_3 and ω_1 ($\omega_3 > \omega_1$) impinge on the crystal, causing the emission of light with frequency $\omega_2 = \omega_3 - \omega_1$ in output. In terms of energy levels, the process can be described in the following way: the higher frequency beam (referred to as the pumping beam) excites atoms in the crystal up to a virtual level, whereas the lower frequency beam stimulates a de-excitation from this level. Because of the mismatch in energy, as a photon with frequency ω_3 disappears, the emission of a photon of frequency ω_1 must be accompanied by a photon of frequency ω_2 as well. In addition to the conservation of energy, expressed by the equation $\hbar\omega_3 = \hbar\omega_1 + \hbar\omega_2$, the process must satisfy a momentum-matching condition in order to happen efficiently:

$$\hbar\mathbf{k}_3 = \hbar\mathbf{k}_1 + \hbar\mathbf{k}_2. \tag{2.18}$$

This momentum-matching condition for photons is often referred to as a phase-matching conditions for electromagnetic waves.
In the OPA used in this thesis work, the laser beam from the Leopard laser corresponds to the pumping beam. This beam passes several times through the nonlinear crystal, each time converting part of its energy into photons with frequency ω_1 by means of superfluorescence in the crystal. Therefore, as the pumping beam gets depleted, the DFG process becomes significative and photons with frequency ω_2 are produced. If one considers an arbitrarily high intensity pumping beam and an ideal nonlinear crystal, the intensities of the two beams are found to grow exponentially with the traveled length in the crystal. Eventually, the frequency of the two beams can be changed by rotating the nonlinear crystal, thus changing the pair of frequencies which better satisfies the phase-matching condition expressed in Eq. (2.18). The two beams of frequencies ω_1 and ω_2 both exit from the OPA. Here, an appropriate filter is used to block the ω_1 beam, in order to obtain a monochromatic beam.
The output beam of the OPA passes through a Keplerian telescope (not shown in figure), built with two planar-converging lenses of similar focal lengths. A pinhole is positioned at the focus of the two lenses, in order to spatially filter the light beam and obtain a Gaussian beam in output. The light beam passes through an optical density filter (3) used to control the power of the light beam by means of attenuation. It is worth noting that, if the power of the beam is too high, the beam intensity on the sample during the scan can increase enough to damage the sample itself. On the other hand, high intensity beams are required to induce nonlinear phenomena. Therefore, the optimal combination of optical density filters must be found at each wavelength. After being attenuated, the light beam reaches a beam splitter (4), where part of the beam is redirected towards a reference detector (5). This detector is used to monitor the laser beam power, in order to normalize the measurements of the other two detectors. Eventually, the laser beam which passes through the beamsplitter is used for the z-scan itself. The beam is collimated when it impinges on the converging lens (5), and it is therefore focused at a distance equal to the

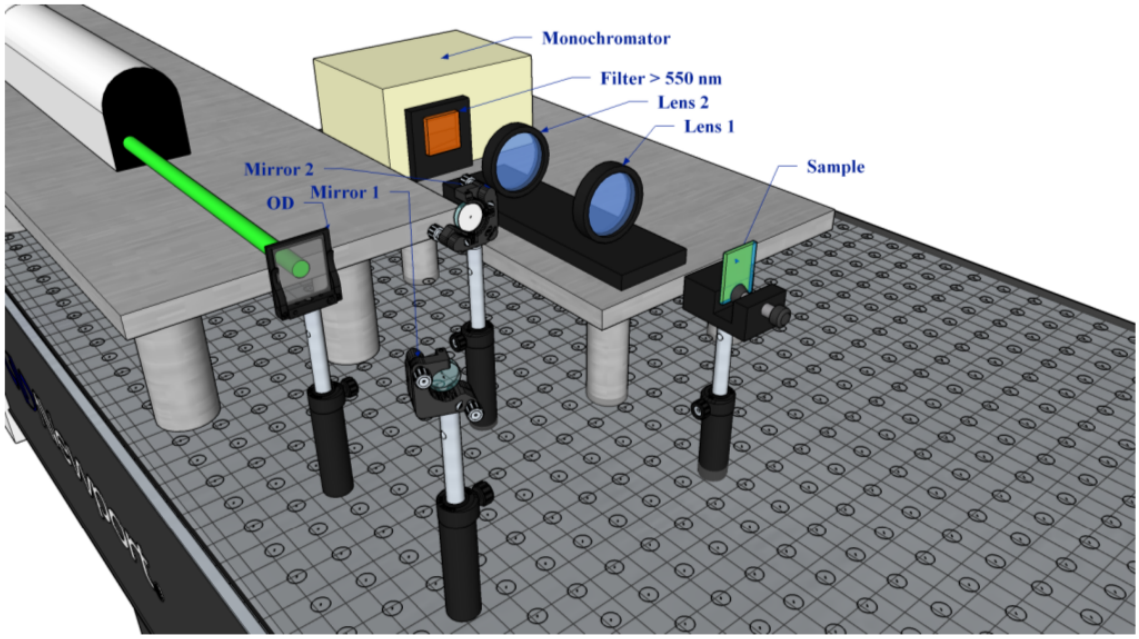

Figure 2.9: Schematic setup for the photoluminescence measurements.

lens focal length, $f = 200\ mm$. The sample (7) can be positioned at several positions in a range of 200 mm across the focal point. After passing through the sample, the light beam is splitted by a second beamsplitter. The transmitted beam is collected by a photodiode detector (10) with an iri diaphragm (9) positioned in front of it (CA configuration), whereas the reflected beam is measured by a photodiode detector (8) with no aperture in front of it (OA configuration). The current signals of the three detectors (reference, CA, and OA) are sent to three independent input channels of an oscilloscope (11), where they get converted into voltage signals by means of a simple 50 Ω resistor. For each position of the sample during the z-scan, several light pulses are collected by triggering the signal acquisition on the reference detector. The oscilloscope calculates the averages of the signals measured on each detector and passes them to a PC for data analysis.

2.7 Photoluminescence measurements

The high-k states of the hyperbolic metamaterial were investigated by means of photoluminescence measurements. The spectrum and lifetime of emitters positioned close to the HMM are affected by the increased photonic density of states, as predicted by Fermi's golden law [33].

The experimental setup for the photoluminescence measurements is described in Fig. 2.9. The emitters were pumped with a pulsed laser, emitting at $\lambda = 355\ nm$ pulses lasting 4.5 ns at a repetition rate of 10 Hz. The wavelength of interest was reached using the third harmonic of a solid state Q-switched Nd:YAG laser. The active medium of this laser is a garnet of yttrium and aluminum ($Y_3Al_5O_{12}$) doped with neodymium (Nd), which is excited by stroboscopic lamps at a frequency of 10 Hz. The laser pulses were directed onto the

sample by means of two highly reflective mirrors (adapt for ns pulsed beams), impinging on the sample at an angle of about 40°. The emitted light was collected perpendicularly to the sample, by means of two converging lenses which focused the light on the entrance slit of a single grating monochromator. The monochromator was used to select the measured wavelength. A longpass filter was positioned before the monochromator, in order to prevent scattered light from the laser to enter inside the detector. The emitted light was detected with a photomultiplier tube (Hamamatsu, model R928). Depending on the sample under study, optical densities filters were placed in front of the laser to reduce the light intensity, preventing the sample from photobleaching. Filters were positioned also in front of the monochromator to avoid saturation of the detector. For steady-state photoluminescence measurements, the signal from the detector was acquired with a lock-in amplifier, whose reference signal was given by the laser itself. Spectra of the emission intensity were acquired in the range $500\ nm < \lambda < 700\ nm$ with a step of $2\ nm$ and a delay of $0.5\ s$ between each measurement. For each sample, 4 spectra were acquired and averaged, sending the final spectrum to a computer. For time-resolved photoluminescence measurements, the signal from the detector was sent to an oscilloscope. Here, the decay spectrum for each sample was obtained as the average over 500 acquisitions. For each sample, a total of 5 decay spectra was acquired, changing every time the impinging point of the laser beam. Each of these spectra was sent to the computer for an independent fit, and the average of their decay times was taken.

Chapter 3

Results: Simulations

3.1 Effective Medium Approximation of an Al_2O_3/Au multilayer

A multilayer composed of alternating thin layers of gold (Au) and alumina (Al_2O_3) was studied in this thesis as an implementation of an hyperbolic metamaterial. In Fig. 3.1 the bulk permittivities of the two materials are plotted together at visible wavelengths. The real part of gold permittivity is negative, and follows a Drude-like dispersion for $\lambda > 600\ nm$. The imaginary part is positive, non-negligible, and grows up to $\varepsilon_2 = 12$ at $\lambda = 1600\ nm$. Alumina has a positive real permittivity slightly affected by dispersion, whereas its imaginary component is negligible.

Substituting the permittivities of gold and alumina in Eq. (1.57) and (1.61), an effective medium is obtained with complex principal components. Evaluating the real parts of $\varepsilon_{\parallel}$ and $\varepsilon_{\perp}$, one finds that the medium can behave like an effective dielectric (all principal components are positive), an effective metal (all principal components are negative) or a Type II HMM ($\varepsilon_{\parallel} < 0$ and $\varepsilon_{\perp} > 0$), depending on the metal filling fraction ρ_m and on the wavelength λ. In Fig. 3.2 the optical behavior of the effective medium is shown in the $\rho_m - \lambda$ plane. At low filling fractions, a transition from an effective dielectric to a Type II HMM occurs when the real part of the in-plane permittivity $\varepsilon_{\parallel}$ changes sign; this happens across the Epsilon-Near-Zero (ENZ) wavelength λ_{ENZ}. For $\lambda < \lambda_{ENZ}$ the in-plane permittivity is positive, whereas for $\lambda > \lambda_{ENZ}$ becomes negative; across this transition, the out-of-plane permittivity remains positive. The value of λ_{ENZ} varies with the filling fraction of the metal, as greater concentrations of gold move λ_{ENZ} to shorter wavelengths. At greater filling fractions negative values of the out-of-plane permittivity are observed, but only in a range in which the in-plane permittivity is always negative. Therefore, at these filling fractions the medium behaves like an effective metal, while the Type I HMM regime ($\varepsilon_{\parallel} > 0$ and $\varepsilon_{\perp} < 0$) is never obtained. This result depends on the particular choice of metal and dielectric. It is worth noting that the Type II HMM regime occupies a broadband wavelength region. In fact, the homogenization of the effective medium theory has a non-resonant nature.

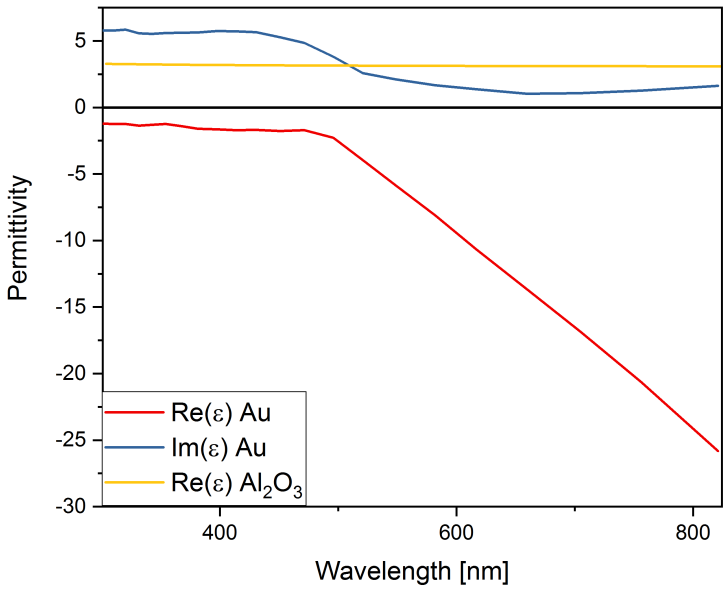

Figure 3.1: Permittivities of gold (Au) and alumina (Al_2O_3) measured on bulk samples [34] [35] in the visible region of the spectrum.

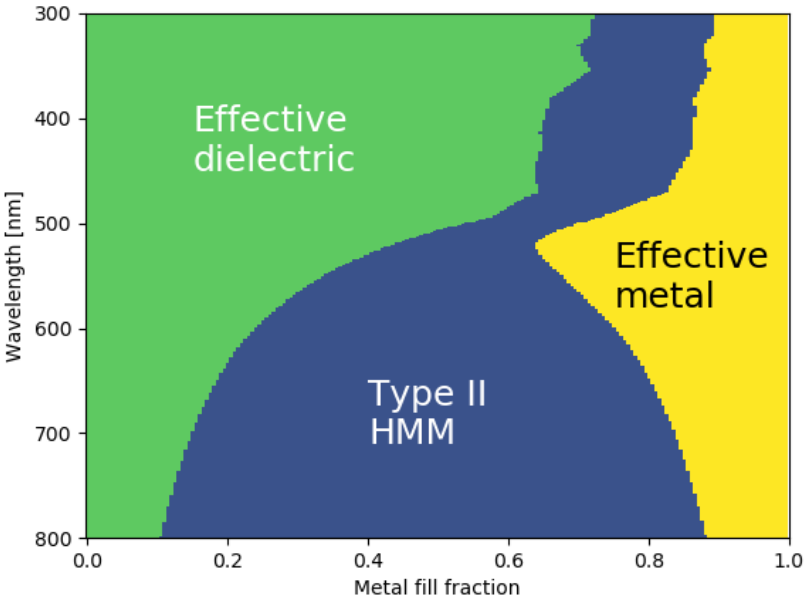

Figure 3.2: Optical phase diagram for an Al_2O_3/Au multilayer at optical frequencies. The effective medium can either be an effective dielectric ($\varepsilon_\parallel > 0$, $\varepsilon_\perp > 0$), an effective metal ($\varepsilon_\parallel < 0$, $\varepsilon_\perp < 0$), or a Type II HMM ($\varepsilon_\parallel < 0$, $\varepsilon_\perp > 0$), depending on the metal filling fraction and on the wavelength.

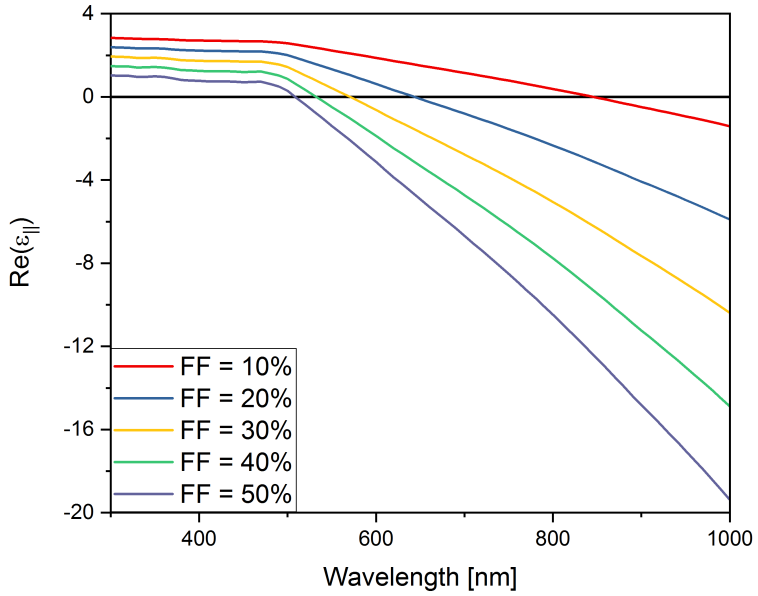

(a)

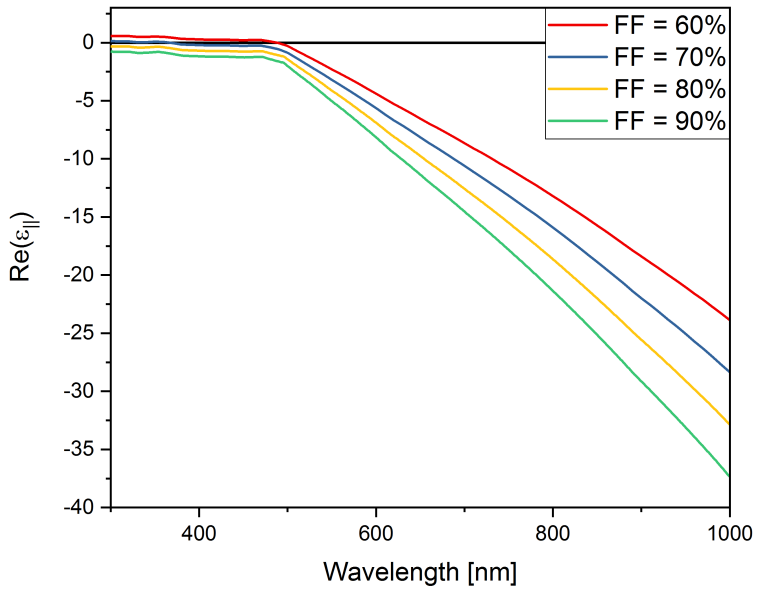

(b)

Figure 3.3: Real components of the in-plane permittivity for the Al_2O_3/Au multilayer described as an effective uniaxial medium, with metal filling fraction (FF) varying from 10% to 50% (a) and from 60% to 90% (b). The permittivities were calculated with the bulk permittivities of Au and Al_2O_3.

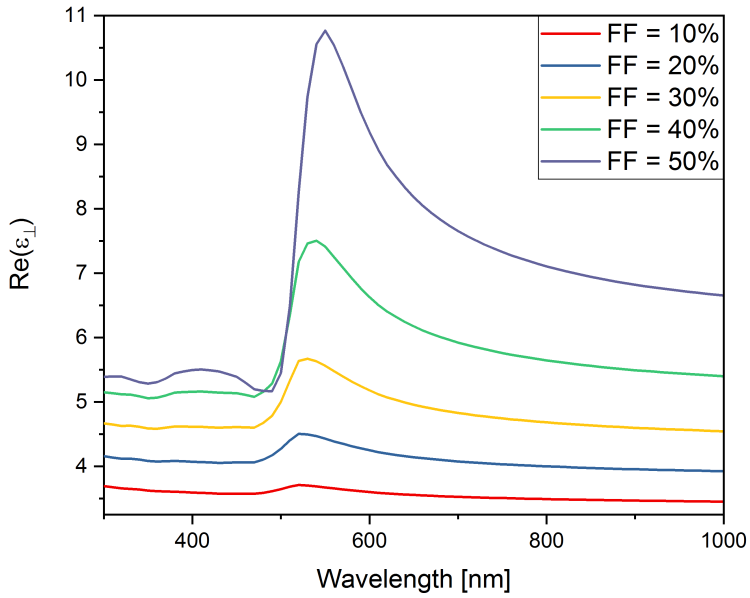

(a)

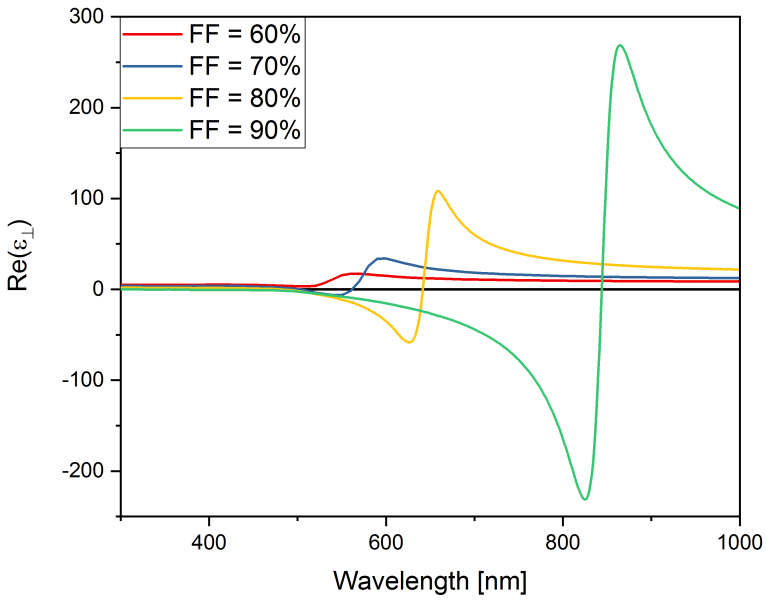

(b)

Figure 3.4: Real components of the out-of-plane permittivity for the Al_2O_3/Au multilayer described as an effective uniaxial medium, with metal filling fraction (FF) varying from 10% to 50% (a) and from 60% to 90%. The permittivities were calculated with bulk permittivities of Au and Al_2O_3.

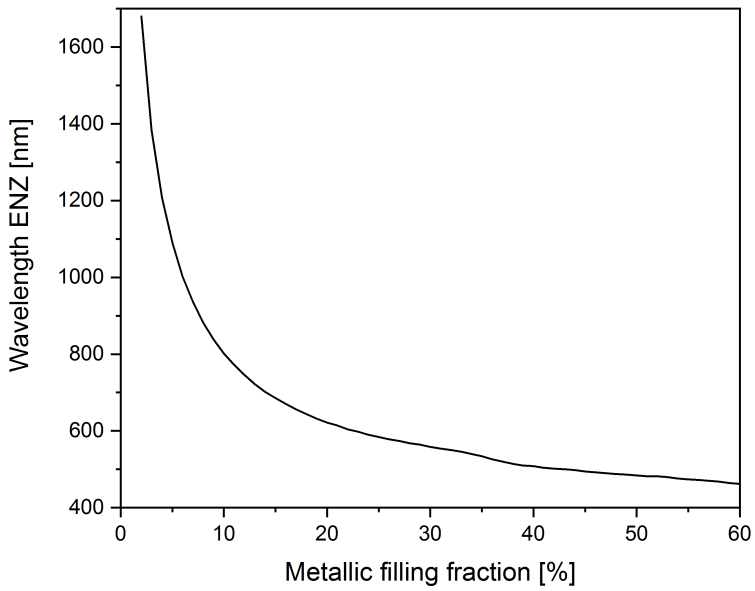

Figure 3.5: Epsilon-Near-Zero wavelength λ_{ENZ} plotted as a function of the Al_2O_3/Au multilayer filling fraction. λ_{ENZ} is the wavelength at which the real component of the in-plane permittivity changes sign. The plot was computed using experimental values for gold and alumina thin films.

In Figs. 3.3a - 3.4b the real parts of the in-plane and out-of-plane permittivities are plotted across the visible and near-IR spectrum for different values of the filling fraction. These values were computed using the bulk permittivities of gold and alumina, obtained from [34] and [35], respectively. To further develop our simulations, experimental values of the permittivities of thin films of gold and alumina were used. Nonetheless, the shapes of the permittivity curves are not dramatically affected by these corrections. It is worthwile plotting the value of λ_{ENZ} as a function of the filling fraction, as seen in Fig. 3.5.

3.2 Simulation methods

The software package S^4 [36] was employed to simulate the reflectance and transmittance spectra of different samples, as functions of the vacuum wavelength λ_0, of the incident polar angle θ, and of the light polarization. S^4 (which stands for Stanford Stratified Structure Solver) implements a Fourier modal method (FMM) to compute the modal expansions of the electromagnetic fields inside layers, together with a scattering matrix method (SMM) algorithm to join modes at the layer borders. In the FMM, the electromagnetic fields in each layer are expanded into eigenmodes with an exponential dependence in the normal direction. The expansion is expressed in terms of a Fourier basis in the plane of periodicity. At the interfaces between layers, the expansion coefficients are related by the field continuity conditions. This corresponds to diagonalizing in the modal basis the scattering

matrix of each layer, in order to combine the total scattering matrix of the system as a combination of scattering matrices of adjacent layers. This approach is suited to simulate multilayered structures in which each layer may have inclusions in the x-y plane, but is homogeneous along the z-direction, which is the direction along which the layers are stacked one above the other.
In all the simulations, the examined structure is embedded between an infinitely thick superstrate and an infinitely thick substrate, both of which are lossless. The software allows to compute, at a given coordinate along the z-axis, the z-component of the Poynting flux integrated over a unit cell surface normal to the z-direction. In other words, one can compute the radiant power propagating forward and backward in a layer, at a given position along the z-axis. In terms of this quantity, the main quantities of interest are the reflectance from the sample and the transmittance through the sample. With light impinging on the sample from the superstrate, the reflectance from the sample is thus defined as the ratio between the power propagating away from the top surface of the system and the power propagating towards it. Similarly, the transmittance is defined as the ratio between the power propagating away from the bottom surface of the sample and the power propagating towards the top surface. Reflectance and transmittance are the physical observables which are computed by means of simulations to characterize a particulare structure, and which can be compared to physical measurements. For multilayered structures, the power propagating forward inside each layer can be evaluated as well.
As these quantities are evaluated to infer the modes of the simulated system, it's worth plotting them as a function of the angular frequency ω and of the tangential component of the wavevector $k_{\parallel}$:

$$k_{\parallel} = n_{sup}\frac{2\pi}{\lambda_0}sin\theta,$$

$$\omega = \frac{2\pi c}{\lambda_0},$$

where n_{sup} is the refractive index of the superstrate, and θ is the angle of incidence with respect to the normal. In fact, in the previous discussions it was observed that for Type II HMMs a critical value of the tangential wavevector must be reached in order to have propagating waves inside the medium. An additional y-axis has been added to the graphs to indicate the corresponding vacuum wavelength $\lambda_0 = 2\pi c/\omega$. The results shown in the following paragraphs regard mainly the simulation of effective mediums and multilayers with a metallic filling fraction of 33%. With this choice of filling fraction, the Epsilon-Near-Zero wavelength λ_{ENZ} is located at 546 nm. For all the simulation cases, the vacuum wavelength ranged from 450 nm up to 1700 nm, with steps of approximately 10 nm. The angle of incidence ranged from 0° up to 80°, with steps of either 2° or 4°, depending on the complexity of the simulated system. The azimuthal angle φ between the projection of the wavevector on the plane and the x-axis was set to zero in all simulations. For simulations of multilayers, the choice of φ does not affect the results, due to the azimuthal symmetry with respect to the z-direction. Instead, when nanohole arrays are considered, the choice of φ corresponds to a precise experimental configuration. The resolution parameter in this type

of simulations is given by the number of Fourier bases in which the electromagnetic field is decomposed. Each system has been simulated for increasing values of this parameter, until results reached convergence within 0.05 (for values normalized to 1).

3.3 Far-field coupling with a prism

The predictions of the EMA are evaluated by simulating the optical response of a 1 μm thick layer with uniaxial permittivity computed through EMA formulas. Dielectric functions experimentally measured on thin films of gold and alumina by means of ellipsometry (see Sec. 4.3.1) have been used to calculate the principal components of the effective permittivities.

In the simulation scripts, the refractive index of the superstrate and the substrate can be assigned arbitrarily. One can then choose a high value for the refractive index of the superstrate, in order to obtain light impinging on the system with a high wavevector. This would be equivalent to a prism-coupling experiment in the Kretschmann configuration. A value of $n_{sup} = 2.8$ was chosen for the superstrate, which at optical frequencies could be theoretically obtained using TiO_2 in the form of rutile. The substrate was assigned the same refractive index value, to act as a decoupler for high-k modes that were able to propagate through the system. If the substrate's refractive index were too low to sustain the high-k modes, total internal reflection would happen in the sample and a null transmittance would be observed. In Figs. 3.6 and 3.7, reflectance and transmittance spectra for p- and s-polarized light are shown. A colorbar indicates the different values in the plane, and some lines are added as a reference. In order to correctly interpret the graphs, it is worth noting that the maximum and minimum of the colorbar for each graph change depending on the particular graph. The black horizontal solid line indicates the nominal ENZ wavelength obtained from effective medium formulas. At smaller wavelengths (in the graph, above the line), the effective permittivity $\varepsilon_{\parallel}$ is positive and the system behaves like an effective dielectric; at longer wavelengths (below the line) $\varepsilon_{\parallel}$ is negative and the system is in the Type II HMM regime. The black dashed diagonal line on the left delimitates the cone of light impinging from air: with light impinging from air, only couples $(k_{\parallel}, \omega)$ on the left of this line can be reached. It is then clear that a coupling mechanism must be employed to reach interesting points which fall outside this cone. Eventually, the black solid diagonal line on the right indicates the minimum value of the tangential wavevector, according to the effective medium theory, to have propagating modes in the system. It was computed considering the dispersion for TM waves in uniaxial media, Eq. 1.48, evaluated for $k_z = 0$, giving $k_{\parallel} = \sqrt{\varepsilon_{\perp}}\omega/c$. Therefore, according to the effective medium theory, propagating modes for the HMM would be located in the region on the right of this line, and below the ENZ wavelength.

The reflectance and transmittance spectra can be analyzed to deduce when light is successfully coupled to the system. Particularly, minima of reflectance are found when light is able to penetrate through the sample. Looking at non-null values in the transmittance spec-

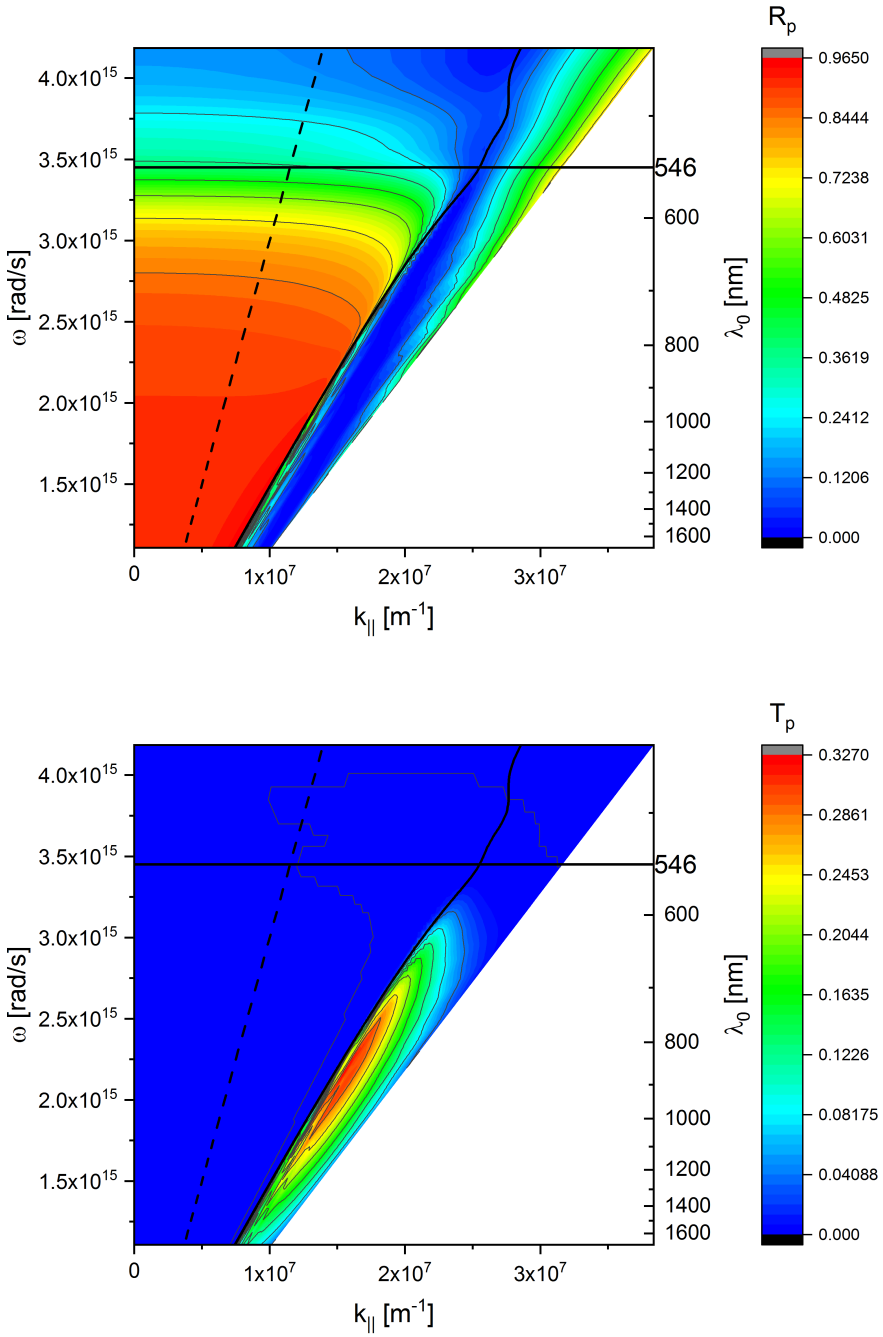

Figure 3.6: Reflectance and transmittance simulated spectra for p-polarized light impinging on a 1 μm thick effective medium with filling fraction equal to 33%. The sample is between a superstrate with $n_{sup} = 2.8$ and a substrate with $n_{sub} = 2.8$.

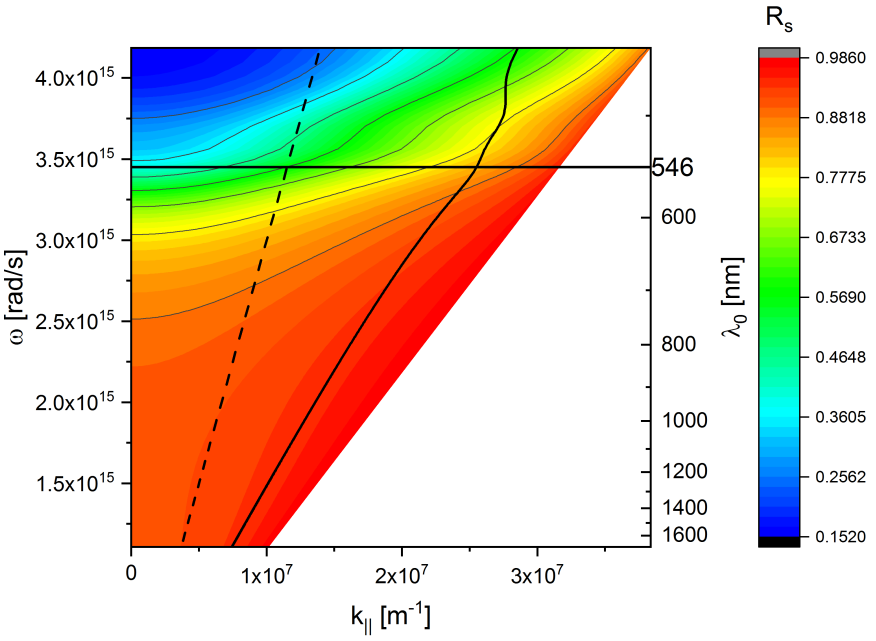

Figure 3.7: Reflectance simulated spectrum for s-polarized light impinging on a 1 μm thick effective medium with filling fraction equal to 33%. The sample is between a superstrate with $n_{sup} = 2.8$ and a substrate with $n_{sub} = 2.8$. The transmittance spectrum is null everywhere.

tra, one can infer when light is able to propagate through the system. Looking at graphs in Fig. 3.6 for p-polarized light, a region of minima is found in the hyperbolic region of the reflectance spectrum, which corresponds to a region of maxima in the transmittance spectrum. These regions indicate a group of propagating modes in the hyperbolic regime, which are distinct from the other evanescent modes. In these cases, p-polarized light impinging from the superstrate has a tangential component wavevector large enough for the TM dispersion relation inside the medium to hold with a real perpendicular component of the wavevector. Looking at the graph in Fig. 3.7, one sees instead that with s-polarized light it's not possible to excite propagating modes, since in s-polarization the electric field is always perpendicular to the optical axis of the sample. In this case the transmittance is essentially null everywhere in the dispersion plane (graph not shown).

To test the validity of the effective medium approximation (EMA), the optical response of a multilayer with equivalent thickness is simulated. To have a metallic filling fraction of 33%, the thicknesses of gold and alumina layers were fixed to 15 nm and 30 nm, respectively, to reproduce systems similar to realistic samples. With these values, to reach a total thickness close to 1 μm as in the previous simulation, a total of 44 layers (22 periods) must be considered. The reflectance and transmittance spectra for this case are shown in Figures 3.8 and 3.9. In agreement with the effective medium theory, high-k states are observed for wavelengths longer than λ_{ENZ}. In the multilayer simulation the transmittance for these modes is lower, reaching a maximum value of $\sim 24\%$, compared to the peak value of $\sim 33\%$ of the EMA simulation. Nonetheless, one must consider that it's

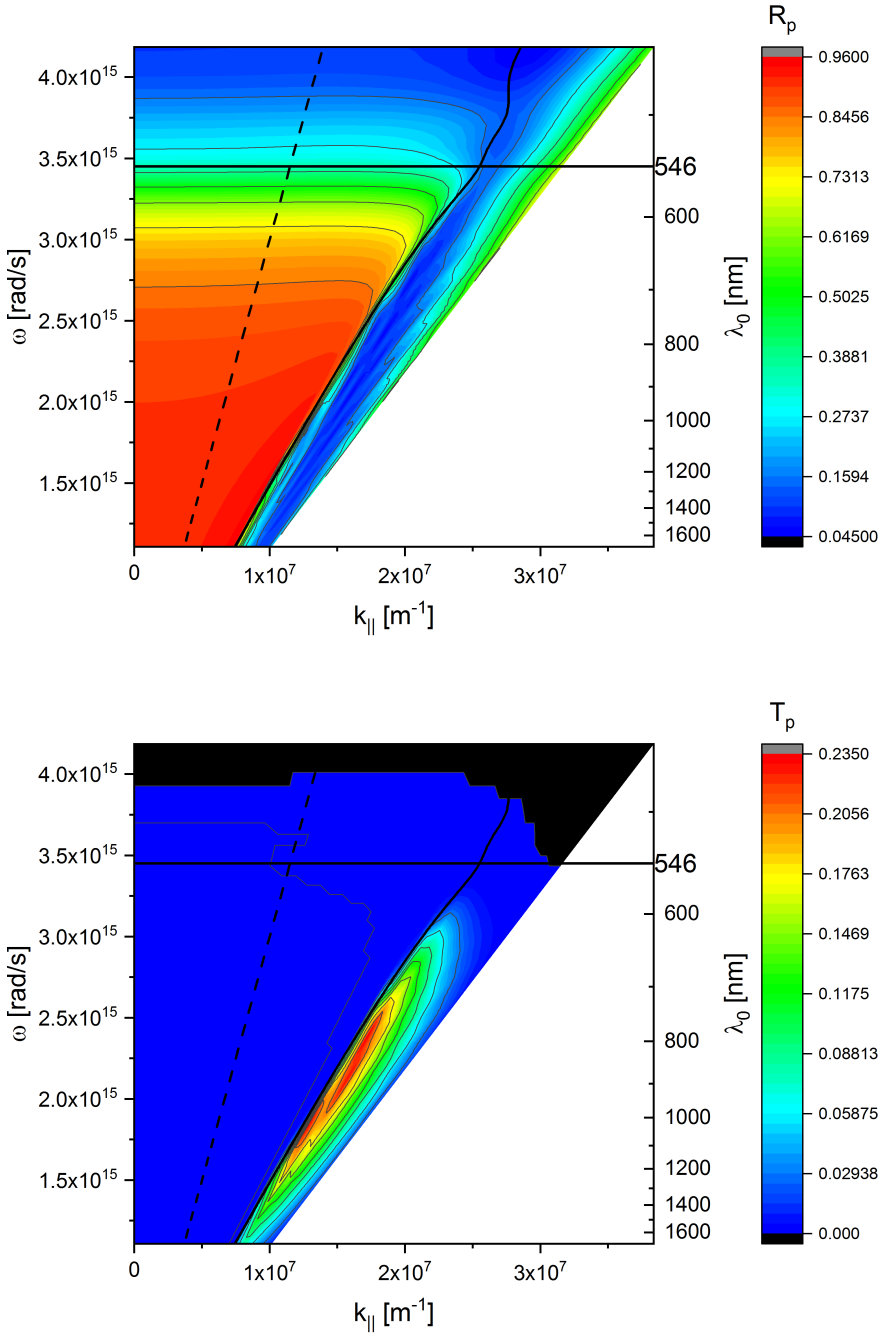

Figure 3.8: Reflectance and transmittance simulated spectra for p-polarized light impinging on a 1 μm thick multilayer composed of alternating 30 nm alumina and 15 nm gold layers. The multilayer amounts to a total of 44 layers (22 periods). The sample is between a superstrate with $n_{sup} = 2.8$ and a substrate with $n_{sub} = 2.8$.

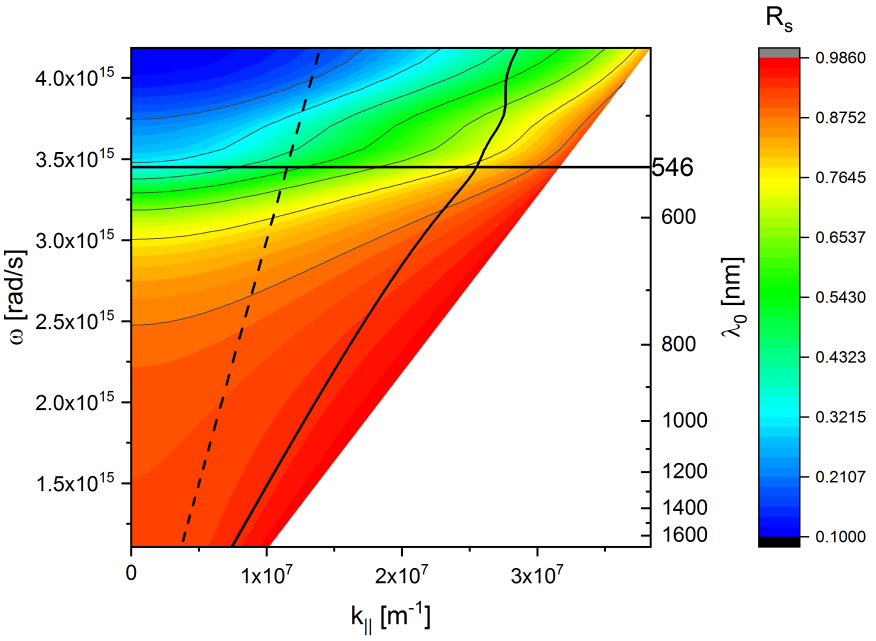

Figure 3.9: Reflectance simulated spetrum for p-polarized light impinging on a 1 μm thick multilayer composed of alternating 30 nm alumina and 15 nm gold layers. The multilayer amounts to a total of 44 layers (22 periods). The sample is between a superstrate with $n_{sup} = 2.8$ and a substrate with $n_{sub} = 2.8$. The transmittance spectrum is null everywhere.

significantly high considering that the absorption length of gold is $\gtrsim 10$ nm in this region of the electromagnetic spectrum, and that the multilayer contains an integrated quantity of 330 nm of gold.

Effective medium formula are obtained for an infinitely repeating multilayer. The optical behavior of a finite multilayer as a function of its number of periods is investigated in Fig. 3.10. In this graph, the reflectance with p-polarized light for multilayers with varying number of periods is plotted (dashed lines) and compared with the reflectance of homogeneous uniaxial layers with dielectric functions computed through effective medium formula (solid lines) for $FF = 33\%$. Starting from a single period multilayer, and increasing gradually the number of periods, one finds that a multilayer with four periods adequately approximates the response of an effective medium: the reflectance is saturated at small wavevectors up to a critical value, after which it drops to zero. The light blue solid line in Fig 3.10 indicates the simulated reflectance for an homogeneous uniaxial medium whose thickness is set equal to 180 nm, which is the overall thickness of the four-period multilayer.

In this thesis, a four-period multilayer with 30 nm thick alumina layers and 15 nm thick gold layers was thus studied as a practical realization of an hyperbolic medium. The optical response for the homogeneous hyperbolic medium with thickness equal to 180 nm is shown in Figs. 3.11, whereas the optical response of the four-periods multilayer is shown in Figs. 3.12. The spectra for the multilayer case reproduces in a good fashion the effective medium case even in the thin sample case and with a large transmittance. The overall modification

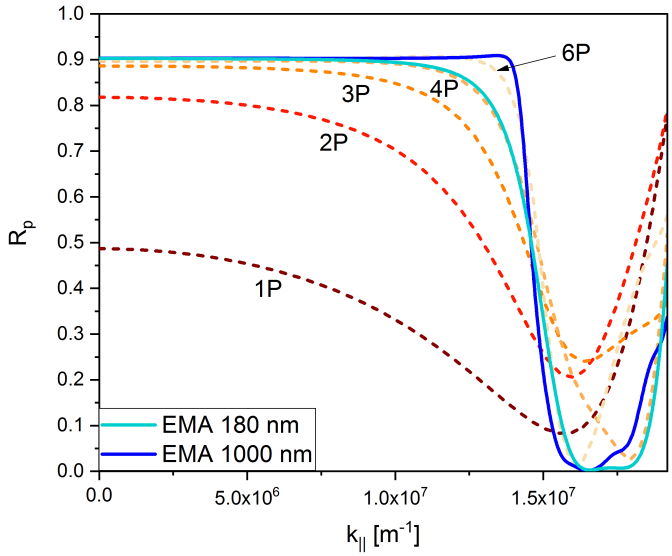

Figure 3.10: Reflectance values simulated at $\lambda_0 = 900\ nm$ for p-polarized light. Dotted lines indicate simulated reflectance for multilayers of 30 nm thick alumina layers and 15 nm thick gold layers, with increasing number of periods. Solid lines indicate simulated reflectance for media having different thicknesses, with dielectric functions computed with effective media formulas with $FF = 33\%$. The effective medium behavior (for $N \to \infty$) is approximated in an adequate way starting from 4 periods.

of the high-k band is attributed to a cross-talking effect between the two interfaces.

3.4 Far-field coupling with NHA

Nanohole arrays with an hexagonal lattice of nanoholes have been studied as a way to match external light to the internal modes of the HMM. To simulate structures which could be fabricated experimentally, the simulated NHA has been assigned typical geometrical parameters of NHAs fabricated by means of nanosphere lithography [37]. In detail, the simulated NHA is made of gold with empty holes (air). It has a thickness of 70 nm, whereas its holes have a diameter of 300 nm, and a center-to-center distance of $a = 520\ nm$, which is the fundamental spacing of the grating.

A schematic representation of the lattice in the real and reciprocal space is shown in Fig. 3.13. A 2D hexagonal lattice with spacing a can be described as a Bravais lattice whose primitive vectors are

$$\begin{cases} \mathbf{a}_1 = a\widehat{\mathbf{x}} \\ \mathbf{a}_2 = \frac{a}{2}\widehat{\mathbf{x}} + \frac{\sqrt{3}a}{2}\widehat{\mathbf{y}} \end{cases} \tag{3.1}$$

The reciprocal lattice of this grating results to be another hexagonal lattice, having lattice

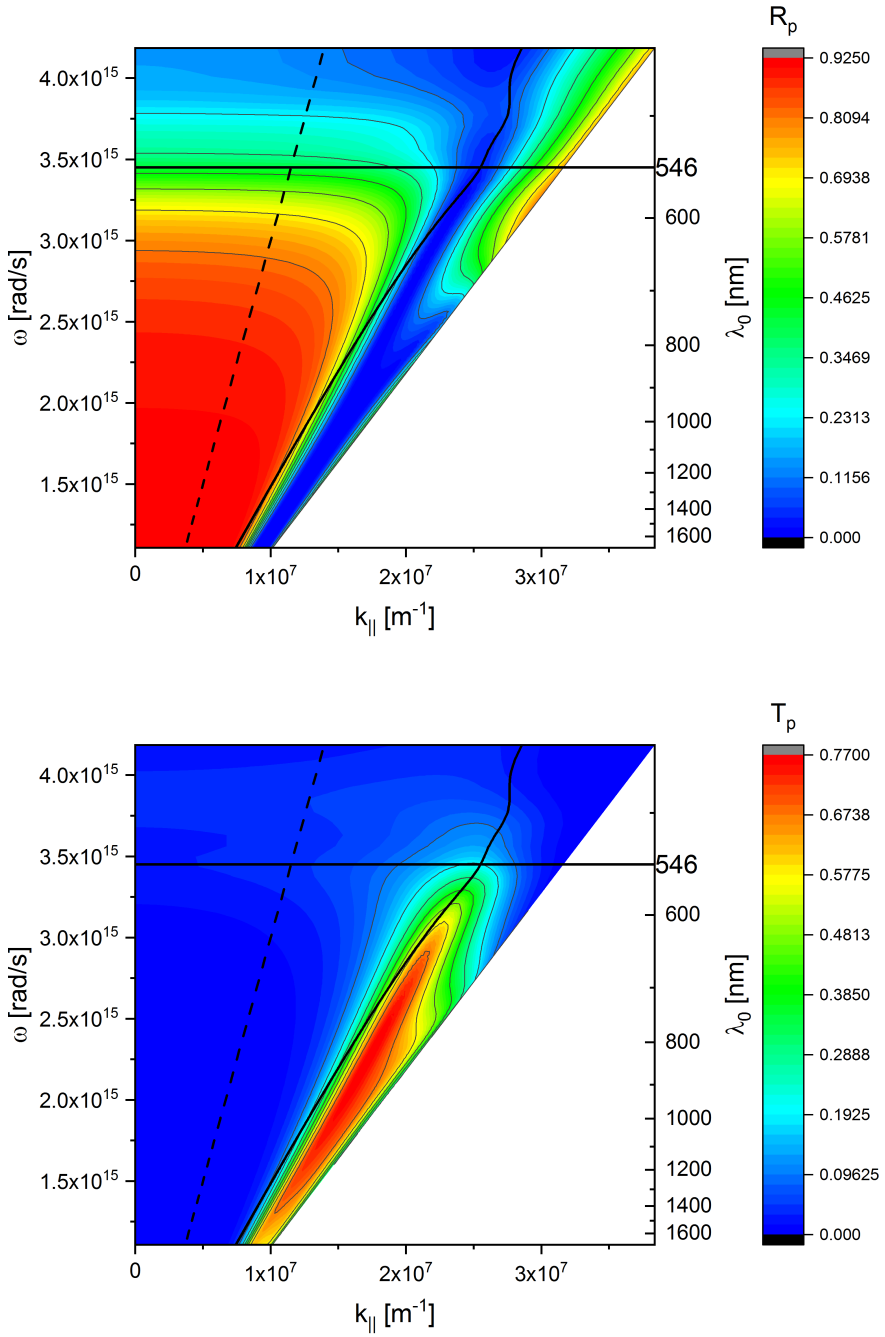

Figure 3.11: Reflectance and transmittance simulated spectra for p-polarized light impinging on a 180 nm thick effective medium with filling fraction equal to 33%. The sample is between a superstrate with $n_{sup} = 2.8$ and a substrate with $n_{sub} = 2.8$.

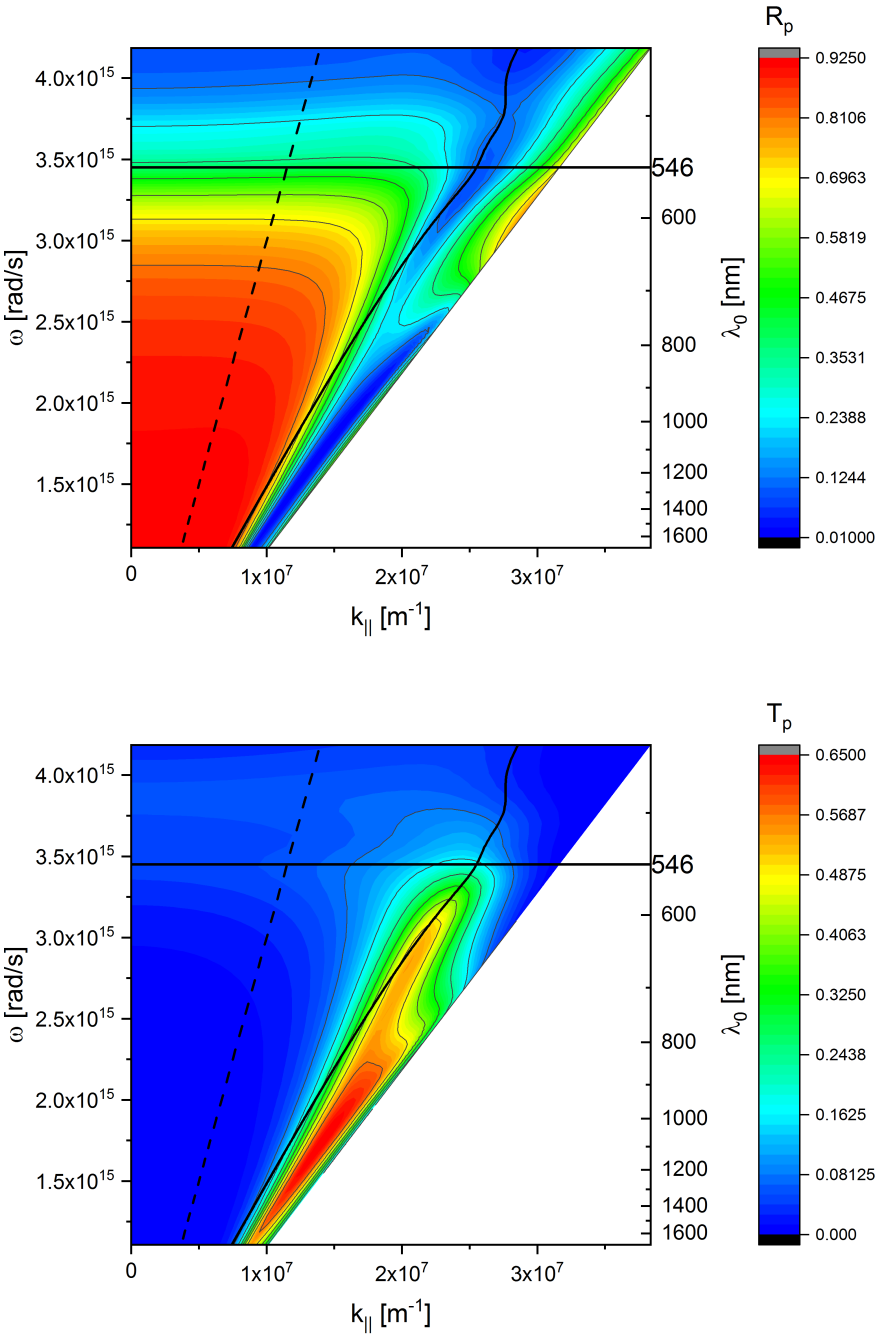

Figure 3.12: Reflectance and transmittance simulated spectra for p-polarized light impinging on a 180 nm thick multilayer composed of alternating four 30 nm alumina with four 15 nm gold layers. The sample is between a superstrate with $n_{sup} = 2.8$ and a substrate with $n_{sub} = 2.8$.

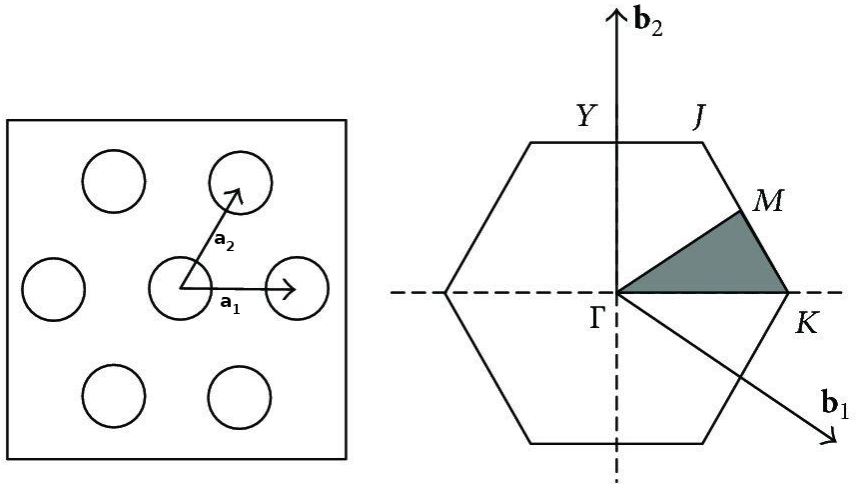

Figure 3.13: On the left, a schematic representation of the hexagonal lattice characterizing the NHA. The hexagonal lattice is described by the basis vectors $\mathbf{a}_1$ and $\mathbf{a}_2$. On the right, the basis vectors $\mathbf{b}_1$ and $\mathbf{b}_2$ describing the corresponding reciprocal lattice. The first Brillouin zone is also drawn. In all simulations, the electromagnetic field impinging on the lattice had the wavevector oriented along the $\Gamma - K$ direction.

constant $4\pi/a\sqrt{3}$, and rotated by 30° with respect to the grating. Its primitive vectors are

$$\begin{cases} \mathbf{b}_1 = \frac{2\pi}{\sqrt{3}a}(\sqrt{3}\widehat{\mathbf{k}}_x - \widehat{\mathbf{k}}_y) \\ \mathbf{b}_2 = \frac{4\pi}{a\sqrt{3}}\widehat{\mathbf{k}}_y \end{cases} \tag{3.2}$$

Unlike a unidimensional grating, a 2D hexagonal lattice can scatter light along different directions in the reciprocal space, depending on the reciprocal lattice vector. Therefore, considering Eq. 1.76, the magnitude of the diffracted wavevector will be

$$k_f = \sqrt{\left[k_{\parallel,x} + \frac{2\pi}{a}n\right]^2 + \left[k_{\parallel,y} + \frac{2\pi\sqrt{3}}{3a}(-n+2m)\right]^2}, \tag{3.3}$$

where a vector in the reciprocal lattice is represented by the couple (n, m) of indices of the basis vectors.

Figures 3.14 and 3.15 show the reflectance and transmittance spectra for a gold nanohole array with the aforementioned geometrical properties ($a = 520\ nm$, $h = 70\ nm$, $d = 300\ nm$), at p- and s- polarized incident light. Light impinges on the the NHA coming from air ($n_{sup} = 1$), and the NHA is separated by a 10 nm alumina spacer from a silica substrate ($n_{sub} = 1.45$). It is worth noting that these graphs (and the following ones) have a shorter range in the x-axis, as they correspond to modes excited with light incoming from air. Therefore, for a comparison with previous graphs, they should be set side by side with the regions in previous graphs located on the left of the black dashed line. For $\lambda > 600\ nm$, the reflectance spectrum for p-polarized impinging light on the NHA shows two bands of minima, which correspond to two bands of maxima for the transmittance. The two bands arise from the coupling of light with SPPs along the interfaces of the NHA.

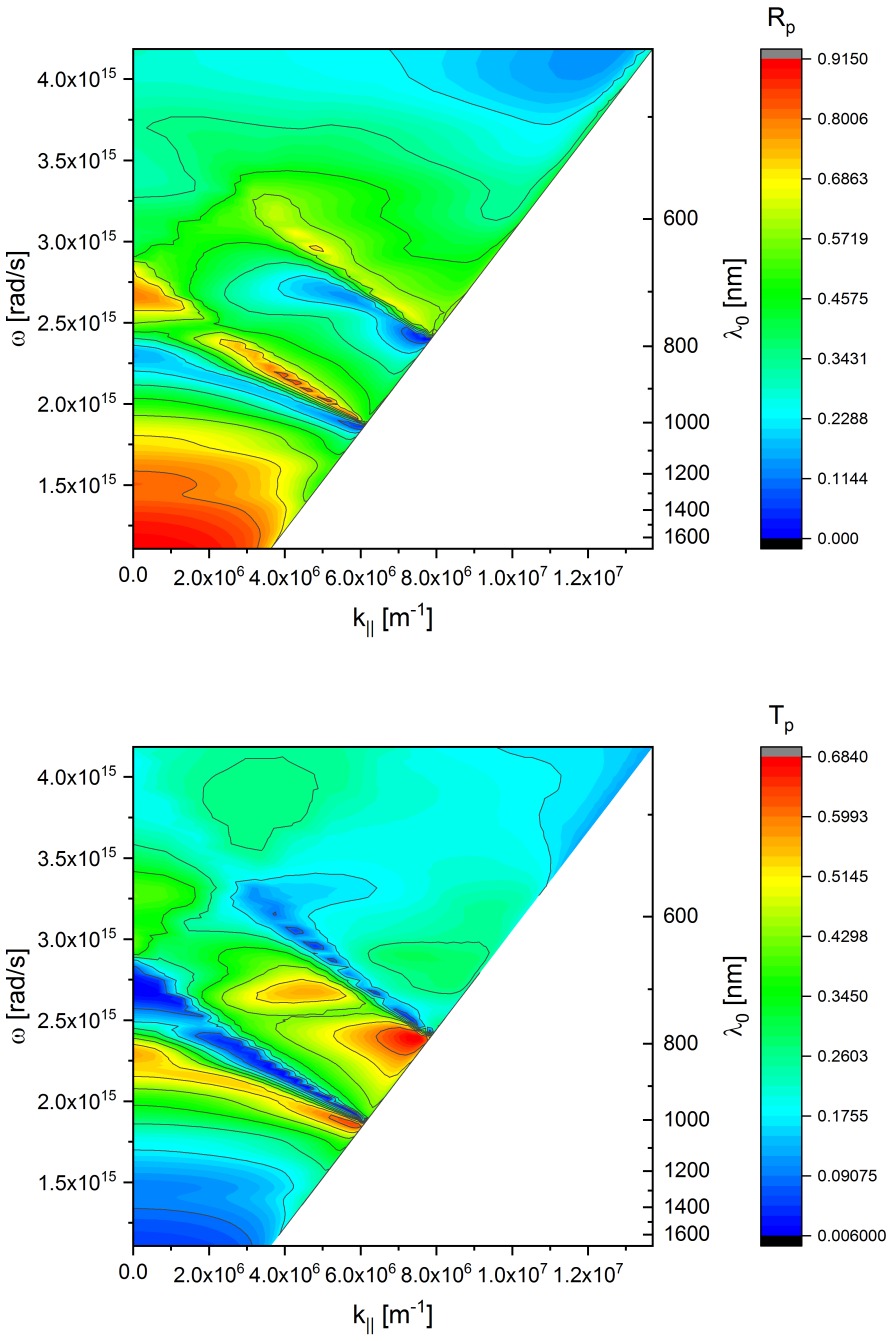

Figure 3.14: Reflectance and transmittance spectra simulated for p-polarized light impinging on a gold nanohole array with a thickness of 70 *nm*. The NHA is on a silica substrate.

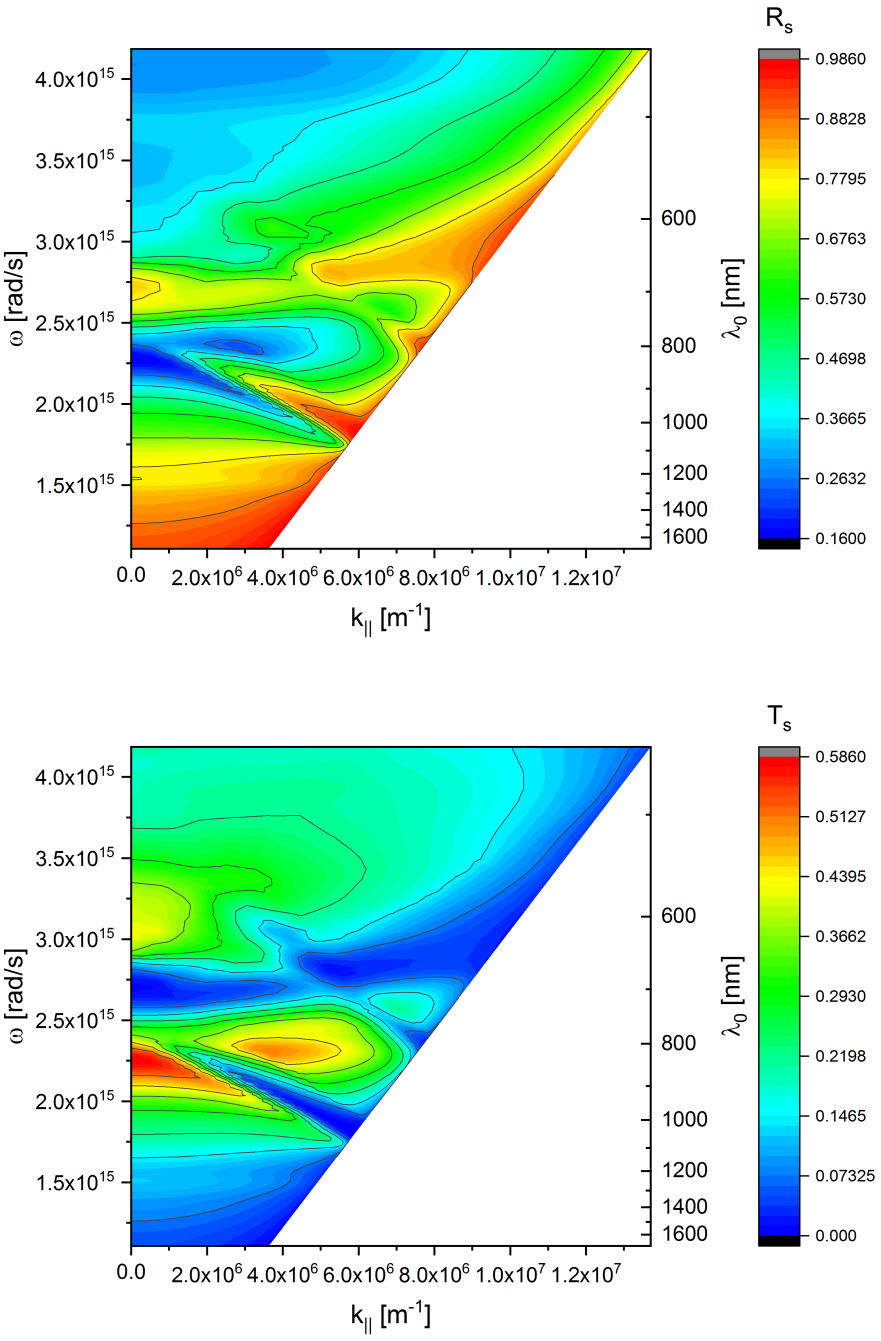

Figure 3.15: Reflectance and transmittance spectra simulated for s-polarized light impinging on a gold nanohole array with a thickness of 70 *nm*. The NHA is on a silica substrate.

That is, the points $(k_{\parallel}, \omega)$ along these bands satisfy the dispersion relation for a SPP, Eq. 1.75, with a wavector contribution from the lattice, Eq. 3.3, namely from first neighbour points.
The NHA acts firstly as a filter, allowing only the transmission of impinging light with (ω, k) values comprised in these bands. Furthermore, as light is transmitted on the other side of the NHA, at the interface with the underlying spacer it is scattered with different contributions of tangential wavevector, according to the scattering planes of the NHA.
Eventually, the NHA has been studied as a coupler for high-k modes for the thin systems discussed previously. In Figs. 3.16 the systems composed of a gold NHA separated by a 10 nm alumina spacer from a 180 nm thick effective medium with filling fraction equal to 33% has been simulated. Light is p-polarized and impinges on the system from air, whereas an optically thick substrate ($n_{sub} = 2.8$) has been chosen in order to decouple high-k modes. The presence of the hyperbolic medium underneath strongly modifies the overall reflectance spectrum, emphasizing the first minimum band and strongly quenching the second one. In the transmittance spectrum some regions of non-null values can be observed, with a peak of 10% in transmittance at high angle of incidence for 700 $nm < \lambda_0 < 800$ nm. In first approximation, this peak can be related to an effective horizontal shift in the $k_{\parallel} - \omega$ plane caused by the NHA periodicity, which enables to reach the region of high-k propagating modes found in Fig. 3.6.
A similar situation is found in the case of the NHA separated by a spacer from a 180 nm thick multilayer composed of alternating four 30 nm alumina with four 15 nm gold layers, see Figs. 3.17, which was simulated with the same boundary conditions. Similarly to prism-coupling simulations, the corresponding transmittance values are slightly lower.

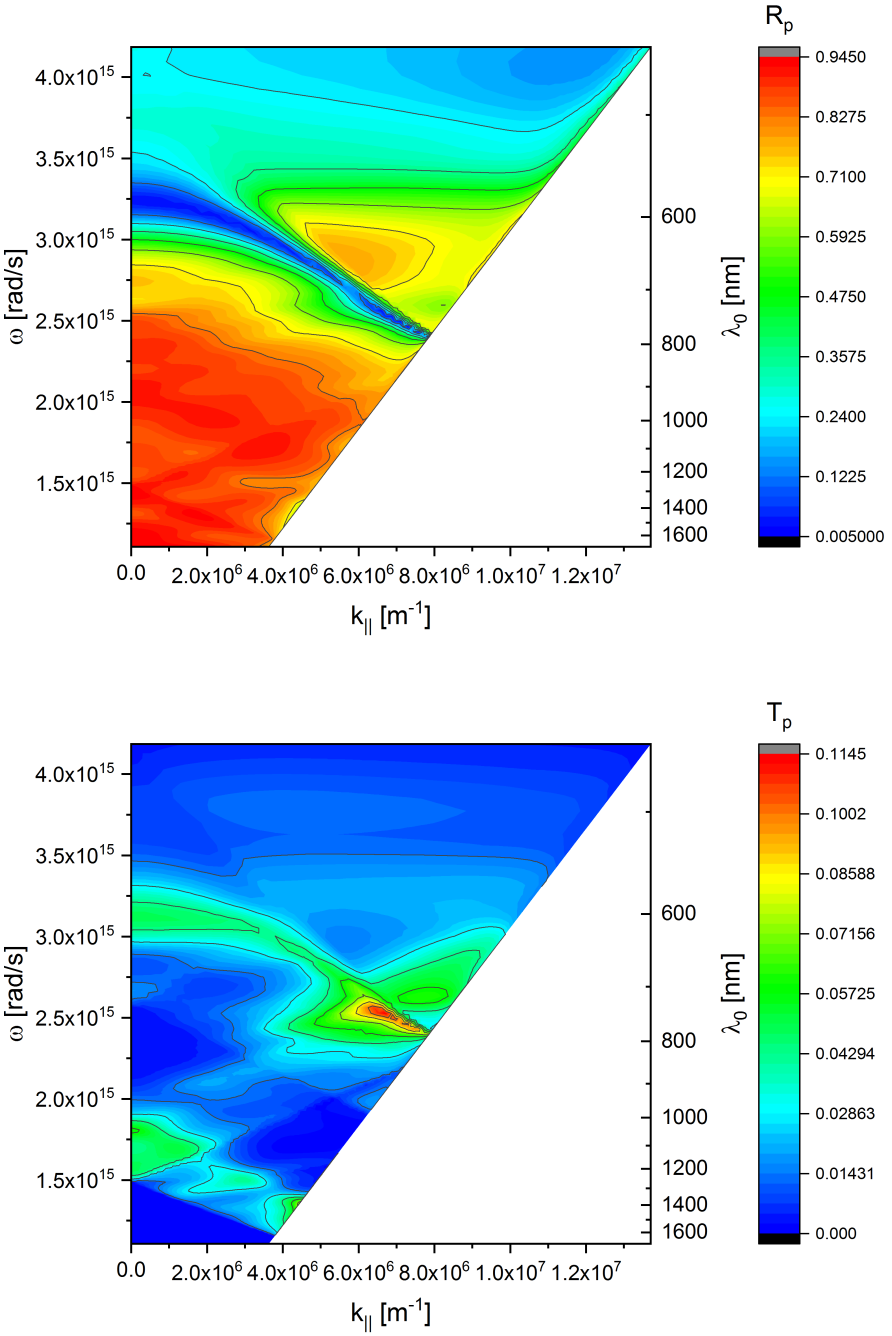

Figure 3.16: Reflectance and transmittance spectra simulated for p-polarized light impinging on a gold NHA, separated by a 10 nm alumina spacer from a 180 nm thick effective medium with filling fraction equal to 33%. Light impinges from air, while the substrate of the system has $n_{sub} = 2.8$

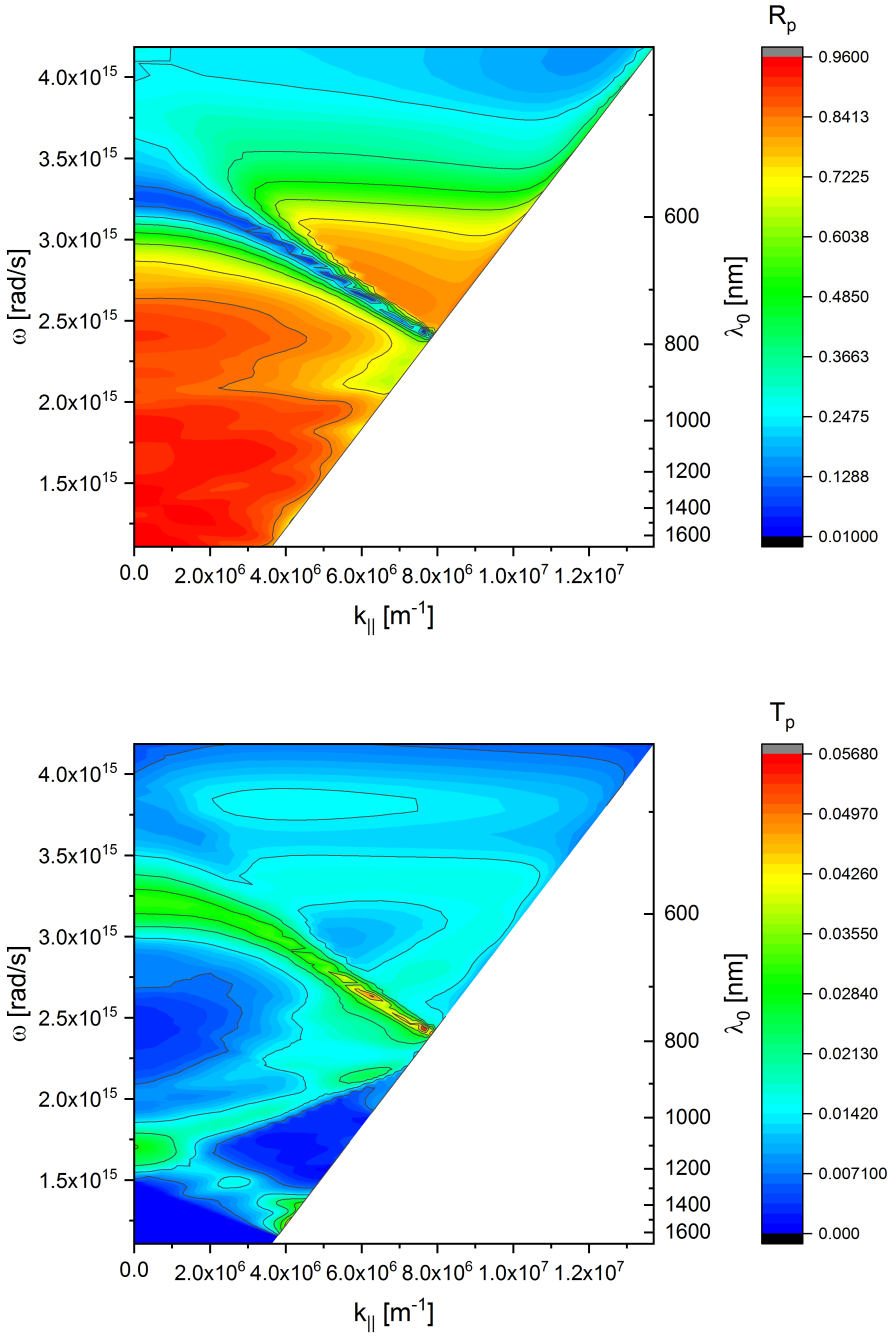

Figure 3.17: Reflectance and transmittance spectra simulated for p-polarized light impinging on a gold NHA, separated by a 10 nm alumina spacer from a 180 nm thick multilayer composed of alternating four 30 nm alumina with four 15 nm gold layers. Light impinges from air, while the substrate of the system has $n_{sub} = 2.8$

Chapter 4

Results: Experimental Measurements

4.1 Synthesis

The deposition of thin films and multilayers was realized on top of substrates having an area of approximately 2 $cm \times 2$ cm. The material of the substrate was either transparent highly-pure HSQ 300 silica (SiO_2), or opaque monocrystalline silicon (Si). The surface of each substrate was cleaned to remove external impurities, which otherwise would cause structural defects in the samples. The samples were cleand with a bath of 1 hour at $90°C$ in an *acid piranha* solution, which is made of sulfuric acid (H_2SO_4) and hydrogen peroxide (H_2O_2) in 3 : 1 proportion. This strong oxidizing solution helps removing most of the organic matter impurities from the substrate surface. After the treatment with the *acid piranha* solution, the samples were thoroughly rinsed with Milli-Q water before being mounted on the sample holder of the sputtering apparatus.

In order to fabricate thin films of controlled thickness, the sputtering rates of a gold target and of an alumina target were characterized. The calibration was performed depositing a few tens of nanometers of the chosen material on a substrate and measuring the thickness of the film by means of atomic force microscopy. The Au sputtering rate was ~ 10 nm/s, whereas the alumina sputtering rate for the alumina target was one order of magnitude slower, ~ 1 nm/s.

AFM scans were done on the surface of a 15 nm thick gold film and a 30 nm thick alumina film. These measurements showed that the average roughness of these layers was $R_a \lesssim 1$ nm. This result implies that at these thicknesses the sputtering process produces homogeneous layers without isolated islands of material.

Several multilayers made of alternating alumina and gold thin films were fabricated. In all multilayer samples, the deposition started with the deposition of an alumina layer, in order to obtain a good adhesion with the substrate. The deposition continued alternating alumina layers with gold layers, having in total four metal layers with thickness t_m and four dielectric layers with thickness t_d. On top of each multilayer an additional alumina layer with thickness t_s was deposited, to seperate the underlying multilayer from additional structures, like nanohole arrays, or layers doped with emitters. Therefore, each multilayer

consisted of four couples of alumina and gold, plus an alumina spacer. The thickness t_m of the four gold layers was kept constant in all the samples, whereas the thickness of the inner alumina layers and of the spacer were changed to obtain multilayers with different metallic filling fraction. The notation $(t_d/t_m) \times 4 + t_s$ will then be used to indicate the fabricated multilayers, with the unit nm implicit. Keeping conceptually separated the underlying multilayer from the spacer on top of it, the metallic filling fraction attributed to each sample was computed as simply $FF = t_m/(t_m + t_d)$.
The fabricated samples consisted of the following multilayers:

- $(30/15) \times 4 + 30$, with $FF = 33\%$
- $(60/15) \times 4 + 60$, with $FF = 20\%$
- $(30/15) \times 4 + 10$, with $FF = 33\%$
- $(80/15) \times 4 + 10$, with $FF = 16\%$

In all the samples the average roughness measured on the last surface was found to be of the order of 1 nm or less, which is comparable with the value found from a single layer deposition. Therefore, the deposition process of alternating metal and dielectric nanometer layers did not cause significant defects in the multilayer structure. In addition to these multilayer samples, other reference samples were sputtered as well; for example, bilayers of gold and alumina with varying thickness were realized to compare the optical behaviour of a bilayer with that of the corresponding multilayer.

4.2 Structural characterization

Several techniques were employed to study the structural and optical properties of each multilayer.

4.2.1 SEM and AFM measurements

Measurements with the scanning electron microscope allowed us to observe the multilayer samples in cross-section, that is, from the side of the multilayer. Collecting the scattered electrons, which depend on the atomic species hit by the electron beam, it was possible to distinguish the different materials of adjacent layers and to measure their thicknesses accordingly. To acquire this image, a sample fabricated on silicon is cleaved with the point of a tweezer, to expose an inner section of the sample. Since the samples contain both metallic and dielectric layers which get hit by charged electrons, special care must be taken with the dissipation of the accumulated electrostatic charge which reduces the instrument resolution. To facilitate charge dissipation, a thin film of carbon was deposited on the cleaved side of the sample, by means of evaporation. In Fig. 4.1 it is shown a cross-sectional SEM image of the $(30/15) \times 4 + 30$ multilayer sample, deposited on Si. The white stripes correspond to the gold thin films, whereas alumina layers appear light gray.

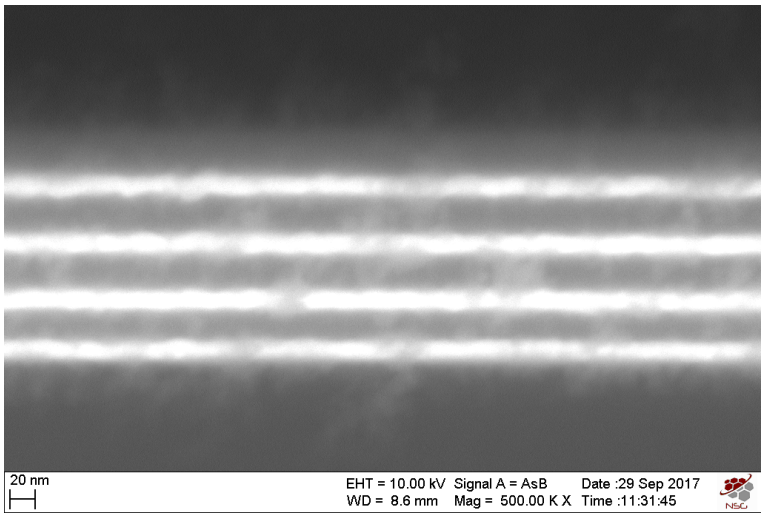

Figure 4.1: Cross-sectional SEM image of the $(30/15)\times 4+30$ multilayer sample. The sample was positioned with the substrate at the bottom of the image.

The sample was positioned with the substrate at the bottom of the image. Because of low atomic number contrast between Al and Si, the first alumina layer starting from the bottom is difficult to distinguish from the Si substrate. In Table 4.1 the values measured for the four multilayer samples are shown. The average thickness of each type of layer is shown, with the error computed as the semidispersion of all the layers. In all the cases, the measured thicknesses are consistent with the nominal values, and the semidispersion for each type of layer is within 5 nm.

Table 4.1: Thicknesses of gold and alumina layers measured on the multilayer samples with the scanning electron microscope. Indicated uncertainties are calculated as the semidispersion of the thickness on the set of layers of the same type.

Multilayer sample	t_{Au}	$t_{Al_2O_3}$	t_{spacer}
$(30/15)\times 4+30$	$(16\pm 1)\ nm$	$(30\pm 4)\ nm$	$(34\pm 1)\ nm$
$(60/15)\times 4+60$	$(17\pm 3)\ nm$	$(61\pm 5)\ nm$	$(64\pm 1)\ nm$
$(30/15)\times 4+10$	$(14\pm 2)\ nm$	$(27\pm 3)\ nm$	$(11\pm 1)\ nm$
$(80/15)\times 4+10$	$(15\pm 1)\ nm$	$(84\pm 4)\ nm$	$(12\pm 1)\ nm$

The atomic force microscope was also used to measure the overall thickness of multilayer samples. To perform these measurements, an additional substrate with a marker sign on it was added into each sputtering session. The sample was then put in a bath of acetone and the removal of the marker was accelerated by means of ultrasounds. It is worth noting that this process not only removes the marker, but damages the multilayer as well, even with a few seconds of ultrasound treatment. Therefore, the resulting border between the top of multilayer and the exposed substrate is not abrupt; instead, several steps can be observed, corresponging to the inner layers of the structure. This complicates the measurement of the total thickness, as the AFM is unable to maintain a straight line over distances longer

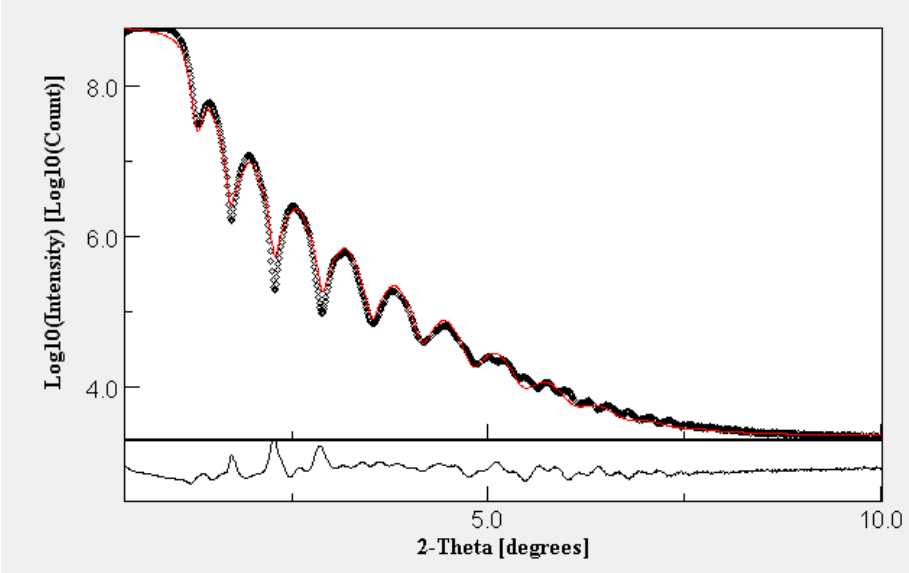

Figure 4.2: X-ray reflectivity spectrum of a bilayer on Si, composed of a 30 nm layer of alumina and a 15 nm layer of gold, with the gold layer facing outwards. The best fit curve is drawn in red.

than 10 μm. The thicknesses measured on the multilayer samples are shown in Table 4.2.

Table 4.2: Total thicknesses of multilayer samples and average roughnesses on their top surface, measured at the atomic force microscope. Indicated uncertainties are estimates of the error given by the apparatus.

Multilayer sample	Exp. t_{ML}	Nom. t_{ML}	R_{ave}
$(30/15) \times 4 + 30$	(220 ± 5) nm	210 nm	0.3 nm
$(60/15) \times 4 + 60$	(320 ± 5) nm	360 nm	0.2 nm
$(30/15) \times 4 + 10$	(180 ± 5) nm	190 nm	0.5 nm
$(80/15) \times 4 + 10$	(370 ± 5) nm	390 nm	0.2 nm

4.2.2 X-ray reflectivity spectra

Two samples were analyzed with the technique of X-ray reflectivity, namely

- the $(30/15) \times 4 + 30$ multilayer sample, deposited on Si.
- a bilayer with a 30 nm alumina layer at the bottom and a 15 nm gold layer on top, deposited on a Si substrate;

The bilayer was studied since it represents the unit cell of the multilayer sample. The reflectivity spectrum for the bilayer is shown in Fig. 4.2, in which the measured data are plotted in black, while the best fit curve is drawn in red. Data are plotted with respect to the detector angle 2θ. The reflectivity was measured up to a grazing incidence angle $2\theta = 14°$, but for $2\theta > 10°$ no reflectivity oscillations can be discerned. The simulated

spectrum depends on the characteristics of the thin films, namely their thickness, their refractive index, and the roughness at the interfaces. It is worth considering the values known in the literature [38] for the refractive indices of gold and alumina; using the notation $n = 1 - \delta + i\beta$ for the refractive index at X-ray energies, the corresponding terms for the two bulk materials are shown in Table 4.3

Table 4.3: Components of the refractive index ($n = 1 - \delta + i\beta$) for bulk gold and alumina in the literature [38].

	δ	β
Gold bulk	$4.72 \cdot 10^{-5}$	$4.87 \cdot 10^{-6}$
Alumina bulk	$1.24 \cdot 10^{-5}$	$1.41 \cdot 10^{-7}$

In the analysis of X-ray reflectance data acquired on the bilayer sample, low sensitivity to the components of the refractive index of alumina was found. These quantities were then fixed to the bulk values from the literature. In this way, it was possible to determine the thicknesses t and the interface roughnesses r as best fit parameters, as well as the refractive index of the gold thin film, as shown in Table 4.4.

Table 4.4: Results of the best fit analysis done on X-ray reflectance data from the bilayer sample.

Gold	$t = (13.2 \pm 0.1)\ nm$
	$\delta = (4.51 \pm 0.01) \cdot 10^{-5}$
	$\beta = (2.3 \pm 0.1) \cdot 10^{-6}$
	$r = (0.4 \pm 0.1)\ nm$
Alumina	$t = (28.0 \pm 0.1)\ nm$
	$r = (0.6 \pm 0.1)\ nm$

The second sample was the $(30/15) \times 4 + 30$ multilayer sample, deposited on Si. Therefore, it had gold and alumina layers with the same nominal thickness as the previous sample, but with an alumina layer on top. Its reflectivity spectrum is shown in Fig. 4.3, together with the best fit curve. The spectrum has narrower angular peaks, due to the periodical repetition through space of the $\sim 45\ nm$ bilayer. Since $\delta_{Al_2O_3} < \delta_{Au}$, the real component of the refractive index of alumina is closer to 1. Therefore, the critical grazing incidence angle for alumina is expected to be lower than the critical angle for gold, being $\theta_c^{(Al_2O_3)} = 0.29°$ and $\theta_c^{(Au)} = 0.56°$. Since on top of the multilayer there is an alumina layer deposited on a gold layer, it follows that for $\theta_c^{(Al_2O_3)} < \theta < \theta_c^{(Au)} = 0.56°$ the X-ray photons can pass through the alumina layer but are totally reflected by gold. Up to $\theta_c^{(Au)}$ the reflectivity spectrum is then the same one would obtain from an alumina layer deposited on a gold substrate. The interference pattern due to the whole multilayer is observed in the graph only for $2\theta > 1.12°$. The number of free parameters in the multilayer sample grows with the number of layers, making it difficult to fit them separately, since they have a high degree of correlation. On the other hand, a model with all layers of the same material having

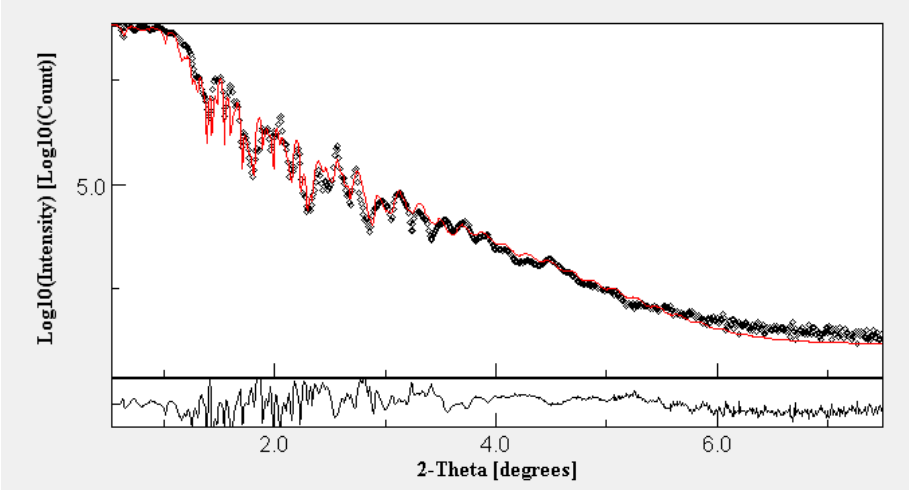

Figure 4.3: X-ray reflectivity spectrum of the $(30/15) \times 4 + 30$ multilayer sample, deposited on Si. The best fit curve is drawn in red.

the same characteristics leads to an inadequate fit. A compromise has been evaluated, starting with same initial conditions for all the layers of the same type. The thickness and roughness of each layer was then set as a free parameter, whereas the refractive index of each layer was set equal to the value found in the bilayer study. Eventually, the best fit curve for the reflectivity shown in Fig. 4.3 was obtained. The general trend is reproduced, but the model follows poorly the finer details of the spectrum. The average thickness of the gold layers results to be equal to 16 nm, with a semidispersion of 4 nm, whereas the average thickness of the alumina layers is 29 nm with a semidispersion of 4 nm. The roughnesses of all the layers are on the order of $1 \div 2$ nm.
The results show that X-ray reflectivity can be used to obtain information on the structural characteristics of the multilayer, as these values are coherent with the results of other techniques. The analysis could be improved by examining first the smallest elements of the multilayer, that is, a single gold thin film and a single alumina thin film. In addition, the effects due to the periodic repetition of a bilayer throughout the multilayer could be studied by examining intermediate structures with a varying number of bilayers.

4.3 Optical characterization

4.3.1 Characterization of thin films

A full characterization of thin film samples is propaedeutic to the subsequent analysis of multilayers. This is true especially when one works with nanostructured metals, whose permittivity can differ strongly from the values of the bulk material. Henceforth, a few samples consisting in thin films of gold and alumina were initially synthesized by means of magnetron sputtering, and were subsequently analyzed by AFM and the ellipsometry techniques.
The optical response of a thin film at each wavelength depends on its dielectric functions at

that wavelength, and on its thickness. For a dispersive material with a complex dielectric function, two independent parameters (the real and imaginary components) must be fitted at each wavelength, together with the thickness. Intuitively, an ellipsometry scan measures only two independent parameters (Ψ and Δ) at each wavelength, so it is not sufficient to find all the required parameters. Additionally, the dielectric functions and the thickness of a layer are highly correlated parameters. Another measurement, independent from the ellipsometric scan, is thus required to obtain the parameters of interest without ambiguity. If the sample has a transparent substrate (e.g. SiO_2, or SLG), additional data can be obtained measuring the transmittance of the sample at normal incidence. In this way one can fully characterize the thin film sample using the ellipsometer, which is able to perform both ellipsometric and transmittance measurements. Otherwise, the thickness of the thin film can be directly measured with the AFM.

In the analysis of the dielectric functions of thin films, the permittivities of the bulk materials were used as starting values for the fit procedure, and small corrections were obtained for thin films. Since a point-by-point fit of the dielectric functions results in data which are noisy and in general do not satisfy the Kramers-Kronig condition, parametric dielectric functions were used in the analysis of ellipsometric measurements. This approach has also the benefit of reducing the number of fundamental parameters.

To measure the dielectric functions of gold films, a thin film with nominal thickness of 15 nm was deposited on a SiO_2 substrate. Transmittance and ellipsometric measurements were conducted, and it was possible to fit both the dielectric functions and the thickness with a total $MSE = 3$. The measured thickness was (15.3±0.1) nm, in agreement with the nominal one. The dielectric functions were fitted with a Drude-Lorentz dielectric function (see Eq. (1.30)), with five peaks centered at the energies $E = 0.16\ eV$, $2.8\ eV$, $3.3\ eV$, $3.4\ eV$, and $4.2\ eV$. The obtained dielectric functions are shown in Fig. (4.4a) and (4.4b), where they are compared with typical values for bulk gold samples [34]. The thin film sample is characterized by a higher absorption with respect to the bulk sample, which is a common result for nanostructured metals.

An alumina thin film with nominal thickness of 30 nm was also deposited on a silicon wafer, and a thickness of $(28.7 \pm 1)\ nm$ was obtained by AFM. The analysis of the ellipsometric measurements showed that the absorption of alumina can be safely neglected even for nanometric thin layers. Therefore, a simple Cauchy dispersion function was used to fit the real part of the refractive index,

$$n(\lambda) = A + \frac{B}{\lambda^2} + \frac{C}{\lambda^4}. \tag{4.1}$$

The best fit values of the parameters (with $MSE = 1.2$) were $A = 1.64 \pm 0.01$, $B = (-0.003 \pm 0.001)\ nm^2$, and $C = (9 \pm 1) \cdot 10^{-4}\ nm^4$. The obtained real permittivity is shown in Fig. (4.5), where it is compared with values for bulk alumina [35]. The bulk values refer to $\alpha - Al_2O_3$, or corundum, which is the most common form of alumina found in nature. The crystalline structure of the alumina thin films was not examined as it was beyond the scope of this study, but one can safely assume assume that the sputtering

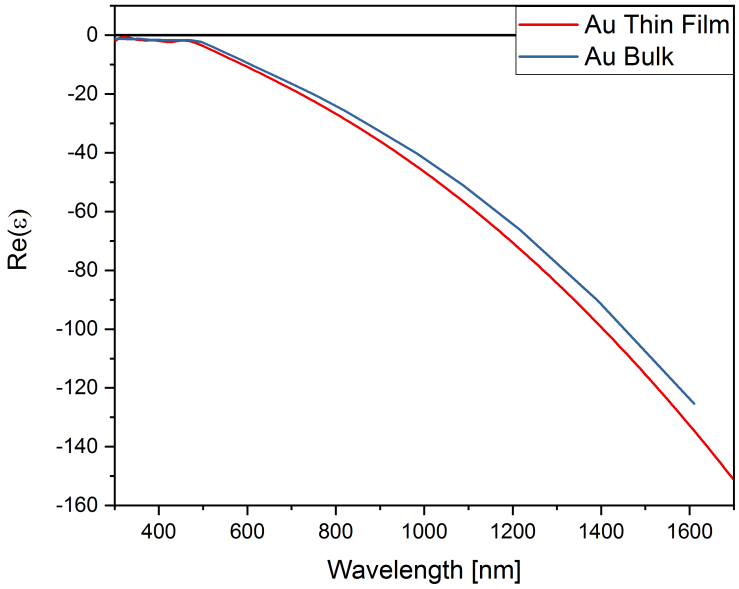

(a)

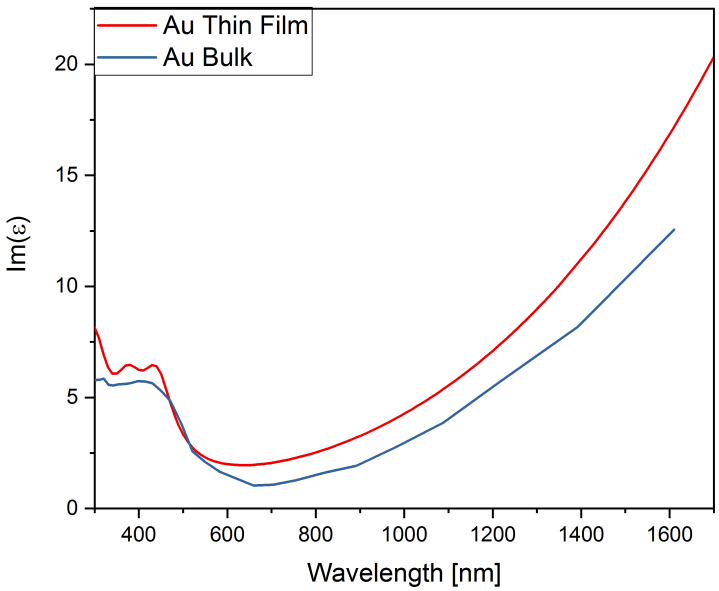

(b)

Figure 4.4: Real part (a) and imaginary part (b) of the dielectric function of gold: comparison between a thin film with thickness of $\sim 15\ nm$ and a bulk sample measured by Johnson and Christy [34].

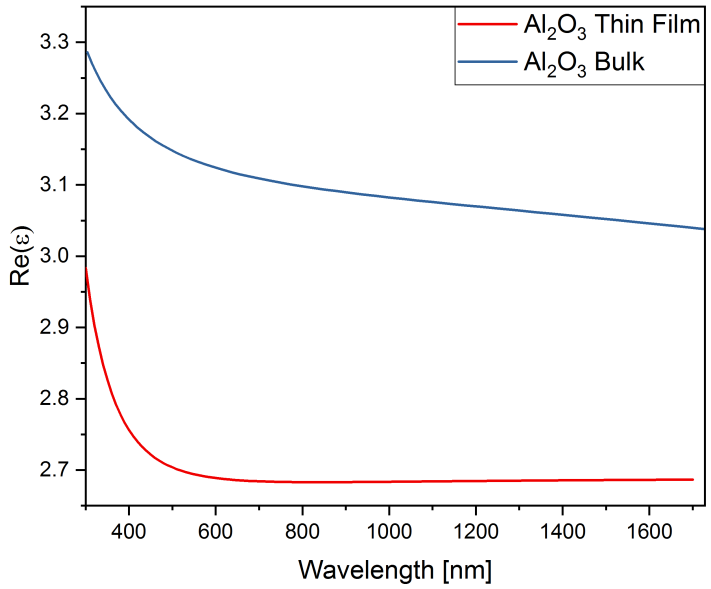

Figure 4.5: Real part of the dielectric function of alumina: comparison between a thin film with thickness of $\sim 30\ nm$ and a bulk sample measured by I. H. Malitson and M. J. Dodge [35].

process produces amorphous alumina.

4.3.2 Optical characterization of multilayers

The $(30/15)\times 4+30$, with $FF = 33\%$ multilayer sample, fabricated on a SiO_2 substrate, was first analyzed with ellipsometric measurements. To evaluate the properties of the sample from a general point of view, anisotropic ellipsometry data were first acquired to look for cross-polarization effects. Indicating with ρ_{xy} the complex reflectance for impinging light of polarization x which gets reflected into light of polarization y, one defines the ellipsometric parameters

$$\begin{cases} AnE = \rho_{pp}/\rho_{ss} \\ A_{sp} = \rho_{sp}/\rho_{ss} \\ A_{ps} = \rho_{ps}/\rho_{pp} \end{cases} \tag{4.2}$$

where AnE corresponds to the standard ellipsometric parameter. With these parameters, one can characterize a sample in terms of its Jones matrix:

$$J = \rho_{ss} \begin{pmatrix} AnE & A_{sp} \\ A_{ps} \times AnE & 1 \end{pmatrix} \tag{4.3}$$

Measurements conducted on the sample (for $\theta = 65°, 70°, 75°$ and $300\ nm < \lambda < 1700\ nm$) showed that the non-diagonal components are null for all the observed wavelengths within the experimental error. Therefore, no cross-polarization effects are observed. This result is compatible either with an isotropic sample, or with an anisotropic uniaxial sample whose

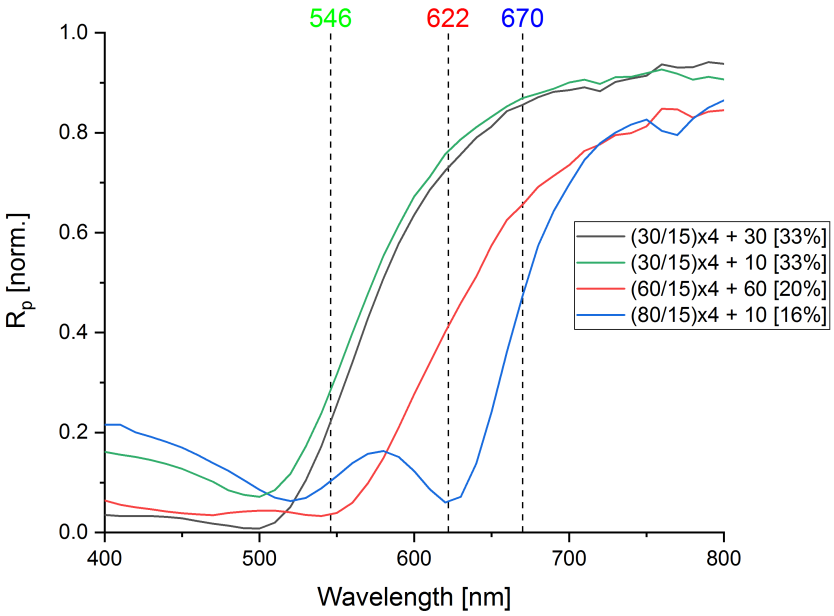

Figure 4.6: Reflectance spectra of the multilayer samples acquired at $\theta = 15°$ with p-polarized light. The vertical dashed lines indicate the ENZ wavelengths for effective media with filling fraction equal to 33%, 20%, and 16%, from left to right.

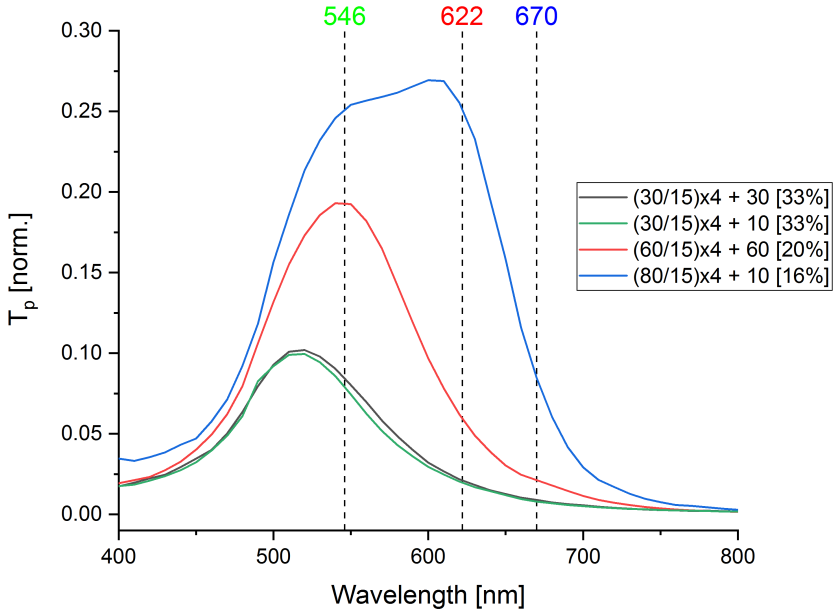

Figure 4.7: Transmittance spectra of the multilayer samples acquired at $\theta = 0°$ with p-polarized light. The vertical dashed lines indicate the ENZ wavelengths for effective media with filling fraction equal to 33%, 20%, and 16%, from left to right.

optical axis is perpendicular to the surface normal [39]. To fully characterize the optical response of the sample, also specular reflectance data $\theta = 15°, 25°, 35°, 45°, 55°$ and straight transmittance data at $\theta = 0$ were collected for p- and s-polarized light. Ellipsometric, reflectance, and transmittance measurements were analyzed by comparing the experimental data with the predictions of carefully chosen models. In Figs. 4.6 and 4.7 the reflectance spectra at $\theta = 15°$ and the transmittance spectra at $\theta = 0°$ of the multilayer samples at p-polarized light are shown. The vertical dashed lines indicate the ENZ wavelengths for effective media with different filling fractions: from left to right, at 33%, at 20%, and at 16%. The ENZ wavelength increases for decreasing filling fraction, as seen in Fig. 3.5. Although the multilayers have the same equivalent thickness of gold, their reflectance and transmittance spectra are strongly dependent on the metallic filling fraction with respect to the dielectric. Namely, in the transmittance spectra it affects the peak position of maximum transmittance, and its height, whereas in the reflectance spectra it changes the range in which the reflectance varies from low dielectric-like values to high values typical of metals.

As a starting point, the multilayer samples were modeled faithfully as a stack of layers, using the experimental dielectric functions for the thin films. A best fitting procedure was implemented with the layer thicknesses as parameters, using the nominal thicknesses as starting values. Fitting each layer thickness as an independent parameter can lead to unphysical results; furthermore, it shows that the sensitivity of this technique on the layers' thickness decreases for deeper layers. In order to reduce the number of free parameters, layers of the same material were assumed to have equal thicknesses. In fact, the sputtering process during the fabrication of the multilayer is carried on in the same way for each layer of the same material. The obtained results are shown in Table 4.5.

Table 4.5: Thicknesses of gold and alumina layers in multilayer samples obtained with measurements at the variable angle spectroscopic ellipsometer. Thicknesses of layers of the same type in a multilayer were set equal to each other. In the first two samples, the thickness of the alumina spacer was set equal to the thicknesses of the alumina layers inside the multilayers, whereas in the other two samples it was considered as a free parameter.

Multilayer sample	t_{Au}	$t_{Al_2O_3}$	t_{spacer}	MSE
$(30/15) \times 4 + 30$	$(15.1 \pm 0.1)\ nm$	$(32.7 \pm 0.2)\ nm$	$(32.7 \pm 0.2)\ nm$	2.0
$(60/15) \times 4 + 60$	$(16.6 \pm 0.1)\ nm$	$(65.8 \pm 0.3)\ nm$	$(65.8 \pm 0.3)\ nm$	1.2
$(30/15) \times 4 + 10$	$(15.2 \pm 0.1)\ nm$	$(38.1 \pm 0.4)\ nm$	$(10.6 \pm 0.4)\ nm$	0.9
$(80/15) \times 4 + 10$	$(15.2 \pm 0.2)\ nm$	$(82.2 \pm 0.6)\ nm$	$(13.4 \pm 0.8)\ nm$	2.2

The fit converges with a low MSE value, and the obtained values of the thin film thicknesses are coherent with values found with other methods, within experimental error.

The experimental measurements were then compared with simulation results for an homogeneous effective medium. Each sample was modeled as a homogeneous uniaxial layer, with $\varepsilon_x = \varepsilon_y = \varepsilon_\parallel \neq \varepsilon_z = \varepsilon_\perp$, and with an alumina spacer on top of it. The principal components of the uniaxial layer were expressed in terms of the effective medium formulas, see

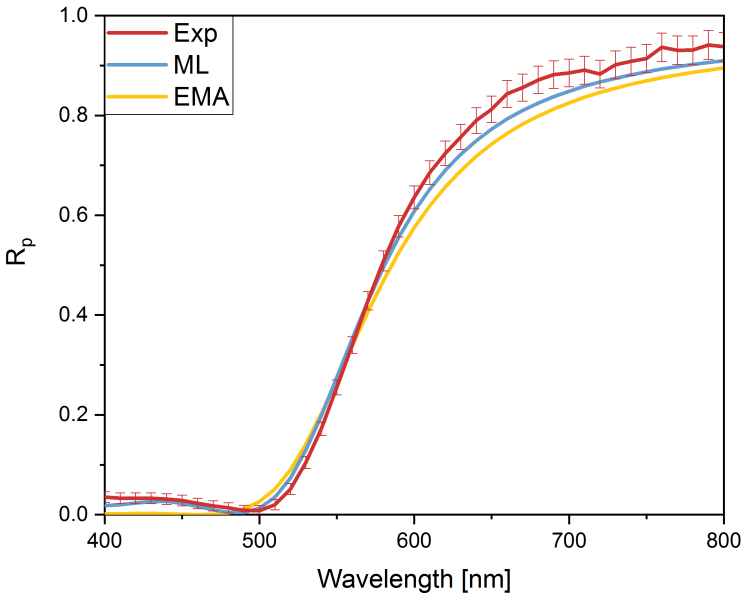

Figure 4.8: Reflectance spectra of the $(30/15) \times 4 + 30$ multilayer sample for p-polarized light at $\theta = 15°$: comparison between experimental measurement (Exp), best fit curve with the multilayer model (ML), and best fit curve with effective medium model (EMA).

Eqs. 1.57 and 1.61, with the metallic filling fraction of the multilayer as a free parameter. The thicknesses of the effective medium and the spacer were fixed to values measured by SEM.

Table 4.6: Fitting results of ellipsometry measurements compared with a model having an effective medium uniaxial layer on a silica substrate, with an alumina spacer on top of the layer. The principal components are given by the combination of gold and alumina permittivities, with the metallic filling fraction as free parameter.

Multilayer sample	Exp. FF	Nomin. FF	MSE
$(30/15) \times 4 + 30$	(32.9 ± 0.1) %	33%	3.0
$(60/15) \times 4 + 60$	(18.6 ± 0.2) %	20%	3.4
$(30/15) \times 4 + 10$	(32.0 ± 0.2) %	33%	3.2
$(80/15) \times 4 + 10$	(15.1 ± 0.2) %	16%	8.3

Obtained values for the filling fraction are reasonably close to nominal values, and with a low MSE value for the first three multilayers. It is worth noting that the higher MSE value is obtained in the analysis of the $(80/15) \times 4 + 10$ multilayer. In fact, this sample has the period with the highest thickness ($\Lambda \sim 100\ nm$), thus making it the multilayer for which the effective medium approximation is less valid.

In Fig. 4.8 the experimental reflectance spectrum of the $(30/15) \times 4 + 30$ multilayer sample for p-polarized light at $\theta = 15°$ is shown in comparison with the corresponding

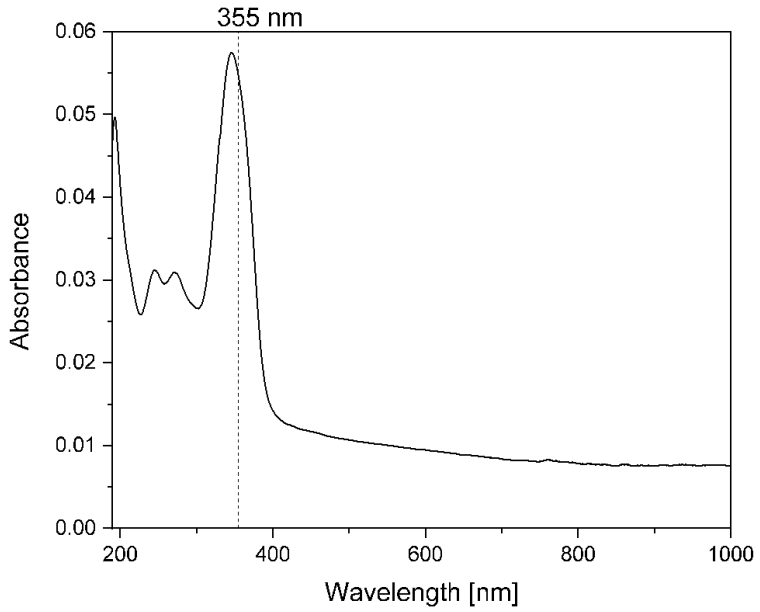

Figure 4.9: Absorption spectrum of EuTTA. The absorption peak is at 346 nm, close to 355 nm, which is the excitation wavelength used to excite the samples. The spectrum was obtained by using as a baseline another sample consisting of an undoped PMMA layer on top of silica.

best fit curves obtained with the multilayer and the effective medium models. Both models reproduce adequately the spectrum.

4.4 Photoluminescence measurements

The europium(III) thenoyltrifluoroacetonate complex (EuTTA) was chosen as a probe for the photoluminescence measurements. In the complex, the ion Eu^{3+} is responsible for the characteristic emission spectrum, whereas the organic complex around gives stability to the compound. A film of polymethylmethacrylate (PMMA) doped with EuTTA was deposited on top of each sample. To fabricate these layers, a 6 mM solution of EuTTA (Acros Organics) dissolved in toluene was first prepared. In parallel, a solution of 2 % w/w PMMA in toluene was made. Both solutions were kept at $75°C$ to ensure that all the solute was dissolved. Eventually, equal parts of the two solutions were mixed together, to obtain a solution of 3 mM EuTTA and 1 % PMMA in toluene, which was kept at $75°C$ as well. A volume of 100 μL of this solution was deposited on each sample and subsequently spin-coated for 60 s at 3000 RPM and for 10 s at 5000 RPM. In order to carry on this procedure, the external surface of each sample was first made to be hydrophilic by exposing it to UV radiation. The thickness of the PMMA layers fabricated with this procedure was measured with the AFM, and was found to be between 30 nm and 50 nm.
EuTTA-doped PMMA layers were first realized on top of a silica substrate and a silicon

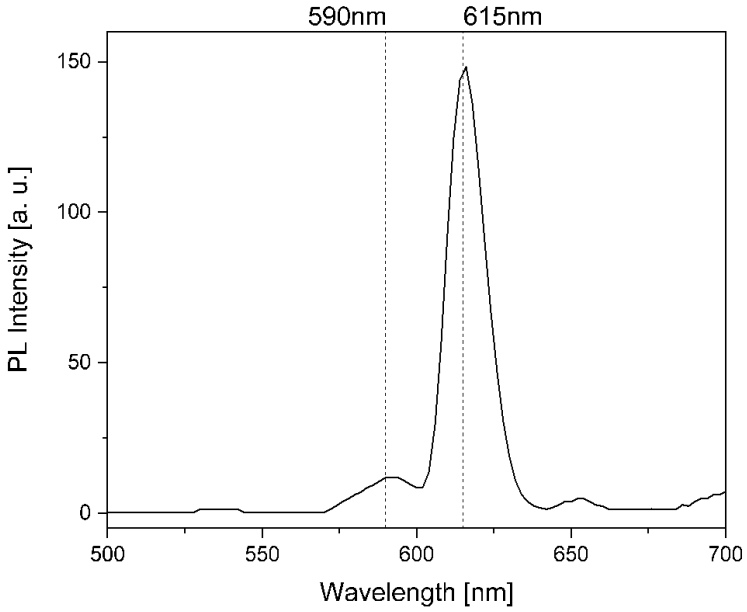

Figure 4.10: Emission spectrum of EuTTA. The main peak of emission is at $\lambda = 615\ nm$, with a $FWHM$ of approximately 10 nm.

substrate, in order to characterize the absorption and emission properties of the emitters, independently from the underlying substrate. The absorption spectrum is shown in Fig. 4.9. When Eu^{3+} is excited with UV radiation (355 nm), it produces at room temperature the emission spectrum shown in Fig. 4.10. A main peak with stable emission is observed at $\lambda \sim 615\ nm$.

In Fig. 4.11 the temporal decay curve measured from the sample with EuTTA-doped PMMA layer on silica is shown, as an example of the data acquired. The decay curves were fitted to extract the corresponding lifetimes. Convolution with the detector response can cause the curve to differ from a single exponential decay. To account for these discrepancies a stretched exponential function was used,

$$y(t) = A\ exp\left[-\left(\frac{t}{\tau}\right)^{k}\right], \tag{4.4}$$

where $0 < k < 1$ is the stretching parameter, and the effective lifetime is given by $\tau_{eff} = \frac{\tau}{k}\Gamma\left(\frac{1}{k}\right)$, where $\Gamma(x)$ is the Gamma function. For each sample, a decay curve was acquired with the laser beam impinging on five different points. Each curve was then fitted with a stretched exponential function, and the effective lifetime of the sample was computed as the average of the lifetimes of the five measurements. The semidispersions for these sets of data are used as estimates of the experimental errors. In the following table, the values of the PL decay time and the thickness of the PMMA layers on top of the two substrates are reported:

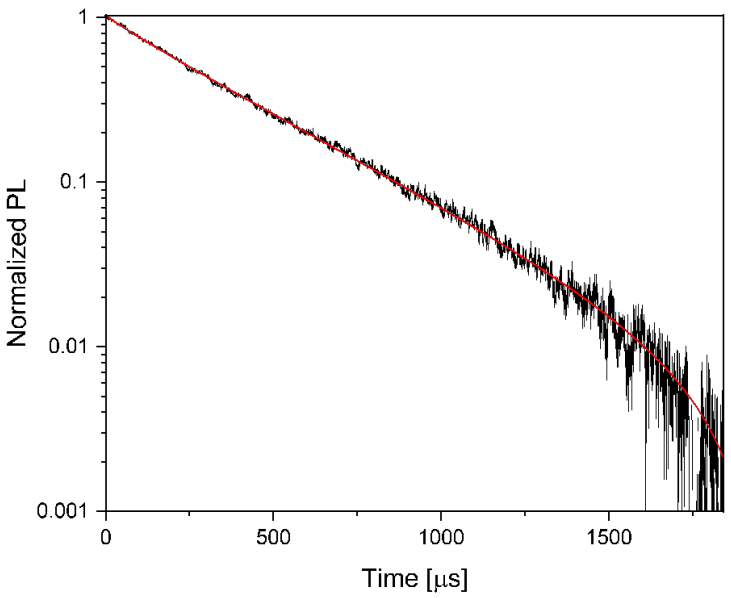

Figure 4.11: Temporal decay curve of EuTTA doped PMMA layers realized on top of a SiO_2 substrate, for emission at $\lambda_{exc} = 355\ nm$, and emission at $\lambda_{em} = 615\ nm$.

substrate	$\tau_{eff}\ [\mu s]$	$t_{PMMA}[nm]$
Si	273 ± 2	34 ± 5
SiO_2	358 ± 2	30 ± 5

A variation of the lifetime is observed, depending on the substrate. This effect can be attributed to the influence of both the air-PMMA and the PMMA-substrate interfaces. Since the thickness of the PMMA layer is nanometric, the emitters embedded in this layer are placed at a small distance from both interfaces, and their decay rate $\Gamma = \tau^{-1}$ is affected by reflection and absorption at each interface. This can be expressed as a variation of the emitters' radiative decay rate from its intrinsic value Γ_r^0, because of new radiative and nonradiative decay routes. This effect is usually expressed in terms of a multiplicative factor f, which depends on the permittivities of the materials in contact with the PMMA layer, and on the thickness of the PMMA layer itself. In this way, the total decay rate is the sum of the nonradiative decay rate and the modified radiative decay rate

$$\Gamma^i = \Gamma_{nr}^0 + \Gamma_r^0 f^i. \tag{4.5}$$

where the superscript i refers to the particular substrate. To calculate the effect of the interfaces, a model describing the emitters in terms of dipoles (CPS model) was implemented [24]. Values of $f^{Si} \sim 1.6$ and $f^{SiO_2} \sim 0.76$ are found for the two samples. Solving the system of two equations (4.5) for the two samples, the nonradiative decay rate and the intrinsic radiative decay rate are found to be $\Gamma_{nr} = (2.0 \pm 0.1) \cdot 10^3\ s^{-1}$ and $\Gamma_r^0 = (1.0 \pm 0.1) \cdot 10^3\ s^{-1}$.

Subsequently, a set of different samples has been studied with this technique, to investigate the effect of different substrates on the emitters' lifetime. The studied samples (fabricated on silica) were:

- 105 nm thick alumina layer
- 50/150 nm gold/alumina bilayer
- 50/10 nm gold/alumina bilayer
- $(30/15) \times 4 + 30$ multilayer sample
- $(60/15) \times 4 + 60$ multilayer sample
- $(30/15) \times 4 + 10$ multilayer sample
- $(80/15) \times 4 + 10$ multilayer sample

According to the effective medium approximation (see Fig. 3.2) at $\lambda_{em} = 615\ nm$, the multilayers $(30/15) \times 4 + 30$ and $(30/15) \times 4 + 10$ are expected to behave as hyperbolic media, whereas the multilayers $(60/15) \times 4 + 60$ and $(80/15) \times 4 + 10$ should be in the elliptical regime.
In Table 4.7 data for all the samples are shown by listing the samples in decreasing order with respect to the measured lifetime. The effective decay lifetimes τ_{eff}, the values for the stretching parameter k, and the amplitude A of the emission signals are reported.

Table 4.7: Fit result of PL measurements for all samples.

type	sample	τ_{eff} $[\mu s]$	k	A $[mV]$
Dielectric	105 nm alumina	336 ± 1	0.92	19.6
Bilayers	50/150 gold/alumina	375 ± 1	0.88	7.7
	50/10 gold/alumina	227 ± 1	0.92	112.4
Multilayers	$(60/15) \times 4 + 60$	244 ± 4	0.91	26.6
	$(30/15) \times 4 + 30$	183 ± 1	0.93	122.9
	$(30/15) \times 4 + 10$	125 ± 1	0.87	116.3
	$(80/15) \times 4 + 10$	121 ± 2	0.85	41.7

The results show how the emitters' lifetime can be strongly modified by the underlying substrate. In all the samples, the PMMA layer is in contact with an alumina layer, which acts as a spacer from the underlying gold layer. Comparing the results with the two bilayer samples, one observes immediately the influence of the spacer thickness on the lifetime. In all the multilayer samples a short lifetime decay is observed, which gets smaller as the spacer is reduced. The two multilayers with a 10 nm thick alumina spacer, although having different filling fractions, show the same value of the lifetime decay.
A theoretical model (described in Section 1.7) was implemented to reproduce the behavior of the bilayer samples. This model was also used to study the influence on the emitters'

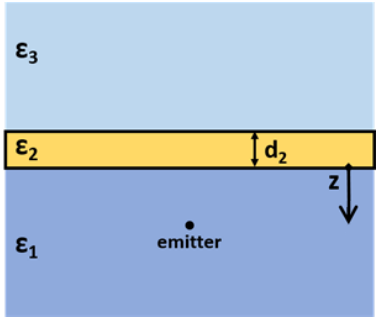

Figure 4.12: Scheme of the CPS model implemented to compute the emission rate of emitters placed in proximity of a gold thin layer. The medium containing the emitters and the medium on the other side of the gold layer are infinitely thick. The emission rate depends on the distance z of the emitters from the thin Au layer, the thickness d_2 of the layer, and the permittivities of the three media.

lifetime of the first layers in the multilayer samples. Emitters were described as dipole emitters at a given distance z from a thin gold layer with thickness d_2, see Fig. 4.12. At a given distance z the emitters are distributed homogenously in the x-y plane, whereas the distribution of the emitters in the first medium along the z-axis can be chosen arbitrarily. To take in account the spacer, which prevents the emitters from being in direct contact with the gold layer, and the finite thickness of the doped PMMA layer, which is assumed to be doped homogeneously, the following distribution of emitters was considered:

$$f(z) = \begin{cases} 1 & \text{if } t_{spacer} < z < (t_{spacer} + t_{PMMA}), \\ 0 & \text{otherwise.} \end{cases} \tag{4.6}$$

The media on either sides of the gold layer are infinitely thick. The first medium has the permittivity of PMMA, whereas the third medium corresponds to alumina. In the first medium, the role of the interfaces PMMA-air and PMMA-alumina was corrected *a posteriori*.

Given the emitters distribution from Eq. 4.6, and calculating the decay rate of dipoles randomly oriented (as described in Chapter 1.7), the time dependence of the PL intensity is calculated as

$$I_{PL}(t) = \int f(z) e^{-\Gamma_{rad} z} dz. \tag{4.7}$$

The temporal decay curve thus obtained can then be fitted to obtain the value of τ_{eff} for a bilayer according to the model.

The geometry of the model is suitable to study in a way close to reality the thick alumina sample and the two bilayer samples. In Table 4.8 the lifetimes calculated with this model are compared with the experimental values. The values are coherent within a discrepance of 10 μs, which may be caused by uncertainties in the thicknesses considered.

Given the accordance with experimental values, the same model was used also to compute the lifetime for additional bilayers which were not realized experimentally. Namely, bilayers corresponding to the first layers in the multilayer samples were investigated, in order to

Table 4.8: Results from CPS model for bilayers which were also realized experimentally.

sample	τ_{CPS} $[\mu s]$	τ_{exp} $[\mu s]$
50/150 gold/alumina	366	375 ± 1
105 nm thick alumina	341	336 ± 1
50/10 gold/alumina	232	227 ± 1

discern if the lifetime modification in the multilayer samples was caused only by these layers or by all layers in the samples. Therefore, a 15 nm thick gold layer was considered, with spacings of 60 nm, 30 nm, and 10 nm. The values calculated for these three bilayers can be compared respectively with the lifetime of the (60/15)×4+60 multilayer, the (30/15)×4+30 multilayer, and the couple of multilayers $(30/15) \times 4 + 10$ and $(80/15) \times 4 + 10$. The values computed for the bilayers are shown in Table 4.9.

Table 4.9: Results from CPS model for additional bilayers, corresponding to the first layers of the multilayer samples.

sample	τ_{CPS} $[\mu s]$
15/60 gold/alumina	299
15/30 gold/alumina	230
15/10 gold/alumina	149

Comparing the computed values for these bilayers with the experimental results on the corresponding multilayers, one finds that the multilayer samples are characterized by a systematically lower lifetime decay. The stronger reduction of the decay lifetime in the multilayers with respect to the bilayers can be interpreted as the signature of a greater photonic density of states, due to the multilayer structure itself.

In all comparisons between a multilayer and a bilayer (corresponding to the last layers in the multilayer), the lifetime for the multilayer sample is approximately equal to 80% of the lifetime for the bilayer, independently of the filling fraction in the multilayer. Therefore, with these geometries, and at this emission wavelength, the filling fraction does not seem to affect how a multilayer changes the emitters' lifetime. This may be attributed to the fact that the transition between elliptical and hyperbolical regime does not happen abruptly at λ_{ENZ}. Instead, it is smoothed out because of the imaginary component of the in-plane permittivity. Therefore, although the $(30/15) \times 4 + 30$ and the $(60/15) \times 4 + 60$ multilayer should correspond to effective media in different regimes at λ_{em}, they are too close to the transition wavelength to observe a clear effect.

To investigate further the role of the filling fraction on the lifetime modification, the same experiment could be repeated with fluorescent molecules emitting far from the $\lambda_E NZ$ of a given multilayer. Equivalently, the filling fraction could be varied to obtain a suitable distribution of high-k states with respect to the emission wavelength. Furthermore, other studies have shown [40] that the decay rate of emitters coupled with the multilayer is dampened when the distance from the multilayer is smaller than the patterning length

of the system. Therefore, to obtain a stronger signature in the lifetime decrease, the thicknesses of the layers could be lowered, thus increasing the upper value of wavevectors which can propagate in medium as an hyperbolic metamaterial.

4.5 Nonlinear optical properties

The $(30/15) \times 4 + 30$ multilayer sample was examined with the z-scan technique to measure its nonlinear optical coefficients at different wavelengths.
The sample was oriented perpendicularly with respect to the impinging beam. Therefore, the electric field was parallel to the layers' surfaces, so that the effective permittivity $\varepsilon_{\parallel}$ of the multilayer was probed with this technique. The use of the OPA allowed to change the wavelength of the laser beam, to study the multilayer's behavior in the range $500\ nm < \lambda < 600\ nm$. Across this range, the intensity at the lens focus was on the order of $I_0 \sim 100\ MW/cm^2$. For each acquisition of transmittance data, values in the linear regime (that is, measurements with the sample away from the focus) were used as reference values to normalize the whole set.
Additionally, the expression for the nonlinear absorption coefficient has been modified as proposed in [41]. Higher-order nonlinear effects are accounted for by means of an intensity dependent nonlinear absorption coefficient $\beta(I)$, therefore preserving the formula $\alpha(I) = \alpha_0 + \beta(I)I$. Terms of opposite signs are admitted a priori to contribute to $\beta(I)$, and for each term the dependency with intensity is described in terms of a saturation effect:

$$\beta(I) = \frac{\beta_+}{1 + \frac{I}{I_{s+}}} + \frac{\beta_-}{1 + \frac{I}{I_{s-}}}. \tag{4.8}$$

In this expression, $\beta_+ > 0$ is related to reverse saturable absorption (RSA) phenomena, and $\beta_- < 0$ describes saturable absorption (SA) effects. The intensity dependence of these terms is described in terms of a hyperbolic function, to reproduce a saturation effect at high laser intensities. Two distinct saturation intensities, I_{s+} and I_{s-}, are considered. Although saturation effects were observed for the RSA component β_+, the SA coefficient β_- was always found to be negligible. Henceforth, β_- was assumed to be equal to 0 in the fitting function. Regarding the nonlinear refractive index n_2, no saturation effects were observed.
Equation 2.11 was used to fit both open aperture (OA) and closed aperture (OA) z-scans, using the corresponding value for the aperture transmittance S ($S = 1$ for OA, $S = 0.323$ for CA). OA scans were first fitted to extract values of β_+ and I_{s+} as best fit parameters. These parameters were then fixed in the analysis of the CA scans to extract the value of n_2.
In Figs. 4.13 and 4.14 the OA and CA transmittance scans at $\lambda = 520\ nm$ acquired from the multilayer sample are shown. In the OA graph, a minimum of the normalized transmittance is observed at the focal point, corresponding to a dominant negative nonlinear coefficient β_-. A similar minimum peak is observed in the CA graph.

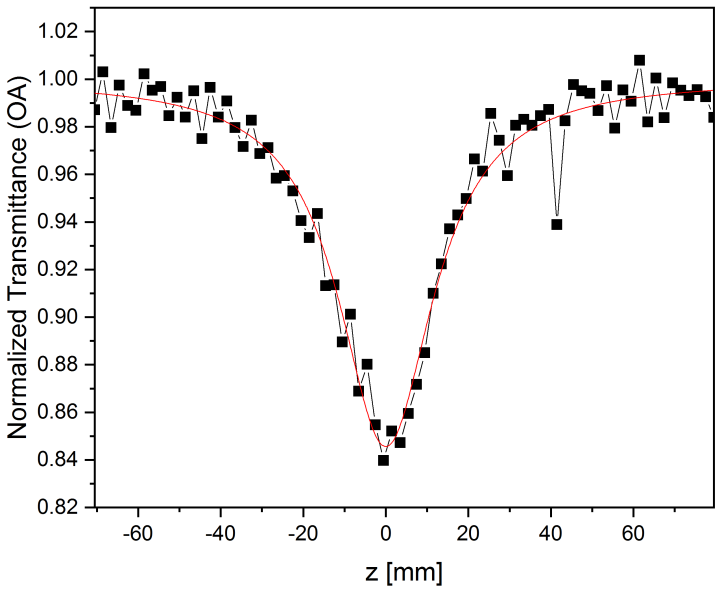

Figure 4.13: OA z-scan of the $(30/15)\times 4+30$ multilayer sample (black squares). The wavelength of the impinging beam was 520 nm, while the peak intensity was $I_0 = 629\ MW/cm^2$. The measurements are normalized to the linear transmittance of the sample. The red curve is the best fit to the experimental data with Eq. 2.11.

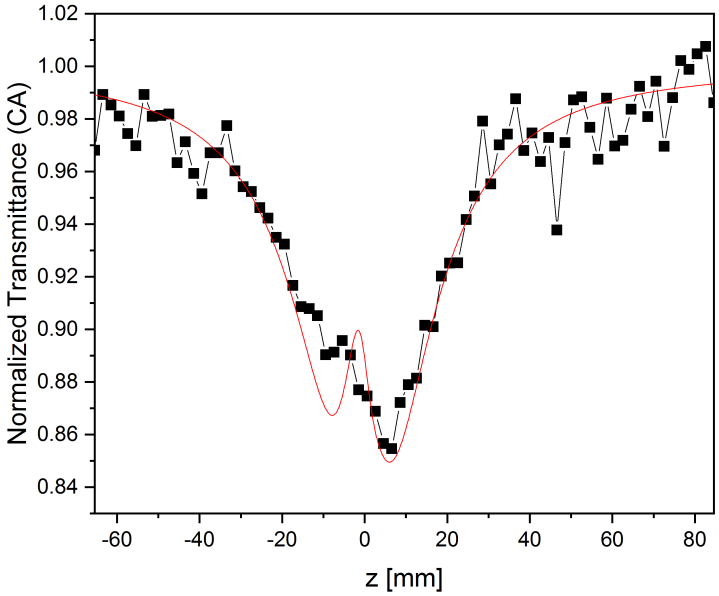

Figure 4.14: CA z-scan of the $(30/15)\times 4+30$ multilayer sample (black squares). The wavelength of the impinging beam was 520 nm, while the peak intensity was $I_0 = 629\ MW/cm^2$. The measurements are normalized to the linear transmittance of the sample. The red curve is the best fit to the experimental data with Eq. 2.11.

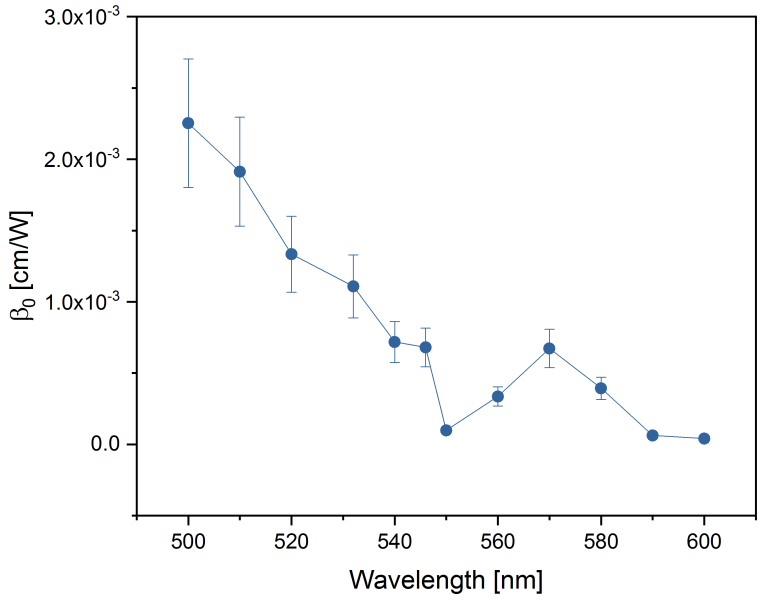

Figure 4.15: Nonlinear absorption coefficient of the $(30/15) \times 4 + 30$ multilayer sample as a function of the wavelength.

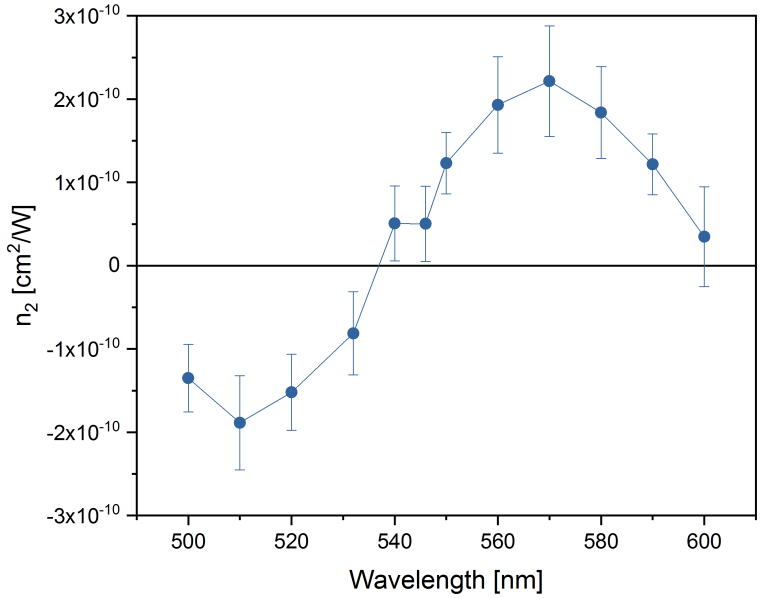

Figure 4.16: Nonlinear refractive index of the $(30/15) \times 4 + 30$ multilayer sample as a function of the wavelength.

The values of β_+ and n_2 of the multilayer measured at different wavelengths are shown in Fig. 4.15 and 4.16. A decreasing trend for the nonlinear absorption coefficient β_+ is observed as the wavelength increases, with values of the order of $\beta_+ \sim 10^{-3}\ cm/W$. Observed values of the saturation intensity I_{s+} are comprised between $I \simeq 10\ MW/cm^2$ and $I \simeq 100\ MW/cm^2$. On the other side, the nonlinear refractive index is found to change from negative values (self-defocusing) to positive values (self-focusing), with the transition happening at $\lambda \sim 540\ nm$. This value may be related to the epsilon-near-zero wavelength of the multilayer, which for a metallic filling fraction of 33% is equal to $\lambda_{ENZ} = 546\ nm$. The z-scan technique was also applied to a bilayer sample, consisting in a 50 nm gold layer with a 150 nm alumina layer on top of it, on silica. The thicknesses of the two layers were chosen to be close to the equivalent thicknesses of gold and alumina in the aforementioned multilayer sample. A high degree of noise in the laser source made it difficult to calculate values for the nonlinear refractive index in particular. Values of the nonlinear absorption coefficient a order of magnitude smaller than in the multilayer sample were observed in the bilayer.

Conclusions

In this work, metal-dielectric multilayers have been studied as an effective approximation for hyperbolic metamaterials (HMM). By means of an effective medium approximation (EMA), a tensorial permittivity can be computed for an infinite stack of repeating layers with negligible thickness with respect to light wavelength. Choosing a proper metal and a dielectric as materials for these layers, principal components of the permittivity with opposite signs are obtained, giving an hyperbolic dispersion relation for TM waves in the medium. This would cause the medium to be able to sustain high-k electromagnetic modes, thus obtaining a diverging photonic density of states. Stacks of alumina and gold layers with thicknesses on the order of tens of nanometers have been selected as a practical implementation of these systems.

Simulations in the frequency domain have been carried out to compare the behavior of hyperbolic metamaterials with layered periodic structures. Computation of reflectance and trasmittance in a prism-coupling configuration showed the presence of high-k propagating modes in both cases for thick samples ($h \sim 1\ \mu m$). Furthermore, these modes are located in regions of the (k, ω) plane whose boundaries correspond to EMA predictions. For thinner samples ($h \sim 100\ nm$) similar results are found, although the dispersion relation is slightly modified by the finite size of the system.

Additionally, a gold nanohole array (NHA) with a two-dimensional hexagonal lattice of nanoholes has been studied as a coupling mechanism in far field. Analysis of wavevector contribution from the hexagonal lattice and simulations in the frequency regimes have shown that this device succeeds in coupling light propagating in far field to the internal high-k modes of the HMM.

Multilayers of gold and alumina have been fabricated and studied experimentally. The synthesis of multilayers made of four couples of gold and alumina layers have been realized by means of magnetron sputtering. The structural properties of the multilayers were examined with several techniques, which indicated independently from one another that the samples consisted of planar layers with sharp interfaces, and whose thicknesses are coherent with chosen values. The linear optical properties of the multilayers were examined by means of spectroscopic ellipsometry, which was used to measure the permittivities of the multilayers modeled as effective media. A best fit analysis confirmed the predictions of EMA formulas for the in-plane permittivity, showing the predicted transition from positive to negative values. A low sensitivity of the fit procedure to the out-of-plane permittivity

was observed instead. Reducing the thickness of the gold and alumina layers would improve the quality of the effective medium approximation, thus increasing the sensitivity to the out-of-plane permittivity.

The photonic density of states in the HMMs was probed through near-field coupling of fluorescent emitters, which in turn modifies their decay lifetime. PMMA layers doped with EuTTA emitters were deposited on top of different dielectrics and also gold-alumina multilayers. A theoretical model, describing the emitters in terms of dipoles, was used to compute the effect of different media and interfaces on the decay lifetime. This model was used to characterize the emitters, to reproduce the results for bilayer samples, and to study the role of the first layers in the multilayer samples. The multilayer samples lowered significantly the decay lifetime, indicating that also the layers far from the doped PMMA layer are able to affect the emitters. In the chosen experimental conditions the multilayers filling fraction didn't seem to affect the degree of lifetime reduction. The analysis of the multilayers' dispersion relation indicates that this could be caused by a smoother transition between dielectric and hyperbolic regime in the multilayers. The emission wavelength and the layers' thicknesses could be optimized to study cases with a proper coupling in distinct regimes.

Nonlinear optical properties of the multilayer were also investigated by means of z-scan technique. A gold-alumina multilayer was investigated with light impinging perpendicularly, probing the in-plane permittivity. Reverse saturable absorption was observed in the sample, giving a positive nonlinear absorption coefficient β_0 on the order of $10^{-3}\ cm/W$. On the other hand, the nonlinear refractive index n_2 was found to change sign at a wavelength close to the wavelength λ_{ENZ} at which the in-plane permittivity $\varepsilon_{\parallel}$ also changes sign. A gold-alumina bilayer with thick layers was studied with the same technique for comparison, finding a nonlinear absorption coefficient an order of magnitude lower and no significant nonlinear refractive effects. Multilayer with different filling fraction could be examined in the same range of intensities to examine if the transition of n_2 moves along with the transition of $\varepsilon_{\parallel}$.

Appendix A

Gaussian beams

A Gaussian beam, that is a monochromatic beam which satisfies the paraxial Helmholtz equation and whose field amplitude and intensity vary in terms of a Gaussian function [42]. The intensity of a Gaussian beam propagating along the z-axis (with $\rho = \sqrt{x^2 + y^2}$) is given by

$$I(\rho, z) = I_0 \left(\frac{w_0}{w(z)} \right)^2 e^{\frac{-2\rho^2}{w^2(z)}}, \tag{A.1}$$

where I_0 and w_0 are the beam intensity and radius (also called waist) at the focus, respectively, and the origin of the z-axis coincides with the beam focus. Away from the focus, the beam radius changes according to

$$w(z) = w_0 \sqrt{1 + \left(\frac{z}{z_R} \right)^2}, \tag{A.2}$$

where z_R is a characteristic length of the Gaussian beam, known as Rayleigh range. Evaluating Eq. (A.1) at a fixed position z' along the axis, one sees that the intensity changes with the term $exp[-2\rho^2/w^2(z')]$, so that it is at its maximum $I_0[w_0/w(z')]$ along the optical axis, and decreases exponentially away from it. Hence, the radius $w(z)$ of a Gaussian beam is the radial distance from the optical axis at which the intensity falls to $1/e^2$ of its value on the axis. The Rayleigh range z_R is the distance from the focus, along the optical axis, at which the radius becomes $w(z_R) = \sqrt{2} w_0$, and it is related to the beam waist by the equation

$$z_R = \frac{\pi w_0^2}{\lambda}. \tag{A.3}$$

Looking at Eq. (A.2), the radius of the Gaussian beam varies slowly for distances from the focus smaller than the Rayleigh range, and $w(z \ll z_R) \simeq w_0$. On the other hand, when $z \gg z_R$, the radius increases linearly with z, namely $w(z) \simeq (w_0/z_R)z$. Hence, away from the focus the beam diverges in a cone-shaped way, where the divergence angle is given by

$$\theta = \frac{w_0}{z_R} = \frac{\lambda}{\pi w_0}. \tag{A.4}$$

It follows that a Gaussian beam focused to a small spot will diverge rapidly away from it. Eq. (A.3) additionally implies that a small waist at the focus restricts the region of slowly varying radius as well.

The Rayleigh range also shows up in the expression for the phase of the electric field of a Gaussian beam as it propagates,

$$\Delta\phi(z) = \left(kz + \frac{k}{2R(z)} - arctan(\frac{z}{z_R}) \right), \tag{A.5}$$

where $R(z) = z[1 + (z_R/z)^2]$ is the radius of curvature of the Gaussian beam. One can see that in the Rayleigh range the phase is approximately equal to the phase of a plane wave, whereas far from the the focus it is approximated by the phase of a spherical wave. Therefore, when a collimated Gaussian beam impinges on a convex lens, it is focused at a distance from the lens approximately equal to its focal length, as for a plane wave. A fundamental difference is that at the focal point the beam spot retains a finite size w_0', as a Gaussian beam is converted into another Gaussian beam with different parameters when passing through a thin transparent lens.

Henceforth, a Gaussian beam is fully determined once its wavelength λ and its Rayleigh parameter z_R are known. As the Rayleigh parameter is related to the beam waist at the focus w_0 by (A.3), one can characterize a laser beam by measuring its w_0. This can be achieved by implementing the "knife edge method", in which one measures the beam power as a knife edge is used to intercept a portion of the beam. The knife edge is mounted onto a translation stage at a given position z' on the propagation direction of the laser beam. In our set-up, the translation stage makes it possible to translate the knife edge in the horizontal x-axis, perpendicular to the propagation direction, with a resolution of $10\mu m$. The knife edge is thus translated along the x-axis, from a position in which the laser beam is not intercepted at all, to the point where it is completely blocked, and for every position of the knife edge the power of the laser beam is measured. For a given position x of the knife edge, one would measure a power given by the beam intensity (A.1) integrated over the beam section which is not intercepted by the knife edge:

$$\begin{aligned} P(x;z') &= \int_{x}^{+\infty}\int_{-\infty}^{+\infty} I(x,y;z')dydx \\ &= I_0 \left(\frac{w_0}{w(z')}\right)^2 \int_{x}^{+\infty}\int_{-\infty}^{+\infty} e^{\frac{-2(x^2+y^2)}{w^2(z')}} dydx \\ &= A\ erfc\left(\frac{\sqrt{2}(x-x_c)}{w(z')}\right) \end{aligned} \tag{A.6}$$

The function $erfc(x)$ is the complementary error function, and a non-null value for x_c is obtained if the beam is not perfectly aligned to the z-axis. The curve fitting of this relationship with experimental data allows to obtain the value of $w(z')$ at the particular position z'. This procedure can then be repeated to measure the beam radius at different positions along the z-axis. Typically one is interested to measure the radius both close to the focus and far from it. A fitting procedure with Eq. (A.2) then allows to determine the value of w_0, and thus z_R.

Bibliography

[1] Wenshan Cai and Vladimir Shalaev. *Optical metamaterials: fundamentals and applications*. Springer Science & Business Media, 2009.

[2] CL Cortes, W Newman, S Molesky, and Z Jacob. Quantum nanophotonics using hyperbolic metamaterials. *Journal of Optics*, 14(6):063001, 2012.

[3] Kandammathe Valiyaveedu Sreekanth, Yunus Alapan, Mohamed ElKabbash, Efe Ilker, Michael Hinczewski, Umut A Gurkan, Antonio De Luca, and Giuseppe Strangi. Extreme sensitivity biosensing platform based on hyperbolic metamaterials. *Nature materials*, 15(6):621, 2016.

[4] Andres D Neira, Nicolas Olivier, Mazhar E Nasir, Wayne Dickson, Gregory A Wurtz, and Anatoly V Zayats. Eliminating material constraints for nonlinearity with plasmonic metamaterials. *Nature communications*, 6:7757, 2015.

[5] Alexander A. Govyadinov and Viktor A. Podolskiy. Metamaterial photonic funnels for subdiffraction light compression and propagation. *Phys. Rev. B*, 73:155108, Apr 2006.

[6] Stefan Alexander Maier. *Plasmonics: fundamentals and applications*. Springer Science & Business Media, 2007.

[7] David R Smith, John B Pendry, and Mike CK Wiltshire. Metamaterials and negative refractive index. *Science*, 305(5685):788–792, 2004.

[8] D. R. Smith, Willie J. Padilla, D. C. Vier, S. C. Nemat-Nasser, and S. Schultz. Composite medium with simultaneously negative permeability and permittivity. *Phys. Rev. Lett.*, 84:4184–4187, May 2000.

[9] VG Veselago. Electrodynamics of substances with simultaneously negative electrical and magnetic permeabilities. *Physics-Uspekhi*, 10(4):504–509, 1968.

[10] Richard A Shelby, David R Smith, and Seldon Schultz. Experimental verification of a negative index of refraction. *science*, 292(5514):77–79, 2001.

[11] John Brian Pendry. Negative refraction makes a perfect lens. *Physical review letters*, 85(18):3966, 2000.

[12] Alexander Poddubny, Ivan Iorsh, Pavel Belov, and Yuri Kivshar. Hyperbolic metamaterials. *Nature Photonics*, 7(12):948–957, 2013.

[13] Leonid V Alekseyev, Viktor A Podolskiy, and Evgenii E Narimanov. Homogeneous hyperbolic systems for terahertz and far-infrared frequencies. *Advances in OptoElectronics*, 2012, 2012.

[14] Alessandro Salandrino and Nader Engheta. Far-field subdiffraction optical microscopy using metamaterial crystals: Theory and simulations. *Physical Review B*, 74(7):075103, 2006.

[15] DAG Bruggeman. The calculation of various physical constants of heterogeneous substances. i. the dielectric constants and conductivities of mixtures composed of isotropic substances. *Annals of Physics*, 416:636–791, 1935.

[16] Amnon Yariv and Pochi Yeh. *Optical waves in crystals*, volume 10. Wiley, New York, 1984.

[17] Justin Elser, Viktor A Podolskiy, Ildar Salakhutdinov, and Ivan Avrutsky. Nonlocal effects in effective-medium response of nanolayered metamaterials. *Applied physics letters*, 90(19):191109, 2007.

[18] T. W. Ebbesen, H. J. Lezec, H. F. Ghaemi, T. Thio, and P. A. Wolff. Extraordinary optical transmission through sub-wavelength hole arrays. *Nature*, 391(6668):667–669, 1998.

[19] HA Bethe. Theory of diffraction by small holes. *Physical Review*, 66(7-8):163, 1944.

[20] C Genet and TW Ebbesen. Light in tiny holes. *Nature*, 445(7123):39–46, 2007.

[21] Enrico Fermi. Quantum theory of radiation. *Reviews of modern physics*, 4(1):87, 1932.

[22] Edward Mills Purcell. Spontaneous emission probabilities at radio frequencies. In *Confined Electrons and Photons*, pages 839–839. Springer, 1995.

[23] MS Yeung and TK Gustafson. Spontaneous emission near an absorbing dielectric surface. *Physical Review A*, 54(6):5227, 1996.

[24] RR Chance, A Prock, and R Silbey. Molecular fluorescence and energy transfer near interfaces. *Adv. Chem. Phys*, 37(1):65, 1978.

[25] Robert W. Boyd. *Nonlinear optics*. Academic Press, 3 edition, 2008.

[26] G. Binnig, C. F. Quate, and Ch. Gerber. Atomic force microscope. *Phys. Rev. Lett.*, 56:930–933, Mar 1986.

[27] David Nečas and Petr Klapetek. Gwyddion: an open-source software for SPM data analysis. *Central European Journal of Physics*, 10:181–188, 2012.

[28] Vaclav Holy, Tilo Baumbach, and Ullrich Pietsch. *High-resolution X-ray scattering from thin films and multilayers*. Springer, 1999.

[29] L Lutterotti, D Chateigner, S Ferrari, and J Ricote. Texture, residual stress and structural analysis of thin films using a combined x-ray analysis. *Thin Solid Films*, 450(1):34–41, 2004.

[30] JA Woollam. *Guide to using WVASE32*, 2002.

[31] Mansoor Sheik-Bahae, Ali A Said, T-H Wei, David J Hagan, and Eric W Van Stryland. Sensitive measurement of optical nonlinearities using a single beam. *IEEE journal of quantum electronics*, 26(4):760–769, 1990.

[32] Sheng-Li Guo, Jun Yan, Li Xu, Bing Gu, Xi-Zhi Fan, Hui-Tian Wang, and NB Ming. Second z-scan in materials with nonlinear refraction and nonlinear absorption. *Journal of Optics A: Pure and Applied Optics*, 4(5):504, 2002.

[33] Harish NS Krishnamoorthy, Zubin Jacob, Evgenii Narimanov, Ilona Kretzschmar, and Vinod M Menon. Topological transitions in metamaterials. *Science*, 336(6078):205–209, 2012.

[34] P. B. Johnson and R. W. Christy. Optical constants of the noble metals. *Phys. Rev. B*, 6:4370–4379, Dec 1972.

[35] IH Malitson and MJ Dodge. Refractive-index and birefringence of synthetic sapphire. In *Journal Of The Optical Society Of America*, volume 62, pages 1405–1405. AMER INST PHYSICS CIRCULATION FULFILLMENT DIV, 500 SUNNYSIDE BLVD, WOODBURY, NY 11797-2999, 1972.

[36] Victor Liu and Shanhui Fan. S^4 : A free electromagnetic solver for layered periodic structures. *Computer Physics Communications*, 183(10):2233 – 2244, 2012.

[37] Günter Schatz. Self-assembled nanospheres: an exciting playground. *Acta Physica Polonica A*, 115(2):431–434, 2009.

[38] Burton L Henke, Eric M Gullikson, and John C Davis. X-ray interactions: photoabsorption, scattering, transmission, and reflection at e= 50-30,000 ev, z= 1-92. *Atomic data and nuclear data tables*, 54(2):181–342, 1993.

[39] T Tumkur, Y Barnakov, ST Kee, MA Noginov, and V Liberman. Permittivity evaluation of multilayered hyperbolic metamaterials: Ellipsometry vs. reflectometry. *Journal of Applied Physics*, 117(10):103104, 2015.

[40] Omar Kidwai, Sergei V Zhukovsky, and JE Sipe. Dipole radiation near hyperbolic metamaterials: applicability of effective-medium approximation. *Optics letters*, 36(13):2530–2532, 2011.

[41] Bing Gu, Ya-Xian Fan, Jing Chen, Hui-Tian Wang, Jun He, and Wei Ji. Z-scan theory of two-photon absorption saturation and experimental evidence. *Journal of Applied Physics*, 102(8):083101, 2007.

[42] Malvin Carl Teich and B Saleh. *Fundamentals of photonics*. Canada, Wiley Interscience, 1991.

List of Figures

List of Tables